Homogeneous reduction by bifunctional manganese catalysis
a quantum chemical approach

Krieger, A.M.

DOI
10.4233/uuid:3377329a-8c7f-4b67-84a0-4a64fe56c0a8

Publication date
2022

Document Version
Final published version

Citation (APA)
Krieger, A. M. (2022). *Homogeneous reduction by bifunctional manganese catalysis: a quantum chemical approach*. [Dissertation (TU Delft), Delft University of Technology]. https://doi.org/10.4233/uuid:3377329a-8c7f-4b67-84a0-4a64fe56c0a8

Homogeneous reduction by bifunctional manganese catalysis: a quantum chemical approach

Homogeneous reduction by bifunctional manganese catalysis: a quantum chemical approach

Dissertation

for the purpose of obtaining the degree of doctor
at Delft University of Technology,
by the authority of the Rector Magnificus
Prof.dr.ir. T.H.J.J. van der Hagen,
chair of the Board for Doctorates,
to be defended publicly on
Tuesday, 22 March 2022 at 12:30 o'clock

by

Annika Meike KRIEGER

Master of Science in Chemistry,
Radboud University Nijmegen, the Netherlands,
born in Düsseldorf, Germany.

This dissertation has been approved by the promoters:

promotor: prof. dr. E.A. Pidko
copromotor: dr. G. Li

Composition of the doctoral committee:

Rector Magnificus,	chairperson
Prof. dr. E.A. Pidko	Delft University of Technology, promotor
Dr. G. Li	Wageningen University and Research, copromotor
Independent members:	
Prof. dr. ir. A. Urakawa	Delft University of Technology
Dr. C. E. Paul	Delft University of Technology
Prof. dr. ir. T. J. H. Vlugt	Delft University of Technology
Prof. dr. M. Tromp	University of Groningen
Dr. I. A. W. Filot	Eindhoven University of Technology

Printed by: Gildeprint Drukkerijen, Enschede

ISBN 978-94-6419-442-5

Contents

Preface

The word catalyst is often associated to a laboratory or a chemical plant, and usually only occurs in the vocabulary of scientists. We have other names for the catalysts around us. We call them lactase, laundry detergent, or exhaust emission control devices and they are part of our daily life. Even the functioning of our body depends on approximately 75.000 naturally-occurring catalysts, called enzymes.

Scientifically speaking, a catalyst is defined as a substance that lowers the energy penalty required by a chemical reaction to proceed without being consumed in the process. Catalytic reactions play a major role in global industries such as chemical synthesis, petroleum refining, polymers and petrochemical industries, and environmental applications.

One of the oldest and most important catalytic transformations might be the brewing of beer: In the fermentation process, enzymes present in yeast break down the sugar molecules of the grains into ethanol. Before the discovery of this process people used to track around in wandering tribes. Civilization only began when fields of grains were planted and the wandering tribes settled down. According to historians[1], the sole purpose of growing these grains was to use them to brew beer. One can therefore propose that the rise of modern static civilization was only a side effect of the brewing of beer. A simple catalytic transformation that made the world into what it is now.

While humanity had about 70 centuries to use trial and error to perfect the beer brewing process, modern catalytic reactions will not enjoy the same amount of time and attention to book the greatest possible improvement. One goal of the scientific community is to develop methods that enable us to skip trial and error approaches and directly predict which catalytic species and reaction conditions give us the desired result.

In this thesis I focus on the application of computational tools to describe and understand catalytic processes better. Analysing the mechanism of a catalytic reaction, the influence of the reaction environment and trends in the stability of catalytic species help us to identify factors that can contribute to rational catalyst design in the future.

---

[1] B. Hayden, N. Canuel, and J. Shanse, *What Was Brewing in the Natufian? An Archaeological Assessment of Brewing Technology in the Epipaleolithic*, J. Archaeol. Method Theory **20**, 102 (2013).

1

Introduction

The application of manganese in homogeneous catalysts has gained vast popularity in the last years.[1–4] Manganese is one of the most abundant transition metals in the Earth's crust and it is also highly biocompatible, facilitating its use in the pharmaceutical industry. Therefore, it is an attractive candidate to replace noble transition metals that are frequently employed in homogeneous catalysts, but which are often toxic and much more expensive than manganese. While heterogeneous catalysis is the overall market leader in today's chemical industry, homogeneous catalysts have critical niche applications as they can offer attractive reaction conditions that are milder and can tune the chemo-, regio- and stereoselectivity.[5] Homogeneous catalysts are consequently often applied in the fine chemical industry that operates at small or medium scale, but requires high tunability and excellent selectivity of the catalytic conversions. In particular pharmaceuticals, agrochemicals, flavours and fragrances are synthesised with homogeneous catalytic transformations as their application results in higher selectivity and faster production.[6] The most applied processes include oxidation, hydroformylation, carbonylation, ogligomerization, hydrocyanation and hydrogenation reactions that are carried out with homogeneous transition metal catalysts.

The efficient hydrogenation of carbonyl compounds has historically relied on stoichiometric reduction methods with alkali metal hydrides and borohydrides.[7, 8] With an increased awareness of the environmental impact of these transformations, catalytic reduction reactions have become an atom-efficient alternative. Especially the application of transfer hydrogenation and hydrogenation with molecular hydrogen are among the most effective transformations available (Figure 1.1). In the last decade the development of manganese-based system has accelerated, offering possibilities to reduce carbonyl compounds under mild conditions and at low catalyst loadings. The employed ligand around the manganese centre is one of the most relevant features that defines activity and selectivity of the catalytic system. This chapter presents a concise introduction into the use of manganese in catalytic systems aimed at the reduction of carbonyl groups (ketones and esters) in

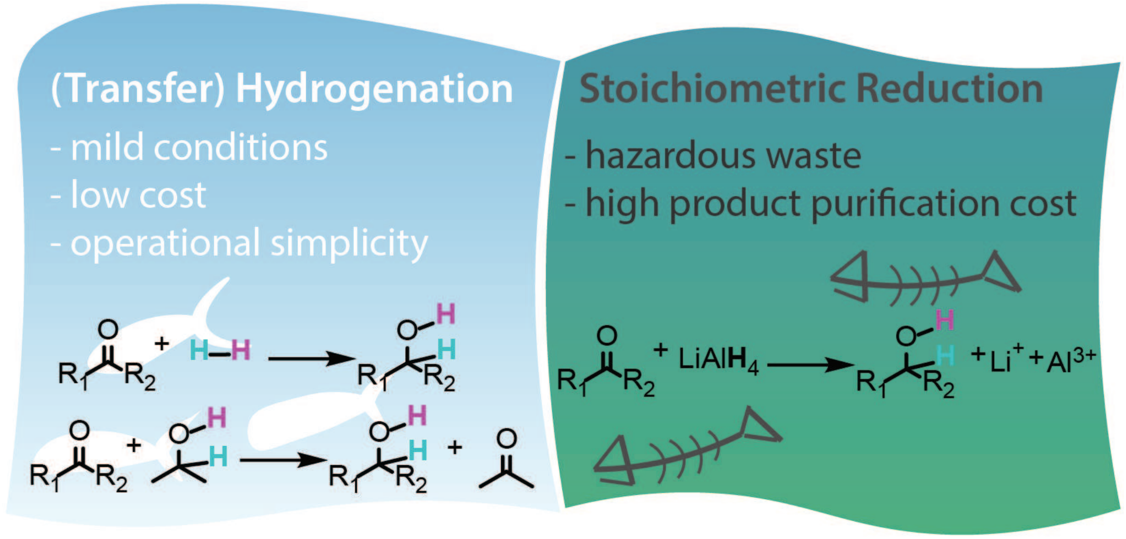

Figure 1.1: Illustration of advantages of catalytic hydrogenation reactions and disadvantages of stoichiometric reductions, with schematic illustration of hydrogenation with molecular hydrogen (left top), transfer hydrogenation (left bottom) and reduction with $LiAlH_4$ (right)

organic substrates through the processes of transfer hydrogenation and hydrogenation with molecular hydrogen. A timeline of the most noteworthy accomplishments in the development of catalytic systems based on manganese pincer and bidentate complexes is given, followed by a section dedicated to mechanistic studies.

1.1. Transfer Hydrogenation and Molecular Hydrogenation

Homogeneous reduction of carbonyl substrates can be achieved by different catalytic transformations. Hydrogenation catalysts focus on the use of gaseous H_2 to reduce the organic substrate. The reaction is highly atom-efficient, however high hydrogen pressure needs to be employed. In transfer hydrogenation reactions a hydrogen donor substrate provides the H_2 equivalent in an activated form to be transferred to the substrate with the use of a catalyst molecule (Figure 1.2).[9] In the course of the reaction, a small molecule such as isopropanol present in excess is oxidized by a catalyst to donate its hydrogen atoms and reduce the substrate. The development of transfer hydrogenation reactions and reductions with molecular hydrogen have booked great achievements with second and third row transition metals. With the award of the Nobel Prize for the development of asymmetric catalysts in 2001[10], the developments of such catalytic systems came in a rapid acceleration. In enantioselective catalysis, the formation of one chiral product is selectively accelerated by the asymmetric catalyst. Therefore, an almost enantiopure product can be formed. So far, great progress has been made towards enabling reduction of a broad range of various functionalized substrates at high enantioselectivities. A special emphasis of the research in enantioselective catalysis is on the improvement of the asymmetric reduction of ketones.[11–17] Many computational studies have focussed on the origin of stereoselectivity.[18–20] However, while multiple studies explain the origin of the formation of chiral product, computations still predominantly support the experimental studies and rationalize the behaviour of the existing catalytic systems. An important persistent goal of the computational catalysis community is to enable rational design to identify the most promising and active catalysts prior to their synthesis to replace the conventional experimental trial and error approaches.[21]

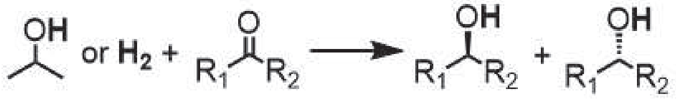

Figure 1.2: (Transfer) hydrogenation of pro-chiral ketones.

1.2. Manganese-based catalysts

The field of catalytic hydrogenation is an old one, with the Wilkinson catalyst being known for decades.[22] Most of the conventional homogeneous transition metal catalysts exhibit metal-centred reactivity, in which the role of the ligand is limited to tuning the steric and electronic properties of the metal centre.[23, 24] Conventional Rh and Ir-based hydrogenation catalysts featuring such a reactivity were particularly active for hydrogenating apolar C=C bonds, while showing only a limited reactivity towards more polar C=O moieties.[25–27] To reduce the latter, polar activation of an H_2 molecule is necessary. The reduction can be achieved by using the so-called metal-ligand cooperation concept, in which the metal centre and the ligand are both directly involved in the catalytic transformation. These bifunctional catalysts allow for a controlled coordination of the substrate molecule and a steered conversion into the desired product. While initially especially second and third row transition metals have been incorporated (with a focus on Ru and Rh), recently transition metals from the first row have gained popularity (mainly Mn, Fe and Co).[28] Manganese has, despite its low toxicity, natural abundance and bioavailability, only been implemented in C=O reduction catalysts since 2016.[1, 3, 4] Next to its abilities in (de)hydrogenation catalysis, its characteristics for the conversion of C-H bonds have been highlighted in multiple reviews.[29–33] Since then, multiple ligand backbones have been explored and adapted from prominent examples that were applied for earlier transition metal catalysts.

1.2.1. Pincer Complexes

The first example of a catalyst for the hydrogenation of C=O bonds has been published by Beller and co-workers.[34] A P,N,P-pincer type Mn(I) catalyst (**A**, Figure 1.3) was introduced with the ability to reduce ketones and aldehydes with molecular hydrogen. A wide range of ketones and aldehydes were reduced with 1mol% Mn(I)-catalyst and a high concentration (3mol%) of strong base (t-BuONa). For the reduction of ketones high conversions, in the upper 90%, were achieved under a hydrogen pressure of 30bar and a temperature of 100°C after 24hrs reaction time. Aldehydes were reduced under milder conditions with only 10bar hydrogen pressure at a temperature of 60°C to achieve conversions between 78% and 99%. In parallel, the group of Kempe investigated Mn(I)-PNP catalysts and reported an example that reduces ketones and aldehydes under milder conditions.[35] With a catalyst loading of only 0.1mol%, substrates were reduced with conversions above 97% at 80°C and 20bar hydrogen pressure in 4 hours. To reduce bulkier substrates, higher catalyst concentrations of up to up to 1mol% were required. Base (KOtBu) is added to the catalytic system to enable the activation of the catalyst.

Later in 2016, Beller and co-workers showed that the previously synthesized Mn(I)-PNP catalyst (**B**, Figure 1.3) can also be used to effectively reduce more challenging ester substrates.[36] Yields above 75% were achieved with catalyst loadings of 2mol% and in the presence of 10mol% base (KOtBu) at 110°C and 30bar H_2. Density functional theory (DFT) was used to support an outer-sphere mechanistic proposal, in which the ester is hydrogenolyzed to form an alcohol and aldehyde intermediate. The rapid hydrogenation of the latter produces a second alcohol product. The first hydrogenation step showed the highest energy barrier. The ligand scope was soon extended beyond the P,N,P-pincer by Milstein and co-workers, who introduced a Mn(I)-PNN catalyst (**D**, Figure 1.3) for the reduction of esters.[37] The group of Beller removed phosphine completely from the catalytic system by presenting the first manganese pincer catalyst with a N,N,N-type backbone (**C**, Figure 1.3) that reduced ketone substrates via transfer hydrogenation.[38] The reaction could be carried out under ambient pressure at catalyst loadings of 1 mol% and base concentrations (KOtBu) of 2 mol%. Reductions at 70°C gave yields up to 99% for halogen containing ketones and up to 98% for aromatic ketones after 24hrs. More catalysts for transfer hydrogenation reductions of ketones have

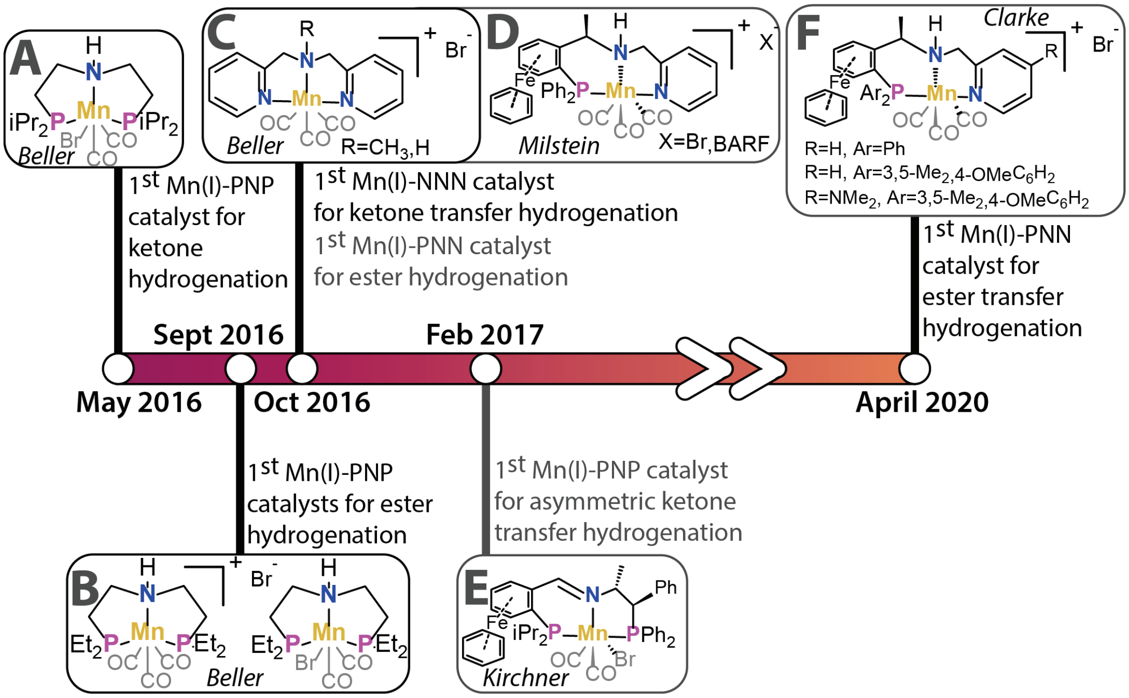

Figure 1.3: Timeline of important findings in Mn-pincer based catalysts in the reduction of esters and ketones.

been developed since, featuring P,N,P- and P,N,N-ligand backbones.[39, 40] These catalysts have enabled the enantioselective reduction of ketones, producing chiral alcohols.

In 2020, the first catalytic system capable of the reduction of esters by transfer hydrogenation has been reported by Clarke and co-workers.[41] Mn(I)-catalysts with P,N,N-ligands (**F**, Figure 1.3) have been applied at concentrations of 1mol% using ethanol as the hydrogenation agent at 100°C. After 22hrs conversions up to 90% were achieved. Interestingly, the highest yields were obtained when using very high concentrations of the base promotor (KOtBu) of 20mol%. Further investigation showed that whereas the concentration of the base critically affect the conversion, this parameter does not significantly influence the overall enantioselectivity.

1.2.2. Bidentate Complexes

Continuing the development of manganese-based catalytic systems pincer backbones were soon replaced by bidentate ligands following the trend set by Ruthenium-based systems. In April 2017 Beller and Pidko presented the first P,N-type catalyst (**G**, Figure 1.4) for the hydrogenation of esters.[42] The reaction proceeded with a catalyst loading of 1mol% and high base concentrations between 10 and 75mol%. Aliphatic and aromatic esters were reduced under a hydrogen pressure of 50bar and at 100°C. In the study the effect of the base was examined showing that the activity is inhibited if lower concentrations are applied.

An effective catalyst for transfer hydrogenation reactions has been introduced by Sortais and co-workers.[43] In June 2017, they reported an aminomethylpyridine(N,N)-ligand (**H**, Figure 1.4) that reduced ketones completely after reactions of 20 minutes at 80°C. Even at room temperature complete conversions were achieved with catalyst concentrations of 0.5mol% and 1mol% base additive.

The first example of asymmetric transfer hydrogenation of ketones was also reported by the group of Sortais.[44] The diamine-ligand (**I**, Figure 1.4) was introduced in July 2017 for the selective reduction of ketones with up to 90% enantioselective excess (e.e.). Reaction conditions were optimized at catalyst loadings of 0.5mol% and 1mol% base. Good conversions were achieved at 80°C after 3hrs, depending on the structural features of the ketone.

In November of the same year Sortais introduced another bidentate catalyst that reduces ketones with molecular hydrogen.[45] The phosphino-pyridinyl(P,N)-ligands achieved high yields (up to 96%) under temperatures of 50°C and a hydrogen pressure of 50bar. Pidko and co-workers continued the improvement of the catalytic systems by introducing a complex with an N-heterocyclic carbene ligand (**J**, Figure 1.4) that works at very low catalytic concentrations, at 0.05mol% loading.[46] These catalyst concentrations approach the ones usually applied in

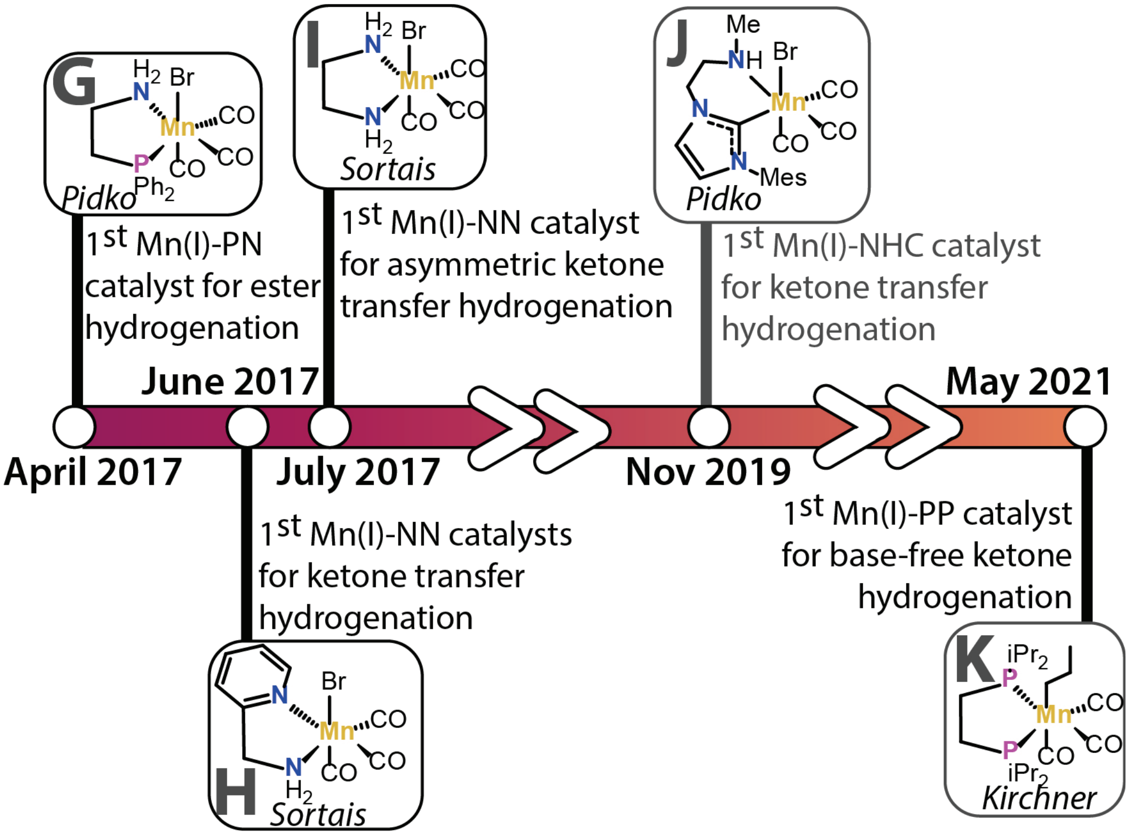

Figure 1.4: Timeline of important findings in Mn-bidentate based catalysts in the reduction of esters and ketones.

ruthenium and iron catalysts. The reaction proceeds to yields up to 94% and is highly active at 80°C. Excellent enantioselectivities at room temperatures were obtained by the Mn(I)-complex with bidentate aminophosphine ligands reported by Bastin and Sortais in July 2020. At catalyst loadings of 0.5mol% and base concentrations of 1mol% enantioselective excesses up to 99% were achieved at temperatures of 30°C after 14hrs. In May 2021, the first bidentate catalyst that reduces ketones under base-free conditions was presented by Kirchner and co-workers (**K**, Figure 1.4).[47] Aromatic and aliphatic ketones were reduced at catalyst concentrations of 3mol% under hydrogen pressure of 10bar.

Manganese-based catalysts applying pincer and bidentate ligands are mainly inspired by previously developed successful catalyst systems. Often ligands that have earlier been used to synthesize ruthenium or iron catalysts have been directly translated to the synthesis and catalytic applications of their manganese-based counterparts. Importantly, early on catalytic studies pointed to the critical role of the reaction conditions, and, in particular, the presence of the alkoxide base in the catalytic system for the efficiency of the Mn-based catalysts. So far, great progress has been achieved in expanding the substrate scope, improving conversion and selectivity. Also the reaction conditions have been tuned, enabling reductions to be carried out at lower temperatures and pressures and with smaller amounts of additives. However, manganese based catalysts still often require higher catalyst concentrations and more complex reaction environments than their more expensive and rare Ir- and Ru-based counterparts.

1.3. Mechanistic Considerations

The development of manganese-catalysed reduction reactions has followed that of its neighbours in the periodic table including ruthenium, iridium and iron.[15, 23, 48, 49] Mechanistic knowledge of bifunctional catalysts has primarily been obtained from these transition metals.[50–55] The most important considerations leading the design of novel catalysts have been the cooperation of the nucleophilic moiety and the Lewis acid/Brønsted site of the complex: the ligand must be capable of proton transfer and hydrogen bonding to enable substrate activation and transformation. Insights that were gained in earlier studies of catalysts with various transition metals could therefore be translated to Mn(I)-complexes.

1.3.1. Hydrogenation Reactions with Molecular Hydrogen

The first experimental report by Beller and co-workers on the use of Mn(I)-pincer catalysts for the hydrogenation of nitriles, ketones and aldehydes, was accompanied with a computational study of the mechanism of Mn(I)-catalysed reductions of a nitrile moiety and exploration of specific reaction steps for benzaldehyde.[34] Following the mechanistic investigation a step-wise mechanism for the amine-complex was proposed. Elangovan et al. provided evidence that an endergonic Mn-H transfer to the C=O bond, forming C-H, was the first step in the reaction. This was followed by a much more favourable exergonic proton transfer from the N-H group of the ligand (Figure 1.6, top). In a later study, Beller extended the DFT studies to methyl benzoate, for which an outer-sphere mechanism was proposed (Figure 1.7, top).[36] In the outer-sphere mechanism the hydride from the Mn-H moiety and the proton of the ligand's NH site of the reactive Mn(I)-amine complexes are transferred simultaneously to the substrate. First the ester is hydrogenated to form a metastable gem-diol intermediate that is rapidly converted to an aldehyde and alcohol. Concomitantly, the catalytic species is dehydrogenated to form a Mn(I)-amido complex, which then reacts with H_2 to regenerate the reactive manganese hydrido amine state capable of further reducing the aldehyde intermediate. In their paper from 2016 Milstein and co-workers reported an NMR study on the PNN-hydrogenation catalyst confirming the existence of the amido- and amine-complexes during the reduction of ester substrates. Interestingly, it was observed that the *syn*-orientation of the amine hydride, where the Mn-H and N-H are orientated in a plane in close proximity isomerizes to an *anti*-orientation during the reaction. The *anti*-orientation replaces the Mn-H with a CO-group, resulting in the proton being directed opposite to the hydride.

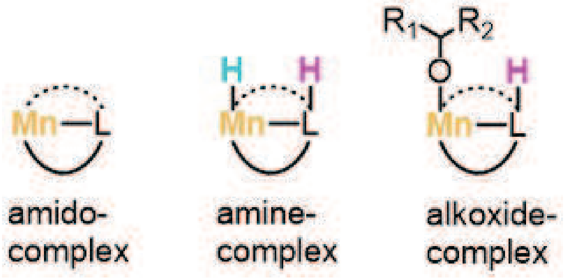

Figure 1.5: Important intermediates in reduction reactions.

Pidko and co-workers also provided computational evidence for an outer-sphere mechanism for the first Mn(I)-bidentate complex capable of efficient reduction of esters.[42] The DFT calculations were conducted on methyl acetate as a model substrate and emphasized the role of the base-assisted hydrogenolysis in the activation of the catalytic species. Furthermore, the importance of metal-ligand cooperation in H_2 activation and substrate coordination has been highlighted. In a later study on the same catalytic system, the effect of the base in the catalytic cycle has been further analysed.[56] It was shown that the base additive assists the catalytic reaction by pre-activating the substrate and facilitating the hydride transfer step. Also, the alkoxide species that can form upon complexation of the manganese centre with the aldehyde has been proposed as a resting state that can lead to catalyst deactivation (Figure 1.7, bottom). The existence of the alkoxide species has earlier been detected in a study by Kirchner and co-workers in 2018.[57] In a stoichiometric study in deuterated solvent, the reaction of 4-fluorobenzaldehyde with the active Mn-amine complex was followed. The formation of the alkoxide species has been detected using NMR- and IR-spectroscopy. The experimental studies were supported by DFT calculations providing a molecular-level description of the formation of the alkoxide species and the regeneration of the Mn-amine species via the inner-sphere reaction mechanism (Figure 1.6, middle).

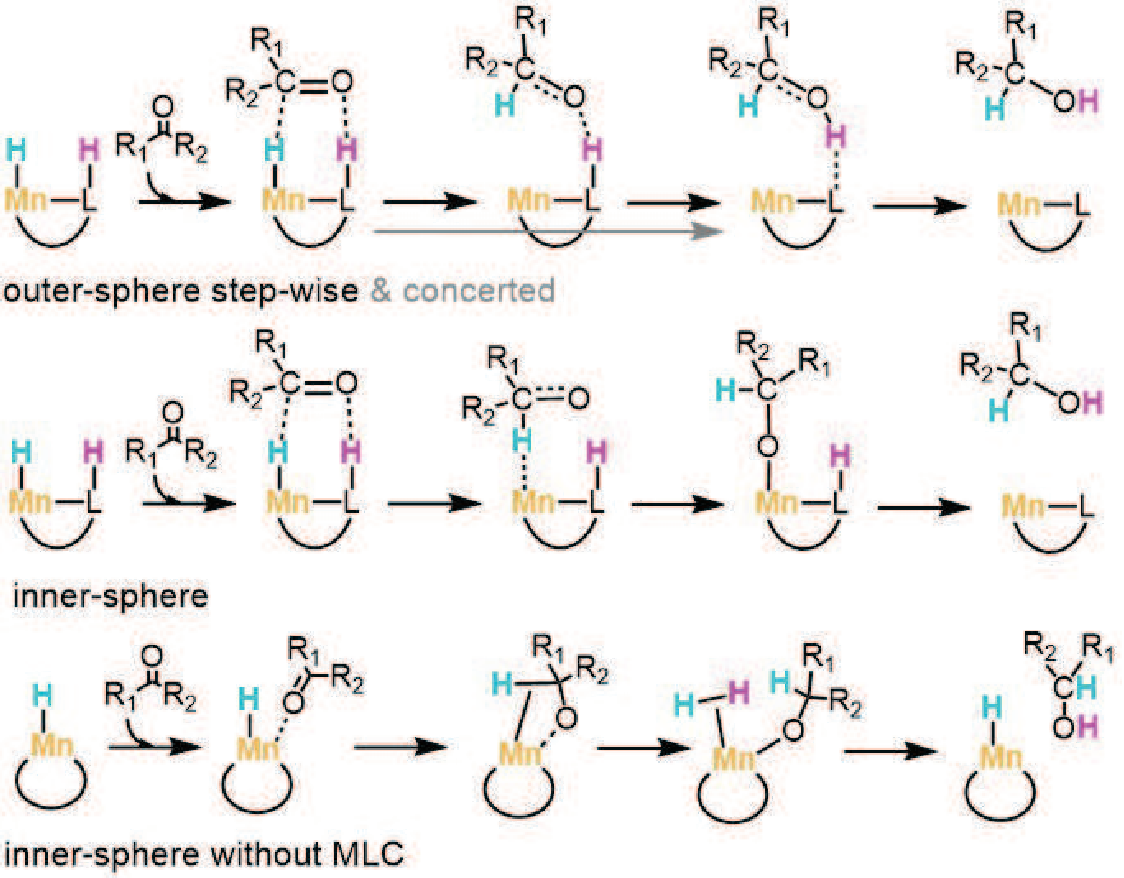

Figure 1.6: Proposed steps in the reduction mechanisms for the hydrogenation of ketones and aldehydes. Top: outer-sphere concerted (grey) and step-wise (black) mechanism, middle: conventional inner-sphere mechanism with alkoxide as intermediate species, bottom: inner-sphere mechanism at metal centre without metal-ligand cooperation (MLC).

In 2021 Kirchner developed a P,P-bidentate catalyst, for which DFT calculations proposed an inner-sphere mechanism for the reduction of acetophenone (Figure 1.6, bottom).[47] In contrast to earlier studies, the calculated catalytic cycle proposes a mechanism without ligand N-H bond participation where the ligand does not play an active role in the catalytic reaction. Coordination and reduction of the substrate solely take place at the metal centre.

1.3.2. Transfer Hydrogenation Reactions

The mechanism of transfer hydrogenation reactions has been mostly investigated for ketone reduction with isopropanol (iPrOH) as a hydrogen source. In transfer hydrogenation reactions by transition metal complexes, two possible modes of hydrogen transfer are commonly considered, namely, the monohydride and dihydride pathways. In a monohydride pathway the hydrogen is transferred to the same group as it originally stems from, while in the dihydride pathway the location of the substitution varies (Figure 1.8).[58] In the original study of the first manganese N,N,N-pincer catalyst for transfer hydrogenation of different aromatic

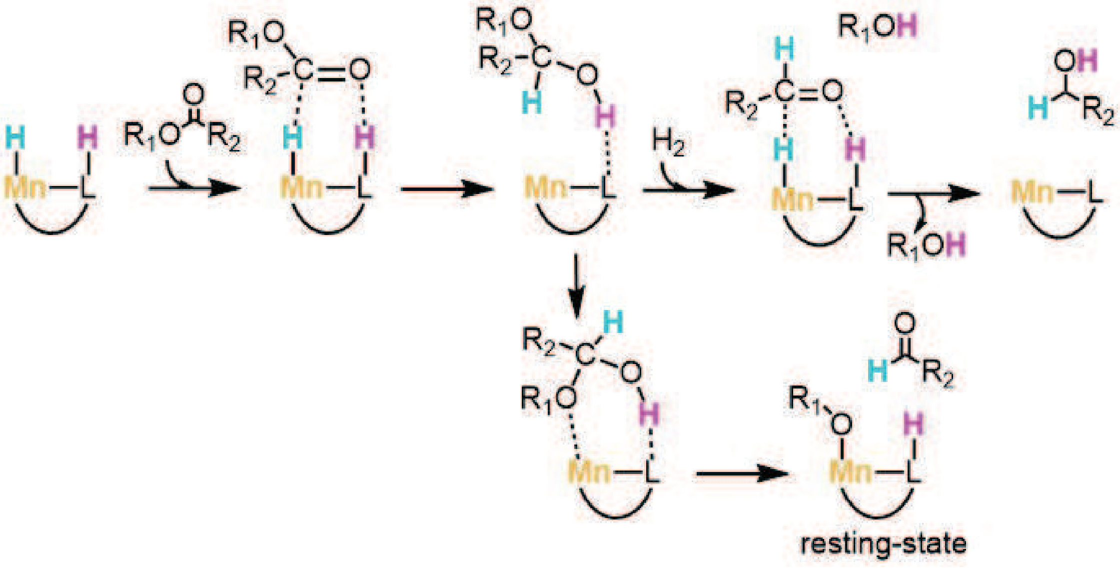

Figure 1.7: Proposed intermediates in the reduction mechanisms for the hydrogenation of esters with the steps of the formation of alkoxide resting-state displayed below.

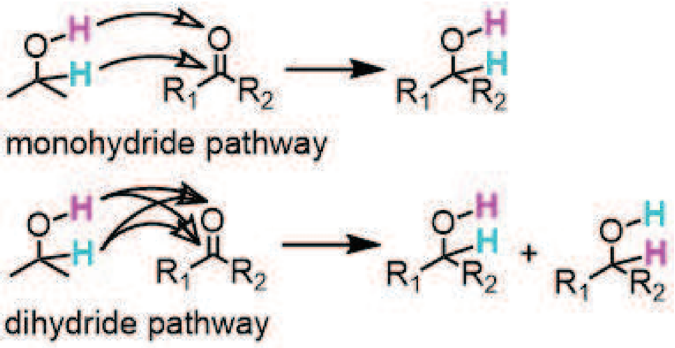

Figure 1.8: Monohydride and dihydride pathway.

ketones with iPrOH, the origin of the H_2 equivalent was examined in deuterated labelling experiments.[38] NMR analysis conclusively pointed to the monohydride mechanism. Interestingly, in this study the importance of the N-H moiety of the ligand, that is often attributed to the activity of the catalyst[59], was also examined. The use of a catalyst with the N-site on the ligand methylated, still provided comparable activities to the pristine Mn-catalyst with the N-H moiety intact. These results suggested that the acid-base cooperative mechanism in ketone reduction may proceed without the involvement of the ligand as the solvent gives sufficiently acidic protons, so there is no need to involve the NH moiety of the ligand.

The group of Kirchner also concluded on the preference for the monohydride pathway in their study in 2017 on ketone reduction by a Mn(I)-PNP complex.[39] DFT studies provided support to an outer-sphere mechanism (Figure 1.6, top) with the C-H group participating in the metal-ligand cooperation (MLC). The calculations also showed that enantioselectivity was steered by steric hindrance. The asymmetry of the catalyst steers the coordination of the substrate, and in turn the hydrogenation of one enantiomer is energetically more favourable. The group of Leitner also assumed an outer-sphere mechanism for their aminotriazole Mn(I)-complex.[60] The MLC was attributed to the N-H moiety in the ligand after carrying out experimental investigations on modified catalysts with the protected amino-moiety. Morris and co-workers also confirmed the outer-sphere mechanism with N-H MLC for their P,N,N-based manganese complex.[40] In their research, attention was drawn to the deactivation pathway and investigated by NMR and DFT studies. In line with earlier studies by Milstein, the metal hydride can deactivate when the *syn*-orientation isomerizes to an *anti*-orientation blocking the MLC functionality. The group of Kundu reported in 2018 their studies on the reactivity of ketone reduction by an N,N-bidentate Mn(I)-catalyst.[61] Mechanistic insights were obtained through DFT calculations, in which the concerted outer-sphere (Figure 1.6, top grey) and inner-sphere mechanisms (Figure 1.6, middle) were directly compared. It was concluded that the outer-sphere mechanism is more likely to take place because of the lower barriers that it provides compared to the inner-sphere mechanism.

Later Khusnutdinova carried out an investigation of the mechanism of ketone reduction by a bipyridine-based Mn(I) catalyst that featured OH-groups on the pyridine moieties.[62] The deuterium labelling experiments provided evidence of a monohydride pathway in the transfer hydrogenation of the ketone substrate. DFT calculations indicated an outer-sphere mechanism with an O-H bond in the ligand being reversible (de)protonated. The experimental and theoretical investigations surrounding the mechanism have unanimously confirmed that ketone reduction by transfer hydrogenation takes place via a monohydride pathway. The concept of metal-ligand cooperation was confirmed in the reduction reactions, providing evidence that the functionality of the ligand can be extended beyond the N-H moiety. Most theoretical investigations succeed in giving an insight into a plausible mechanism. However, the model accuracy is often limited as a majority of the computational studies were carried out with DFT in gas phase.

Knowledge from these studies is developed further and supplemented with solvent description but only a small amount of studies are attributed to understanding the influence of the composition of the solvent environment. Furthermore, kinetic effects that have been observed in experimental settings are mostly explained with calculations focused on the thermodynamics of the system. Theoreticians often only study the catalyst while catalytic activity is attributed to the whole catalytic system.

1.4. Scope of the thesis

The aim of this thesis is to develop a deeper understanding of the important parameters that are provided by the complexity of the catalytic system. Particular emphasis is placed on the effect of the solvent description on a molecular as well as a kinetic level. Furthermore, I try to reduce the gap between experimental studies and DFT calculations by applying multiscale modelling technics including molecular dynamics (MD) simulations and MKM (explained in the next chapter). The first part of the thesis will focus on the computational methodologies that were used in this work. The quantum mechanical modelling methods, DFT and density functional tight-binding (DFTB), are discussed as they lay the basis for all calculations in this thesis. Molecular dynamics (MD) simulations are described, which analyse physical movements of the catalysts. Microkinetic modelling is introduced as a tool to analyse the evolution of our catalytic reaction.

In Chapters 3 and 5 the role of solvent in the catalytic reaction is investigated. Literature has previously described the role of solvent in determining the reaction mechanism. The implementation of continuum or explicit solvent correction can change energy barriers of certain reaction steps, making alternative reaction channels more feasible. Chapter 3 focusses on the kinetic effects of different solvent descriptions, highlighting how the dynamic changing medium composition can affect catalyst performance. In Chapter 5 an alternative reaction mechanism for the reduction of ketones is proposed based on the implementation of explicit solvation.

Chapter 4 introduces a strategy to apply high-throughput computational investigations in assessing descriptors for Mn(I)-pincer catalysis. In the chapter the thermodynamic stability of different adducts is determined by DFT and xTB and used to build scaling relationships.

Chapter 6 focuses on the selectivity control of a catalyst. While computational studies solely based on DFT often rationalize the enantiomeric excess of the reaction by one reaction step, here a microkinetic modelling approach is introduced to determine the origin of selectivity. The chapter shows that contrary to common believe selectivity can depend on various reaction steps using ketone reduction as an example.

References

[1] D. A. Valyaev, G. Lavigne, and N. Lugan, *Manganese organometallic compounds in homogeneous catalysis: Past, present, and prospects,* Coord. Chem. Rev. **308**, 191 (2016).

[2] B. Maji and M. Barman, *Recent Developments of Manganese Complexes for Catalytic Hydrogenation and Dehydrogenation Reactions,* Synthesis (Stuttg). **49**, 3377 (2017).

[3] F. Kallmeier and R. Kempe, *Manganese Complexes for (De)Hydrogenation Catalysis: A Comparison to Cobalt and Iron Catalysts,* Angew. Chemie Int. Ed. **57**, 46 (2018).

[4] M. Garbe, K. Junge, and M. Beller, *Homogeneous Catalysis by Manganese-Based Pincer Complexes,* European J. Org. Chem. **2017**, 4344 (2017).

[5] B. Cornils and W. A. Herrmann, *Concepts in homogeneous catalysis: the industrial view,* J. Catal. **216**, 23 (2003).

[6] A. Behr and P. Neubert, *Applied Homogeneous Catalysis* (Wiley, 2012).

[7] K. Ziegler, *Aluminium-organische Synthese im Bereich olefinischer Kohlenwasserstoffe,* Angew. Chemie **64**, 323 (1952).

[8] J. Kollonitsch, O. Fuchs, and V. Gabor, *New and Known Complex Borohydrides and some of their Applications in Organic Syntheses,* Nature **173**, 125 (1954).

[9] D. Wang and D. Astruc, *The Golden Age of Transfer Hydrogenation,* Chem. Rev. **115**, 6621 (2015).

[10] R. Noyori, *Asymmetric Catalysis: Science and Oppurtunities,* Nobel Lect. , 186 (2001).

[11] R. Noyori, *Asymmetric Catalysis: Science and Opportunities,* Angew. Chemie Int. Ed. **41**, 2008 (2002).

[12] T. Ikariya and A. J. Blacker, *Asymmetric Transfer Hydrogenation of Ketones with Bifunctional Transition Metal-Based Molecular Catalysts,* Acc. Chem. Res. **40**, 1300 (2007).

[13] T. Ikariya, K. Murata, and R. Noyori, *Bifunctional transition metal-based molecular catalysts for asymmetric syntheses,* Org. Biomol. Chem. **4**, 393 (2006).

[14] F. Foubelo, C. Nájera, and M. Yus, *Catalytic asymmetric transfer hydrogenation of ketones: recent advances,* Tetrahedron: Asymmetry **26**, 769 (2015).

[15] R. H. Morris, *Exploiting Metal–Ligand Bifunctional Reactions in the Design of Iron Asymmetric Hydrogenation Catalysts,* Acc. Chem. Res. **48**, 1494 (2015).

[16] R. Noyori and S. Hashiguchi, *Asymmetric Transfer Hydrogenation Catalyzed by Chiral Ruthenium Complexes,* Acc. Chem. Res. **30**, 97 (1997).

[17] C. Wang, X. Wu, and J. Xiao, *Broader, Greener, and More Efficient: Recent Advances in Asymmetric Transfer Hydrogenation,* Chem. - An Asian J. **3**, 1750 (2008).

[18] R. Noyori, M. Yamakawa, and S. Hashiguchi, *Metal−Ligand Bifunctional Catalysis: A Nonclassical Mechanism for Asymmetric Hydrogen Transfer between Alcohols and Carbonyl Compounds,* J. Org. Chem. **66**, 7931 (2001).

[19] A. M. R. Hall, P. Dong, A. Codina, J. P. Lowe, and U. Hintermair, *Kinetics of Asymmetric Transfer Hydrogenation, Catalyst Deactivation, and Inhibition with Noyori Complexes As Revealed by Real-Time High-Resolution FlowNMR Spectroscopy,* ACS Catal. **9**, 2079 (2019).

[20] P. A. Dub and T. Ikariya, *Quantum Chemical Calculations with the Inclusion of Nonspecific and Specific Solvation: Asymmetric Transfer Hydrogenation with Bifunctional Ruthenium Catalysts,* J. Am. Chem. Soc. **135**, 2604 (2013).

[21] E. A. Pidko, *Toward the Balance between the Reductionist and Systems Approaches in Computational Catalysis: Model versus Method Accuracy for the Description of Catalytic Systems,* ACS Catal. **7**, 4230 (2017).

[22] J. A. Osborn, G. Wilkinson, and J. J. Mrowca, *Tris(triphenylphosphine)halorhodium(I),* (2007) pp. 67–71.

[23] J. Pritchard, G. A. Filonenko, R. van Putten, E. J. M. Hensen, and E. A. Pidko, *Heterogeneous and homogeneous catalysis for the hydrogenation of carboxylic acid derivatives: history, advances and future directions,* Chem. Soc. Rev. **44**, 3808 (2015).

[24] R. A. Sánchez-Delgado and M. Rosales, *Kinetic studies as a tool for the elucidation of the mechanisms of metal complex-catalyzed homogeneous hydrogenation reactions,* Coord. Chem. Rev. **196**, 249 (2000).

[25] P. Etayo and A. Vidal-Ferran, *Rhodium-catalysed asymmetric hydrogenation as a valuable synthetic tool for the preparation of chiral drugs,* Chem. Soc. Rev. **42**, 728 (2013).

[26] H.-Y. Jang and M. J. Krische, *Catalytic C−C Bond Formation via Capture of Hydrogenation Intermediates,* Acc. Chem. Res. **37**, 653 (2004).

[27] S. Khumsubdee and K. Burgess, *Comparison of Asymmetric Hydrogenations of Unsaturated Carboxylic Acids and Esters,* ACS Catal. **3**, 237 (2013).

[28] G. A. Filonenko, R. van Putten, E. J. M. Hensen, and E. A. Pidko, *Catalytic (de)hydrogenation promoted by non-precious metals – Co, Fe and Mn: recent advances in an emerging field,* Chem. Soc. Rev. **47**, 1459 (2018).

[29] Y. Hu, B. Zhou, and C. Wang, *Inert C–H Bond Transformations Enabled by Organometallic Manganese Catalysis,* Acc. Chem. Res. **51**, 816 (2018).

[30] W. Liu and J. T. Groves, *Manganese Catalyzed C–H Halogenation,* Acc. Chem. Res. **48**, 1727 (2015).

[31] E. P. Talsi and K. P. Bryliakov, *Chemo- and stereoselective CH oxidations and epoxidations/cis-dihydroxylations with H2O2, catalyzed by non-heme iron and manganese complexes,* Coord. Chem. Rev. **256**, 1418 (2012).

[32] W. Wang, M. M. Lorion, J. Shah, A. R. Kapdi, and L. Ackermann, *Late-Stage Peptide Diversification by Position-Selective C−H Activation,* Angew. Chemie Int. Ed. **57**, 14700 (2018).

[33] F. Collet, C. Lescot, and P. Dauban, *Catalytic C–H amination: the stereoselectivity issue,* Chem. Soc. Rev. **40**, 1926 (2011).

[34] S. Elangovan, C. Topf, S. Fischer, H. Jiao, A. Spannenberg, W. Baumann, R. Ludwig, K. Junge, and M. Beller, *Selective Catalytic Hydrogenations of Nitriles, Ketones, and Aldehydes by Well-Defined Manganese Pincer Complexes,* J. Am. Chem. Soc. **138**, 8809 (2016).

[35] F. Kallmeier, T. Irrgang, T. Dietel, and R. Kempe, *Highly Active and Selective Manganese C=O Bond Hydrogenation Catalysts: The Importance of the Multidentate Ligand, the Ancillary Ligands, and the Oxidation State,* Angew. Chemie Int. Ed. **55**, 11806 (2016).

[36] S. Elangovan, M. Garbe, H. Jiao, A. Spannenberg, K. Junge, and M. Beller, *Hydrogenation of Esters to Alcohols Catalyzed by Defined Manganese Pincer Complexes,* Angew. Chemie Int. Ed. **55**, 15364 (2016).

[37] N. A. Espinosa-Jalapa, A. Nerush, L. J. W. Shimon, G. Leitus, L. Avram, Y. Ben-David, and D. Milstein, *Manganese-Catalyzed Hydrogenation of Esters to Alcohols,* Chem. - A Eur. J. **23**, 5934 (2017).

[38] M. Perez, S. Elangovan, A. Spannenberg, K. Junge, and M. Beller, *Molecularly Defined Manganese Pincer Complexes for Selective Transfer Hydrogenation of Ketones,* ChemSusChem **10**, 83 (2017).

[39] A. Zirakzadeh, S. R. M. M. de Aguiar, B. Stöger, M. Widhalm, and K. Kirchner, *Enantioselective Transfer Hydrogenation of Ketones Catalyzed by a Manganese Complex Containing an Unsymmetrical Chiral PNP′ Tridentate Ligand,* ChemCatChem **9**, 1744 (2017).

[40] K. Z. Demmans, M. E. Olson, and R. H. Morris, *Asymmetric Transfer Hydrogenation of Ketones with Well-Defined Manganese(I) PNN and PNNP Complexes,* Organometallics **37**, 4608 (2018).

[41] M. B. Widegren and M. L. Clarke, *Towards practical earth abundant reduction catalysis: design of improved catalysts for manganese catalysed hydrogenation,* Catal. Sci. Technol. **9**, 6047 (2019).

[42] R. van Putten, E. A. Uslamin, M. Garbe, C. Liu, A. Gonzalez-de Castro, M. Lutz, K. Junge, E. J. M. Hensen, M. Beller, L. Lefort, and E. A. Pidko, *Non-Pincer-Type Manganese Complexes as Efficient Catalysts for the Hydrogenation of Esters,* Angew. Chemie Int. Ed. **56**, 7531 (2017).

[43] A. Bruneau-Voisine, D. Wang, V. Dorcet, T. Roisnel, C. Darcel, and J.-B. Sortais, *Transfer Hydrogenation of Carbonyl Derivatives Catalyzed by an Inexpensive Phosphine-Free Manganese Precatalyst,* Org. Lett. **19**, 3656 (2017).

[44] D. Wang, A. Bruneau-Voisine, and J.-B. Sortais, *Practical (asymmetric) transfer hydrogenation of ketones catalyzed by manganese with (chiral) diamines ligands,* Catal. Commun. **105**, 31 (2018).

[45] D. Wei, A. Bruneau-Voisine, T. Chauvin, V. Dorcet, T. Roisnel, D. A. Valyaev, N. Lugan, and J.-B. Sortais, *Hydrogenation of Carbonyl Derivatives Catalysed by Manganese Complexes Bearing Bidentate Pyridinyl-Phosphine Ligands,* Adv. Synth. Catal. **360**, 676 (2018).

[46] R. Putten, J. Benschop, V. J. Munck, M. Weber, C. Müller, G. A. Filonenko, and E. A. Pidko, *Efficient and Practical Transfer Hydrogenation of Ketones Catalyzed by a Simple Bidentate Mn−NHC Complex,* ChemCatChem **11**, 5232 (2019).

[47] S. Weber, J. Brünig, L. F. Veiros, and K. Kirchner, *Manganese-Catalyzed Hydrogenation of Ketones under Mild and Base-free Conditions,* Organometallics **40**, 1388 (2021).

[48] F. Agbossou-Niedercorn and C. Michon, *Bifunctional homogeneous catalysts based on first row transition metals in asymmetric hydrogenation,* Coord. Chem. Rev. **425**, 213523 (2020).

[49] S.-F. Zhu and Q.-L. Zhou, *Iridium-Catalyzed Asymmetric Hydrogenation of Unsaturated Carboxylic Acids,* Acc. Chem. Res. **50**, 988 (2017).

[50] D. B. Grotjahn, *Heteroatoms moving protons: Synthetic and mechanistic studies of bifunctional organometallic catalysis,* Pure Appl. Chem. **82**, 635 (2010).

[51] C. T. Mbofana and S. J. Miller, *Bifunctional Catalysis with Lewis Base and X-H Sites That Facilitate Proton Transfer or Hydrogen Bonding (n-π*),* in *Lewis Base Catal. Org. Synth.* (Wiley-VCH Verlag GmbH & Co. KGaA, Weinheim, Germany, 2016) pp. 1259–1288.

[52] Y. Liu, X. Yue, C. Luo, L. Zhang, and M. Lei, *Mechanisms of Ketone/Imine Hydrogenation Catalyzed by Transition-Metal Complexes,* Energy Environ. Mater. **2**, 292 (2019).

[53] P. A. Dub and J. C. Gordon, *The role of the metal-bound N–H functionality in Noyori-type molecular catalysts,* Nat. Rev. Chem. **2**, 396 (2018).

[54] M. Yamakawa, H. Ito, and R. Noyori, *The Metal−Ligand Bifunctional Catalysis: A Theoretical Study on the Ruthenium(II)-Catalyzed Hydrogen Transfer between Alcohols and Carbonyl Compounds,* J. Am. Chem. Soc. **122**, 1466 (2000).

[55] X. Zhang, L. W. Chung, and Y.-D. Wu, *New Mechanistic Insights on the Selectivity of Transition-Metal-Catalyzed Organic Reactions: The Role of Computational Chemistry,* Acc. Chem. Res. **49**, 1302 (2016).

[56] C. Liu, R. van Putten, P. O. Kulyaev, G. A. Filonenko, and E. A. Pidko, *Computational insights into the catalytic role of the base promoters in ester hydrogenation with homogeneous non-pincer-based Mn-P,N catalyst,* J. Catal. **363**, 136 (2018).

[57] M. Glatz, B. Stöger, D. Himmelbauer, L. F. Veiros, and K. Kirchner, *Chemoselective Hydrogenation of Aldehydes under Mild, Base-Free Conditions: Manganese Outperforms Rhenium,* ACS Catal. **8**, 4009 (2018).

[58] J.-E. Bäckvall, *Transition metal hydrides as active intermediates in hydrogen transfer reactions,* J. Organomet. Chem. **652**, 105 (2002).

[59] P. A. Dub, B. L. Scott, and J. C. Gordon, *Why Does Alkylation of the N–H Functionality within M/NH Bifunctional Noyori-Type Catalysts Lead to Turnover?* J. Am. Chem. Soc. **139**, 1245 (2017).

[60] O. Martínez-Ferraté, C. Werlé, G. Franciò, and W. Leitner, *Aminotriazole Mn(I) Complexes as Effective Catalysts for Transfer Hydrogenation of Ketones,* ChemCatChem **10**, 4514 (2018).

[61] K. Ganguli, S. Shee, D. Panja, and S. Kundu, *Cooperative Mn(I)-complex catalyzed transfer hydrogenation of ketones and imines,* Dalt. Trans. **48**, 7358 (2019).

[62] A. Dubey, S. M. W. Rahaman, R. R. Fayzullin, and J. R. Khusnutdinova, *Transfer Hydrogenation of Carbonyl Groups, Imines and N-Heterocycles Catalyzed by Simple, Bipyridine-Based Mn I Complexes,* ChemCatChem **11**, 3844 (2019).

2

Computational Methods

In this chapter, a brief overview of the computational approaches that have been used throughout this thesis are explained. Section 2.1 serves as an introduction to the methods used in energy calculations. Sections 2.2 to 2.4 describe methods that build upon the geometric structures and energetics retrieved from the energy calculations.

2.1. Quantum chemical calculations

Quantum chemistry provides a theoretical framework to compute the energetics and all relevant properties of molecular systems. It is the basis for quantum chemical calculations that are widely used to model various properties and reactive events in molecular systems. The basis of these calculations lie in the Schrödinger equation.[1] It outlines how a quantum state evolves by describing the system in terms of wave functions. The Schrödinger equation is the quantum physical equivalent to Newton's second law of motion, which describes the acceleration of a system by considering its mass and force acting on it. Understanding the physical properties of a molecule requires an investigation of the electron distribution and interactions. These properties are defined by the electronic wavefunction defined as:

$$\hat{H}\Psi = E\Psi$$

where the wave function is denoted by Ψ and E being the eigenvalue of the system. $\hat{H}$ is the Hamiltonian operator and describes the total energy of the system. It is split into kinetic energy terms and the potential energy terms.

$$\hat{H} = \hat{T}_N + \hat{T}_e + \hat{V}_{Ne} + \hat{V}_{ee} + \hat{V}_{NN}$$

In the system that is described, both electrons (e) and nuclei (N) are present. Potential energy terms arise from interactions between nuclei and electrons. Since the nuclei have a much larger mass than the electrons, they move at a slower velocity. Therefore, the nuclei can be regarded as frozen and the Schrodinger equation is solved for the electrons only. This is called the Born-Oppenheimer approximation.[2]

$$\hat{H}_{elec} = \sum_i -\frac{1}{2}\Delta_i - \sum_i \sum_A \frac{Z_A}{r_{iA}}\Delta_i + \frac{1}{2}\sum_i \sum_{i \neq j} \frac{1}{r_{ij}}$$

The electronic Hamiltonian ($\hat{H}_{elec}$) compromises two monoelectronic terms and the last term that describes the electron-electron repulsion. In the above equation the kinetic energy is denoted by Δ_i, the protons in the nucleus by Z_A, and the distances between the electrons and electron and nuclei by r_{iA} and r_{ij}.

The electronic Schrödinger equation can be approximately solved using different methods. One of them is Hartree-Fock (HF) theory, where the central field approximation is applied.[3] In the HF approximations a one electron equation is described and therefore electron-electron correlation is neglected. Instead of defining the potential of an electron by its distance to other electrons, it is placed in an average electron field. The correlated motion is not accounted for. If one wants to include possible excitations of the system the wavefunction needs to be expanded, which leads to substantial time-consuming calculations.

In modern computational chemistry, quantum chemical strategies based on the Hohenberg-Kohn (HK) theorem have become the methods of choice as being more efficient and accurate at the same time. It states that every observable in a stationary quantum mechanical system can be calculated from the ground-state density. The electron density of the system, that can be described by 3N variables, the x-, y- and z-position, is the only parameter that is needed, in principle, to compute all its properties. Therefore, a functional of the electron density can describe the total ground state energy of the electron system. This approximation is used in density functional theory DFT calculations.

There are two basic approximations in practical DFT approaches, namely, the local density approximation (LDA) and the generalized gradient approximation (GGA).[4] In the LDA, the exchange-correlation energy for a slowly varying region of a material is assumed to be equal to the density of a homogenous electron gas. This is a very rough approximation to the actual electron density resulting in large deviations of the computed parameters from the experiment. In GGA, gradients of the local electron density are also taken into account by adding a non-uniform attribute to the description of the energy.

While GGA is widely employed for periodic calculations[5], hybrid methods are generally favoured for transition metal-ligand complexes[6–8]. The behaviour of transition metal complexes is often difficult to describe with GGA and LDA methods. Due to varied occupations of valence orbitals, subtle differences in exchange and correlation effects can occur. Hybrid methods can correct for these changes because they are built from different energetic components. In hybrid methods a linear combination of the HF exact exchange functional (E_X) is taken and combined with explicit exchange (E_X) and correlation (E_C) functionals. The weighing of the individual parts of the hybrid exchange-correlation (E_{XC}) functional are usually set by fitting predictions to experimental or calculated thermochemical data. Throughout this thesis the PBE0 functional[9] was used which combines the HF exchange energy with the Perdew–Burke-Ernzerhof (PBE) exchange energy. PBE is a GGA functional which performs especially well for metal systems. The linear combination of the HF and PBE part is specified below:

$$E_{XC}^{PBE0} = \frac{1}{4}E_X^{HF} + \frac{3}{4}E_X^{PBE} + \frac{1}{4}E_C^{PBE}$$

Since the transition metal complexes investigated in this thesis are moderate in size, long range non-covalent interactions need to be described. In conventional DFT approximations these London dispersion interactions, that are induced dipole – induced dipole interactions resulting from the correlated motions of electrons in the interacting fragments, cannot be described well. Such long range interactions can play critical role in defining selectivity and binding patterns in various chemical systems and therefore they need to be explicitly accounted for in quantum chemical calculations.[10] This is usually achieved by adding a dispersion correction term that is either an empirical or experimental parameterized term. Throughout this thesis the DFT-D3 dispersion correction scheme introduced by Grimme was used, which is available for the first 94 elements of the periodic table.[10]

The hybrid DFT calculations are used to locate intermediates and transition state necessary to analyse the potential energy surfaces underlying the chemical transformations investigated in Chapters 3, 5 and 6. While hybrid DFT represents the most widely used and accurate state-of-the-art electronic structure methodologies for computing energetics and geometries of transition metal complexes, they are quite demanding with regards to the computational time and cannot be routinely employed for the analysis of extended volumes of the chemical space for, e.g., computational screening of large libraries of hypothetical TM complexes.

This can be achieved by using the recently developed Density Functional Tight Binding (DFTB) method, which combine a reasonable accuracy with an increased computational efficiency.[11] The acceleration of the electronic structure calculations in DFTB is achieved via the parameterization. The Hamiltonian, $\hat{H}$, is replaced with a parameterized matrix that is calculated from the DT-derived local orbitals and the corresponding potentials. The elements of this matrix depend on the intermolecular distances and orbital symmetries. Due to this simplification calculations can be carried out faster, however the resulting energies and structures become less accurate. Most importantly, the limited scope of the parametrization involved in the development of these methods results in the fact that one cannot a priori predict, when these methodologies will succeed and when they fail. In this thesis, we investigated whether DFT-B can be useful for establishing functionality-structure relationship in a high-throughput computational workflow employing Mn pincer complexes. Specifically, the extended semiempirical tight-binding model GFN2-xTB [12] is applied in Chapter 4 to test its applicability to the manganese metal complexes.

2.2. Solvent models

Homogenous catalysts operate in solvent. To account for the effect of this environment different strategies can be applied. Explicit solvent molecules can be placed in proximity to the catalyst to mimic the direct interaction of the system.[13, 14] This approach gives a physically realistic picture as the solvent can form chemical bonds with the solute molecule. The disadvantage of incorporating explicit solvent molecules is the high computational cost that arises when integrating multiple layers of solvent in quantum chemical calculations. Continuum solvent models, on the other hand, offer a convenient method to incorporate solvent effects without having to place explicit solvent molecules.[15–17] The goal of these solvent models is to approximate the energy that it takes to move the solute molecule from the gas phase to the solvent environment. The Hamiltonian of the system can be split into two terms describing the solute molecule and the interaction ($\hat{V}$) between the solute and the solvent:

$$\hat{H}^{total}(r) = \hat{H}^{solute}(r) + \hat{V}^{solute+solvent}(r)$$

This is achieved by accounting for the electrostatic effects of the solvent environment. The solvent is described as a continuous isotropic field. Empirical parameters are applied in the description, with the dielectric constant of the solvent being the primary one. It defines how polarizable the medium is. A solvent cavity of a certain size and shape is outlined and the solute molecule is placed in there. The charge distribution of the solute polarizes the dielectric medium. From the change of polarization the interaction of the solute and the solvent is calculated.

The continuum solvent system used throughout this thesis is the Solvation Model Based on Density (SMD).[18] It is a universal continuum solvation model that is applicable to charged and uncharged complexes in different solvents. The model estimates the free energy of solvation within the approximation of an ideal solution.

A drawback of the use of continuum solvent models is that only one type of solvent is considered while the catalytic system often consists of a mixture of different solvents and additives. Therefore, an ideal solution is assumed, where upon mixing no change in enthalpy and volume will occur, while often the reality is that of a non-ideal solution. The conductor-like screening model for realistic solutions (COSMO-RS) gives a more suitable description.[19, 20] It is based on the conductor-like screening model (COSMO), which is a model that determines the electrostatic interactions of molecules with the solvent.[21] It differs from the continuum models by deriving polarization charges from a conductor approximation. The cavity surface is split into different segments for the approximation. These polarization charges are combined with a statistical thermodynamic treatment of the interacting surfaces for COSMO-RS. Therefore, instead of a dielectric field the solute and solvent are treated intrinsically. From this chemical potentials are derived, which can be applied to calculate consistent mixture thermodynamics at various temperatures. The choice of the solvent model often depends on the available resources. Continuum solvent models are the most efficient while the inclusion of explicit solvent molecules requires more resources. Therefore, the choice of a certain description does not only depend on the research question to be answered but the available resources. In Chapter 3 we investigate how microscopic- and macroscopic characterizes of the catalytic changes from using different solvent models, specifically comparing SMD with COSMO-RS solvation.

2.3. Molecular dynamics

Another option to account for the interactions that arise from explicit solvation are molecular dynamics (MD) simulations.[22–24] In such MD simulations the catalyst is placed in a box of solvent molecules and the movement of this ensemble is generated based on Newton's equation of motion:

$$F = m * a = m * \frac{\partial v}{\partial t}$$

F denotes the force, m corresponds to the mass and a signifies the acceleration. The MD trajectory is calculated with force fields, which analytical solve the function of the positions of the particles. This can be achieved by integrating the equations or motion by a Verlet algrorithm:

$$r(t + \Delta t) \cong 2r(t) - r(t - \Delta t) + a\Delta t^2 = 2r(t) - r(t - \Delta t) + \frac{F(t)}{m\Delta t^2}$$

The time step in the MD simulation is denoted by Δt. To investigate the reactive events, the electronic structure of the complete chemical system has to be considered in the framework of quantum mechanics. Quantum chemical DFT calculations are used to compute the forces acting on the nuclei at each simulation step, which are then used to propagate the dynamic evolution of the system following the classical Newton's equation of motion. Such an integration of the two theories is enabled by the Born-Oppenheimer approximation and the resulting MD simulation are commonly referred to as the ab initio molecular dynamics (aiMD).[25–27] Ab initio MD was applied in chapter 6 in this thesis to derive the energy barrier of a transition process for a fully solvated system.

While this type of MD simulations are generally applied to retrieve thermodynamic data, variations can be introduced that enable conformational analysis. Low mode MD is a conformational search method that is based on following the low-frequencies of the system.[28] In each step of the MD trajectory the catalytic system is perturbed along a low-frequency vibration mode. These modes often corresponds to rotatable bond confirmations that are sterically hindered. Therefore, the conformations are not attainable in DFT or ab initio MD simulations. When the low mode MD simulation is applied the system can move from one low-energy state to the next. In catalysis, MD simulations can be applied for versatile objectives from generating new catalytic conformations to obtaining energy barriers.

2.4. Microkinetic modeling

The tools described in the previous sections enable us to retain structural and energetic data on specific catalytic intermediates. The complex network of structures and energies gives information on the stability of different intermediates and describes the barrier to achieve a transformation of geometry. However, a large amount of laboratory-based investigations feature kinetic studies. To link the data from the potential energy surfaces to these kinetic experiments microkinetic modelling can be applied.[29–31] The elementary steps of the reaction are coupled with concentration effects to calculate reaction rates. The evolution of this reaction can then be simulated by solving the differential equations. Assuming have the following reaction step:

$$n_a A + n_b B \leftrightarrows n_c C + n_d D$$

Here, n_x denote the stoichiometric coefficient of element X. The reaction rate of this step can be obtained by determining the change in concentration in a set time frame:

$$rate = \frac{1}{n_c}\frac{\partial[C]}{\partial t} = \frac{1}{n_d}\frac{\partial[D]}{\partial t} = \frac{-1}{n_a}\frac{\partial[A]}{\partial t} = \frac{-1}{n_b}\frac{\partial[B]}{\partial t} =$$

$$= k_{fw}[A]^{n_a}[B]^{n_b} = -k_{bw}[C]^{n_c}[D]^{n_d}$$

The reaction rate constant is given by k_{fw} for the forward reaction and k_{bw} for the backward reaction. The rate constant is directly related to the change in Gibbs free energy (ΔG) of a reaction step, which can be written as:

$$K_{eq} = \frac{k_{fw}}{k_{bw}} = \exp\frac{-\Delta G^{\ddagger}}{RT}$$

From transition state theory the reaction rate constant can then be defined by the Eyring-Polanyi equation:

$$k = \frac{\kappa k_B T}{h}\exp\frac{-\Delta G^{\ddagger}}{RT}$$

The Boltzman constant is given by k_B, h is the Planck's constant, κ is the transmission factor, which is usually set to unity, and $\Delta G^{\ddagger}$ is the activation energy that is required to go form an intermediate state to the transition state. By applying these equations and combining them in a model for a whole reaction network enables us to analyse the kinetic parameters of a system. Except the reaction rate, it is possible to evaluate which steps in the network are rate-determining and how the selectivity of the process can be affected.

Microkinetic modelling has been applied in this thesis to study the effect of different solvent models on the degree of rate control, rate-determining steps and resting states in Chapter 3. In Chapter 5, MKM was applied as a tool to highlight the uncertainty in enantiomeric excess predictions.

References

[1] F. Giustino, *Materials Modelling Using Density Functional Theory: Properties and Predictions*, Materials Modelling Using Density Functional Theory: Properties and Predictions (Oxford University Press, 2014).

[2] E. S. Kryachko and E. V. Ludeña, *Energy Density Functional Theory of Many-Electron Systems*, Understanding Chemical Reactivity (Springer Netherlands, 2012).

[3] H. Schaefer, *Applications of Electronic Structure Theory*, Modern Theoretical Chemistry (Springer US, 2012).

[4] W. Kohn, A. D. Becke, and R. G. Parr, *Density Functional Theory of Electronic Structure,* J. Phys. Chem. **100**, 12974 (1996).

[5] J. Hafner, *Ab-initio simulations of materials using VASP: Density-functional theory and beyond,* J. Comput. Chem. **29**, 2044 (2008).

[6] N. E. Schultz, Y. Zhao, and D. G. Truhlar, *Density Functionals for Inorganometallic and Organometallic Chemistry,* J. Phys. Chem. A **109**, 11127 (2005).

[7] F. Furche and J. P. Perdew, *The performance of semilocal and hybrid density functionals in 3d transition-metal chemistry,* J. Chem. Phys. **124**, 044103 (2006).

[8] A. Bencini, *Some considerations on the proper use of computational tools in transition metal chemistry,* Inorganica Chim. Acta **361**, 3820 (2008).

[9] C. Adamo and V. Barone, *Toward reliable density functional methods without adjustable parameters: The PBE0 model,* J. Chem. Phys. **110**, 6158 (1999).

[10] L. Goerigk, *A Comprehensive Overview of the DFT-D3 London-Dispersion Correction,* in *Non-Covalent Interact. Quantum Chem. Phys.* (Elsevier, 2017) pp. 195–219.

[11] A. F. Oliveira, G. Seifert, T. Heine, and H. A. Duarte, *Density-functional based tight-binding: an approximate DFT method,* J. Braz. Chem. Soc. **20**, 1193 (2009).

[12] C. Bannwarth, S. Ehlert, and S. Grimme, *GFN2-xTB—An Accurate and Broadly Parametrized Self-Consistent Tight-Binding Quantum Chemical Method with Multipole Electrostatics and Density-Dependent Dispersion Contributions,* J. Chem. Theory Comput. **15**, 1652 (2019).

[13] J. Tomasi and M. Persico, *Molecular Interactions in Solution: An Overview of Methods Based on Continuous Distributions of the Solvent,* Chem. Rev. **94**, 2027 (1994).

[14] R. E. Skyner, J. L. McDonagh, C. R. Groom, T. van Mourik, and J. B. O. Mitchell, *A review of methods for the calculation of solution free energies and the modelling of systems in solution,* Phys. Chem. Chem. Phys. **17**, 6174 (2015).

[15] R. B. Sunoj and M. Anand, *Microsolvated transition state models for improved insight into chemical properties and reaction mechanisms,* Phys. Chem. Chem. Phys. **14**, 12715 (2012).

[16] C. J. Cramer and D. G. Truhlar, *Implicit Solvation Models: Equilibria, Structure, Spectra, and Dynamics,* Chem. Rev. **99**, 2161 (1999).

[17] J. Tomasi, B. Mennucci, and R. Cammi, *Quantum Mechanical Continuum Solvation Models,* Chem. Rev. **105**, 2999 (2005).

[18] A. V. Marenich, C. J. Cramer, and D. G. Truhlar, *Universal Solvation Model Based on Solute Electron Density and on a Continuum Model of the Solvent Defined by the Bulk Dielectric Constant and Atomic Surface Tensions,* J. Phys. Chem. B **113**, 6378 (2009).

[19] A. Klamt, F. Eckert, and W. Arlt, *COSMO-RS: An Alternative to Simulation for Calculating Thermodynamic Properties of Liquid Mixtures,* Annu. Rev. Chem. Biomol. Eng. **1**, 101 (2010).

[20] A. Klamt, *Conductor-like Screening Model for Real Solvents: A New Approach to the Quantitative Calculation of Solvation Phenomena,* J. Phys. Chem. **99**, 2224 (1995).

[21] A. Klamt, *The COSMO and COSMO☐RS solvation models,* WIREs Comput. Mol. Sci. **8** (2018), 10.1002/wcms.1338.

[22] B. J. Alder and T. E. Wainwright, *Studies in Molecular Dynamics. I. General Method,* J. Chem. Phys. **31**, 459 (1959).

[23] D. Frenkel and B. Smit, *Molecular Dynamics Simulations,* in *Underst. Mol. Simul.* (Elsevier, San Diego, 2002) 2nd ed., Chap. 4, pp. 63–82.

[24] C. J. Cramer, *Simulations of Molecular Ensembles,* in *Essent. Comput. Chem. Theor. Model.* (John Wiley & Sons, Ltd, West Sussex, 2002) Chap. 3, pp. 63–93.

[25] R. Iftimie, P. Minary, and M. E. Tuckerman, *Ab initio molecular dynamics: Concepts, recent developments, and future trends,* Proc. Natl. Acad. Sci. **102**, 6654 (2005).

[26] M. Iannuzzi, *Ab Initio Molecular Dynamics,* in *Comput. Methods Catal. Mater. Sci.*, edited by R. A. van Santen and P. Sautet (Wiley-VCH, Weinheim, 2009) Chap. 6, pp. 93–114.

[27] V. van Speybroeck and R. J. Meier, *A recent development in computational chemistry: chemical reactions from first principles molecular dynamics simulations,* Chem. Soc. Rev. **32**, 151 (2003).

[28] P. Labute, *LowModeMD—Implicit Low-Mode Velocity Filtering Applied to Conformational Search of Macrocycles and Protein Loops,* J. Chem. Inf. Model. **50**, 792 (2010).

[29] M. Jaraíz, *DFT-Based Microkinetic Simulations: A Bridge Between Experiment and Theory in Synthetic Chemistry,* (2020) pp. 81–105.

[30] M. Besora and F. Maseras, *Microkinetic modeling in homogeneous catalysis,* WIREs Comput. Mol. Sci. **8** (2018), 10.1002/wcms.1372.

[31] D. Vlachos, A. Mhadeshwar, and N. Kaisare, *Hierarchical multiscale model-based design of experiments, catalysts, and reactors for fuel processing,* (2006) pp. 9–27.

3

Composition- and Condition-dependent Kinetics

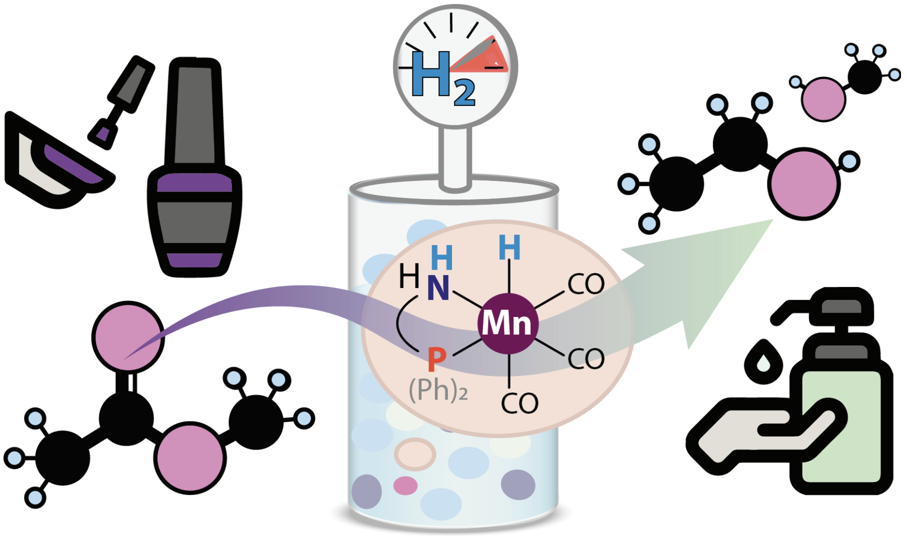

This chapter has been published in J. Phys. Chem. C **49**, 124 (2020) [1].

The reaction medium and conditions are the key parameters defining the efficiency and performance of a homogeneous catalyst. In the state of the art molecular descriptions of catalytic systems by density functional theory (DFT) calculations, the reaction medium is commonly reduced to an infinitely diluted ideal solution model. In this work we carry out a detailed operando computational modelling analysis of the condition-dependencies and non-ideal solution effects on the mechanism and kinetics of a model ester hydrogenation reactions by a homogeneous Mn(I)-P,N catalyst. An operando model aims to reflect realistic conditions and catalytic structures during the reaction that are accompanied by an established (complex) reaction network. By combining DFT calculations, COSMO-RS solvent model and the microkinetic modelling approach, the kinetic behaviour of the multicomponent homogeneous catalyst system under the realistic reaction conditions was investigated in detail. The effects of the reaction medium and its dynamic evolution in the course of the reaction were analysed by comparing the results obtained for the model methyl acetate hydrogenation reaction in a THF solution and under solvent-free neat reaction conditions. The dynamic representations of the reaction medium gives rise to strongly non-linear effects in the kinetic models. The non-ideal representation of the reaction medium results in pronounced condition-dependencies of the computed energetics of elementary reaction steps and the computed kinetic profiles, but affect only slightly such experimentally accessible kinetic descriptors as the apparent activation energy and degree of rate control.

3.1. Introduction

Homogeneous catalysis by transition metal complexes is an important strategy for the efficient and sustainable production of chemical products and intermediates used for pharmaceuticals, fragrances and fine chemicals.[2] Catalytic hydrogenation of unsaturated organic molecules with H_2 provides a highly atom efficient and green alternative to the conventional stoichiometric synthetic routes utilizing inorganic hydrides as the reducing agents.[3] The development of new efficient hydrogenation catalyst systems based on earth-abundant, inexpensive and biocompatible 3d metals is an important and active area of research.[4–8] Computations play an important role in modern catalysis and chemistry research by providing an atomistic framework to rationalize and support the experimental spectroscopic and reactivity studies[9, 10] and, increasingly in the recent years, to guide and support the experimental development and optimization of new and improved catalyst systems.[11–13]

Modern quantum chemistry and, in particular, density functional theory (DFT) methods provide with the practical and efficient computational tools to obtain a detailed insights into mechanisms of catalytic reactions, nature of key catalytic intermediates and transition states, and the associated energetics of the elementary steps.[14, 15] The prediction of geometries and properties of reaction intermediates is usually accurate and consistent among different functionals.[16] DFT is very powerful and efforts are continuously being made to develop more accurate computational methods based on new exchange-correlation functionals[17–19] and wave-function-based methods.[20]

When applied to practical problems of chemistry and catalysis, the computational accuracy is contributed by both the accuracy of the quantum chemical method and the accuracy/completeness of the chemical model used to represent the catalytic system in question.[21] The latter represents a particular challenge when simulating chemical processes in multicomponent concentrated reactive solutions commonly encountered in the practice of homogeneous catalysis. There is a substantial condition gap between the experiments with their highly complex multicomponent reaction systems and highly reduced computational models. Operando modelling approaches are being developed to close this gap and enable the detailed in silico analysis of the condition-dependencies in practical catalytic systems.

In applied computational catalysis, the reaction environment is commonly reduced to an oversimplified implicit ideal solvent models that does not account for all the solvation and complex medium effects.[22–24] Bridging the conditions gap between the experiment and the model is an important challenge on the way towards predictive catalysis modelling.[25] Development of computational approaches to analyse the effect of the multicomponent reaction environment that includes solvent, reactants as well as various promotors and additives is key to understanding the factors that define the catalytic performance. The choice of the reaction medium and conditions can determine whether the catalytic conversion takes place or not.[26, 27] It is therefore important to investigate how the variations in the representation of the reaction environment and its composition affect the macroand microscopic characteristics of a multicomponent catalytic reaction system.

Ester hydrogenation by homogeneous transition metal catalysts is an example of a highly complex multicomponent and multiphase catalyst system.[28–31] In the past catalytic systems based on ruthenium, iron, osmium and manganese have been investigated thoroughly.[28, 32–40] However, a vast majority of publications have been devoted to ester hydrogenation by Ru- or Fe-based catalysts.[37, 41–43] Following the first report by Beller and co-workers on a Mn-catalyst for the ester hydrogenation processes,[40] manganese has been in the focal area of homogeneous hydrogenation catalysis research in view of its abundance and biocompatibility.[44–47] For these systems, different mechanisms have been proposed and the presence of the solvent, additives and base seems to be crucial for the catalytic reaction.[6, 48] Because of the diversity in conditions and substrate scope it remains challenging to analyse their specific contributions to the reactivity of the catalyst. This highlights the need to switch to a more complex system description and analysis. One widely employed method to analyse catalytic systems under the reaction conditions (operando) is microkinetic modelling.[25] However, its application to homogeneous catalysis is still relatively scarce.[49] Our group has reported an ester hydrogenation catalytic system based on a non-pincer Mn-P,N catalyst, whose performance is defined by the multicomponent reaction environment (Figure 3.1).[45] Mechanistic studies combining DFT calculations and ab initio thermodynamic analysis of multicomponent reactive solutions[26] highlighted the role of the complexity of the reaction environment in such systems and put forward a hypothesis on the mechanistic role of the base promotors and the concentrated reaction medium in this system.[6] The base additive plays a role in both the catalyst activation and the catalytic ester conversion itself.[50, 51] Excess base helps removing trace amounts of water, aids substrate prearrangement and supplements to the entropic effects in base-assisted ester activation by Mn-P,N. Moreover, it has been proposed[6] that the inorganic base promotes the hydrogenolysis paths to reactivate the alkoxide resting state.

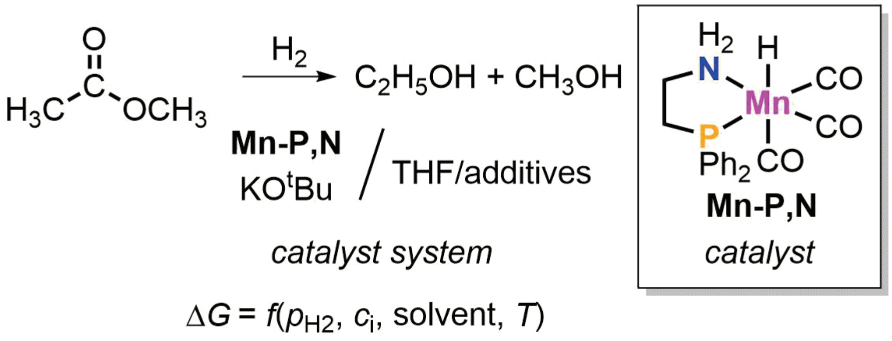

Figure 3.1: The definition of the condition space and the associated condition-dependent free energy surfaces for the catalytic ester hydrogenation reaction.

Previously, the operando modelling of the multicomponent solution has been used to analyse condition dependencies of the thermodynamics of competing reaction paths to identify potential deactivating channels and resting states.[6] The properties of the reaction environment dynamically changes in the course of the catalytic reaction from an ester (apolar, $\varepsilon(CH_3COOCH_3)_{298K}$ = 6.7)[52] to alcohol (polar, $\varepsilon(CH_3OH)_{298K}$ = 33.6, $\varepsilon(C_2H_5OH)_{298K}$ = 24.3).[53, 54] We anticipate that such an evolution of the medium and the associated condition-dependencies will affect the reaction kinetics as well. Therefore, in this study we examine the influence of different solvent descriptions on the computed reactivity of Mn-P,N-based ester hydrogenation system. This work reports the development of an operando DFT-based kinetic model accounting for the multicomponent and dynamic nature of the Mn-P,N homogeneous ester hydrogenation catalyst system. Four different approaches of varying complexity were considered to account for the solvation environment, as illustrated in Figure 3.2. The basic gas-phase model (GP) completely neglects the solvent environment.[55] The reaction components in this model are considered as separate non-interacting species, while the reaction conditions are accounted for here via the entropic and finite temperature corrections computed from statistical thermodynamics in the ideal gas approximation.[23] The *IS* model stands for ideal solution, in which bulk solvent effects are accounted for via the COSMO-RS implicit solvent model[56] but the components are considered as non-interacting. Here a mixed solvent model of THF and KOtBu base promotor was used to mimic the experimental conditions. However, in the experiments the substrates and the products account for a substantial fraction of the reaction mixture. During the catalytic reaction the ester substrate converts gradually to alcohol product. Together with the reaction environment, dielectric constants, hydrogen bonding patterns and the mode of solvation changes. The most important characteristic entails that as concentrations change, the change of properties are accounted for. To account for these effects, we introduced the concentration gradient corrections in

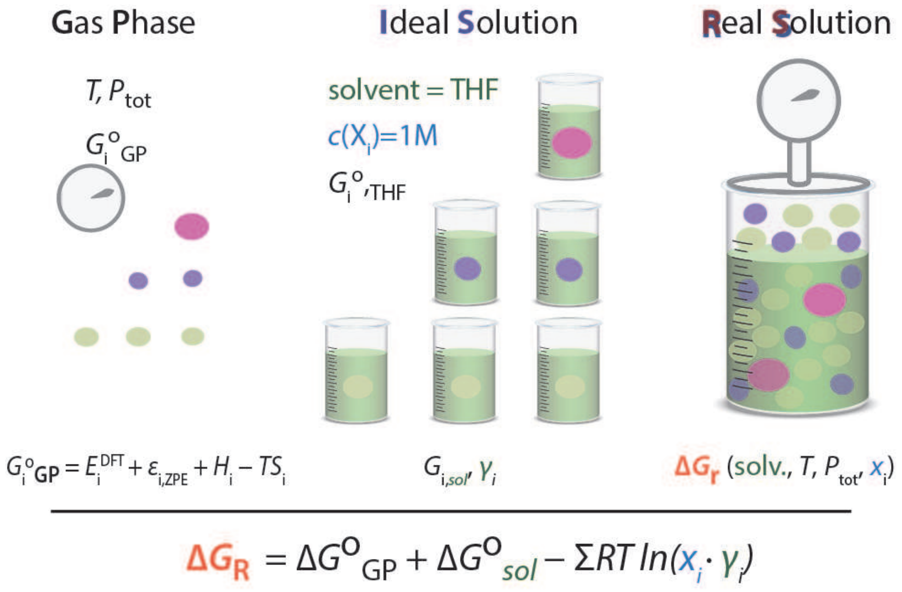

Figure 3.2: Models and approaches to concentration-dependent free energy surfaces.

the dynamic *RS* models for the reaction in THF solvent (*RS-THF*) and under solvent-free neat conditions (*RS-pure*). The starting solvent is a reactant that is being fully converted to another solvent that is the product, therefore changing the properties of the solution completely. In the fourth model we consider a complex model closest to the lab conditions under which the reactions are carried out (*RS-THF*). Mixed solvent model is considered with realistic concentrations of the reagents, and products as the reaction proceeds in THF as the basic solvent.

The chapter is organized in three sections. After describing the details of computational methodologies in section 2, results and discussion section 3 begins with the introduction of the two competitive mechanisms and the presentation of the standard DFT results for the respective reaction paths. This is followed by the discussion of the effect of the solvent model on the computed free energy profiles, which are further utilized to construct full condition-dependent microkinetic description of the system. The main findings and observations are summarized in the conclusion section 4.

3.2. Computational Details

Geometry optimization and frequency analysis for inter-mediates and transition states were carried out in the framework of the density functional theory (DFT) using the Gaussian16 C0.1 program.[57] The hybrid exchange-correlation functional PBE0[58] was used in combination with the 6-311+G(d,p) basis set on all atoms for geometry optimization and vibrational analysis. Van der Waals interactions are accounted for by the dispersion-corrected DFT-D3 (BJ) method.[59] The ultrafine grid was uniformly used. The nature of each stationary point was confirmed by frequency analysis, in which zero imaginary frequencies for minima and one for transition states. The single imaginary frequency has an eigenmode in the direction of the reaction coordinate. Reaction (ΔE) and activation energies ($\Delta E^{\ddagger}$) were corrected for zero-point energy (ZPE) from the normal-mode frequency analysis. Electronic energies (ΔE_{DFT}) and entropies (ΔS) were used for the calculations of the standard gas phase Gibbs free energies ($\Delta G°_{GP}$) at a temperature (T) of 373.15K. All vibrational modes were taken into account.

The solvation free energy contributions for the ideal solution approximation in THF (ΔG_{IS}) and the Gibbs free energies for the two real solution approximations (ΔG_{RS}) were computed with the COSMO-RS method.[60] The respective corrections were calculated using the COSMOthermX version C3.0 program[56] at the recommended BP86 level of theory. H_2 pressure was set in the calculations to the 50 bar that is the value used in the original experimental study.[45] The chemical composition of the ideal solution (*IS*) is composed of 0.75 mol KOtBu, 24.6 mol THF and 0.3 mol dodecane. For the real solution of the solvent free approximation (*RS-pure*), the starting reaction medium is composed of 0.1 mol KOtBu, 1 mol methyl acetate and 0.3 mol dodecane. The real solvent model including the THF solvent (*RS-THF*) is made up of 0.75 mol KOtBU, 24.6 mol THF, 1 mol methyl acetate and 0.3 mol dodecane.

For the microkinetic model an in-house python script was used and the reaction kinetics was derived for a batch-type reactor. Reaction rate constants were calculated using the Eyring equation. The differential equations were solved with the real-valued variable-coefficient ordinary differential equation solver (vode) embedded in the python SciPy package, with the backward differentiation formulas (BDF) implementation for stiff problems. The relative and absolute tolerances were set at 1e-8. Time integration until reaching steady state was applied. The initial conditions of the MKM were based on the experimental conditions with 1:0.05 ratio of methyl acetate to catalyst. The Gibbs free energy in gas or solvent were computed as outlined in Figure 3.1. Each solvent model and pathway were examined separately. To compute the kinetic profile of the dynamic reactions, the energy contributions were implemented as a function of alcohol product concentration. Standard conditions in the free energy analysis were defined as the conditions at the start of each catalytic cycle and they were kept unchanged during the microkinetic cycle. Apparent activation energies were calculated in a temperature range of 36K in five steps (345.5K; 363.8K; 373.15K; 382.5K; 392K). The reaction rates were determined in the initial phase of the reaction. To determine the degree of rate control, we examined the coefficient (χ_i) of every single elementary step in the reaction, defined by:

$$\chi_i = \left(\frac{\partial \ln r}{\partial \ln k_i}\right)_{k_j \neq k_i, K_i}$$

where r denotes the overall reaction rate, k_i the reaction rate constant of step i and K_i the equilibrium constant [61]. The rate constants were varied with factors between 0.996 and 1.004 (0.996; 0.998; 1; 1.002; 1.004).

3.3. Results and Discussion

3.3.1. Reaction mechanism

In line with the earlier mechanistic study, here we considered two competing reaction pathways for ester hydrogenation with the Mn-P,N catalyst denoted in Figure 3.3 as the hydrogen shuttle (HS) and the alkoxide (AX) mechanisms.[6, 45] Figure 3.4 presents the corresponding standard Gibbs free energy diagrams calculated in the GP approximation (ΔG°_{GP}). Both paths start with the coordination of the ester substrate to the Mn-H complex (**I**) forming a weak hydrogen-bonded complex **II**. The first step The subsequent hydride transfer to the carbonyl carbon is the most activated and endergonic step along the reaction path. It proceeds with a standard Gibbs free energy barrier of 102 kJ/mol and result in the intermediate **III**, which is 78 kJ/mol higher in energy than the starting configuration. Next, complex **III** coordinates molecular H_2 to form the σ-complex **IV**. The endergonic nature of this step (**III** + H_2 **–** **IV**, ΔG°_{GP} = 62 kJ/mol) is due the translational entropy loss and the change of Mn coordination from the trigonal pyramidal to the octahedral one upon the H_2 complexation. Subsequent heterolytic H_2 dissociation over Mn···gem-acetal acid-base pair yields state **V** featuring molecular acetaldehyde (AcH), methanol (MeOH) and the catalytic Mn-H species. Next, methanol is released from the reactive ensemble (**V–VI**) followed by a hydride transfer to AcH

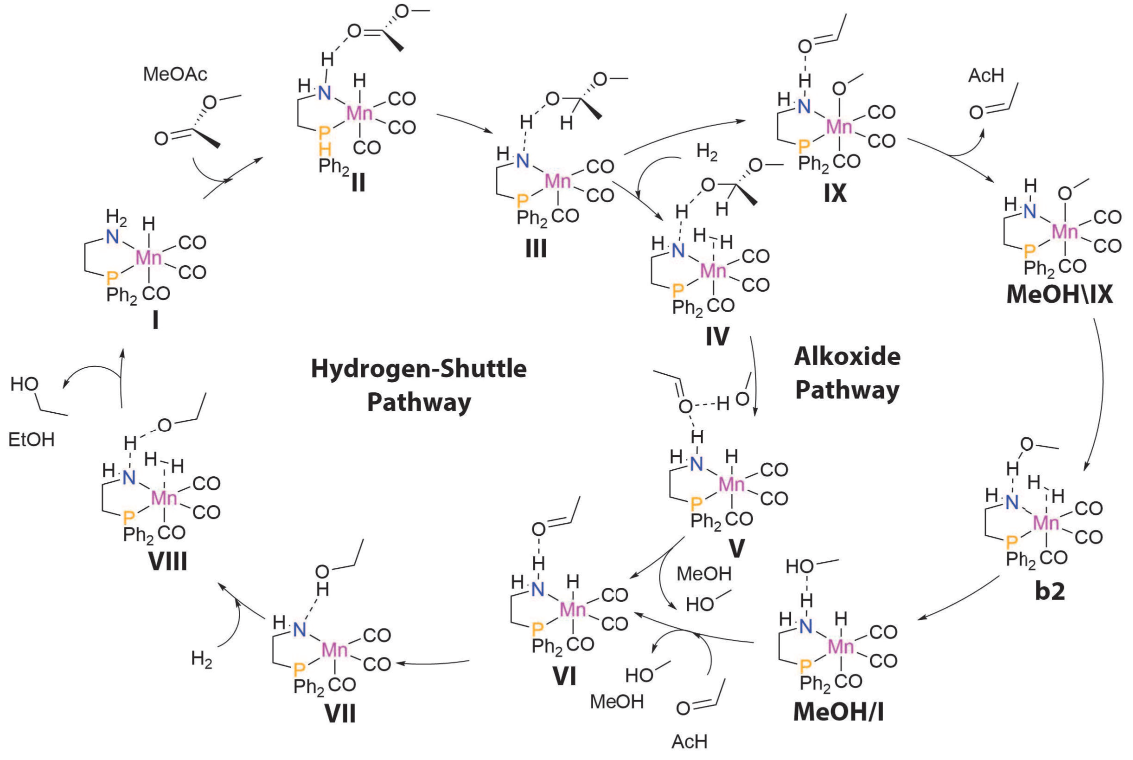

Figure 3.3: Mechanisms of the hydrogen-shuttle (HS) and alkoxide (AX) paths for a model methyl acetate ester hydrogenation with Mn-P,N catalyst I.

(**VI–VII**) that proceeds with a free energy barrier of only 13 kJ/mol. Both steps are exergonic and they decrease the standard Gibbs free energy of the system by 19 kJ/mol. The catalytic cycle is closed via an endergonic coordination of H_2 to the 5-coordinated Mn-center followed by a barrierless heterolytic H^2 cleavage upon which the methoxide moiety is protonated and the initial complex **I** is regenerated. The entire transformation proceeds with a change of free energy of -6 kJ mol^{-1}, which is in good agreement with the experimental thermochemistry data (-14 kJ mol^{-1}).[62]

The alternative AX path diverges from the HS channel after the formation of the gemacetal intermediate. In this path, the intermediate **III** undergoes a barrierless retroaldol transformation to form state **IX**. Release of AcH from **IX** produces an Mn-methoxide complex **MeOH/IX** that has previously been proposed as the resting state for the catalytic reaction.[45] Further transformation of this complex requires the replacement of the –OCH3 ligand with an H_2 molecule that is endergonic by 100 kJ/mol. However, as soon as the σ-H2 complex is formed, it dissociate barrierless to produce **MeOH/I**, which after the MeOH release promotes the reduction of AcH following the HS mechanism.

The direct comparison of these two different pathways and their computed energetics reveals that the HS pathway proceeds through fewer but more endergonic steps, while the AX pathway includes more elementary steps with relatively lower

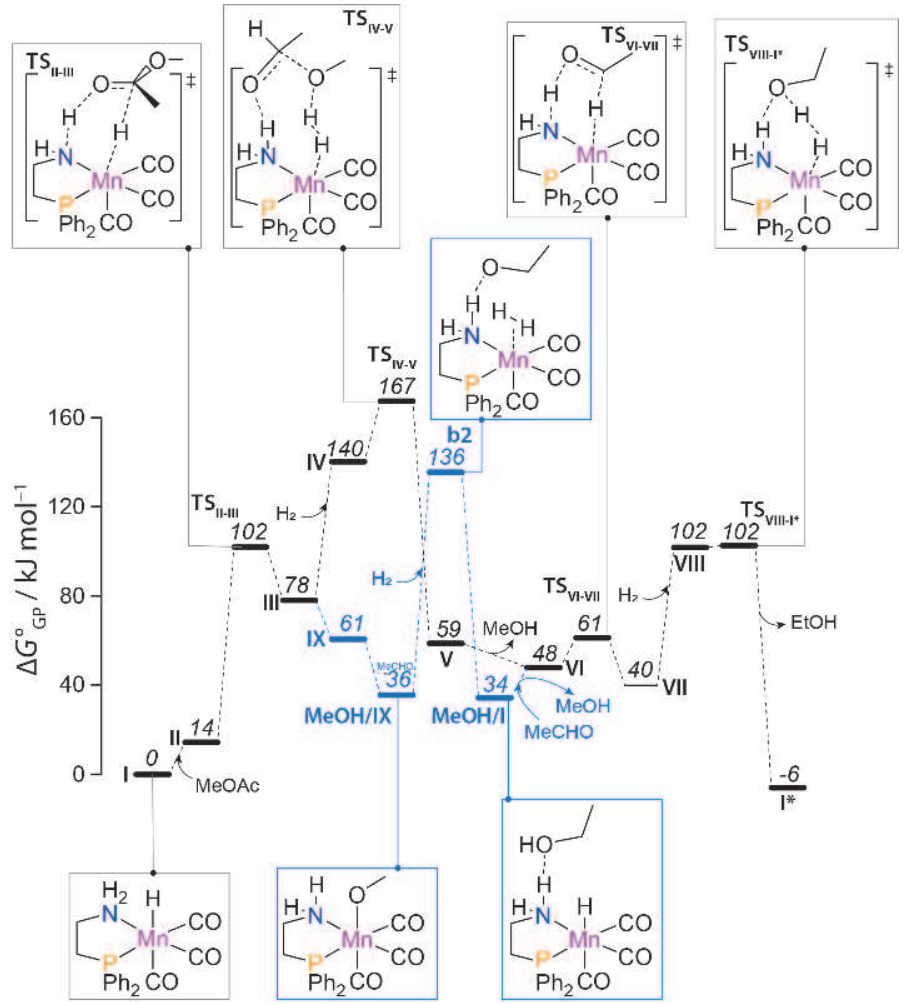

Figure 3.4: Standard Gibbs free energy diagrams for the HS (black) and AX (grey) pathways at 373 K computed using the *GP* model.

barriers. This suggests that the AX path should in principle be favoured. However, the current diagram were constructed using the gas-phase approximation, in which the solvation effects were not accounted for. Furthermore, the coordination and decoordination steps were assumed to be elementary within the diagrams. However, the closer look at the computed data reveals that the barrier heights for the elementary steps that do not account for the ligand exchange are comparable. Under the catalytic conditions the reaction rate will be defined by the whole reaction network and by the composition of the reaction medium.[63] In the next sections, we will separately address the effects of the reactive environment on the reaction energetics and the overall kinetics of the catalytic process.

3.3.2. Condition-dependent free energy surfaces

Three distinct solvation models, namely, the *IS*, *RS-THF*, and *RS-pure*, introduced in section 2 were considered here. The corresponding results for the HS and AX pathways are summarized in Figures 3.5a and b, respectively. The in vacuo results obtained with the *GP* model are also presented as a reference with grey dashed lines. In the ideal THF solution (*IS*) model, the solvent-corrected standard free energies (ΔG_{IS}) are obtained by correcting the *GP* results with the a estimated free energy of solvation (ΔG_{solv}) of each species in an infinitely diluted pure THF solution. The real solution (*RS*) model allows to account for the multicomponent nature of the solution and for the evolution of its composition in the course of the reaction. For the latter, denoted as the gradient correction, the *RS* solvent correction terms are computed at varied concentrations of the ester substrate and alcohol products. As a result, the computed energetics become a function of the conversion. The energies of the individual states along the reaction coordinates are now presented in the diagram as a range with a colour gradient showing the evolution of the reaction medium from low (light colour) to high (dark colour) conversion levels. We considered two situations, namely, when the reaction is carried out in a realistic THF solution (*RS-THF*) and solvent-free in neat ester (*RS-pure*). The medium composition and the reactions conditions do not change within each cycle to maintain the quasi-equilibrium that is required to obey the transition state theory.

The *IS* model shift the energetics of individual states by ΔΔG ranging from – 20 to +20 kJ/mol compared to the levels predicted within the *GP* approximation. The ΔΔG sign indicates relative stabilization and destabilization of the state in solution. The corrections are not uniform along the reaction coordinate. The *IS* correction affects only slightly (ΔΔG = 0 - +7 kJ/mol, Figure 3.5) the initial steps of ester coordination and activation (steps **I–III**). In the AX cycle (Figure 3.5b), also the subsequent conversion of **III–IX** and the formation of Mn-alkoxide complex (**MeOH/IX**) become less favourable within the *IS* model (Figure 4 3.5b). However, for the subsequent steps of the catalytic cycle a pronounced stabilizing effect of the solvent is observed (steps **IV–I***, Figure 3.5a; steps **b2**-**I**, Figure 3.5b). The *IS*-model consistently stabilizes the respective states by ΔΔG ranging from -25 to -75 kJ/mol. The overall hydrogenation reaction of ester to alcohol (**I–I***) is also more exergonic in the *IS* model compared to the *GP* model.

Next, we consider the effect of the dynamic reaction environment during the catalytic process using the gradient *RS*-models. The fundamental difference between the *IS* and the *RS*-models is that in the latter, the presence of all components of the reaction medium is explicitly taken into account when computing the solvent corrections. This results in a more pronounced destabilization of the initial ester activation steps within the *RS*-models. The results of the *RS-THF* model at low conversion levels resemble those obtained with the *IS* pure THF model. However, they deviate strongly for the intermediates with increasing ester conversion and, accordingly, the concentration for the alcohol product in the reaction medium. When the hydrogenation is carried out in neat ester substrate (*RS-pure*), the reaction proceeds over a wide range of compositions of the reaction medium, however the range of conditions is narrower. Similar to the *IS* model, the corrections as well as the energy ranges that they cover are not uniform along the reaction coordination. Both *RS*-models predict the that the favourability of the overall reaction decreases with the increasing ester conversion.

The *RS-THF* model also predicts a notable destabilization of the initial ester coordination steps (**I–III**) with ΔΔG = +6 – +31 due to solvation. Unlike the *IS* case considered above, the destabilization effect of *RS-THF* solvation is also observed the subsequent ester hydrogenolysis steps **III–IV** in the HS path (ΔΔG = +1 – +22, Figure 3.5), whereas it exerts a pronounced stabilization on the intermediates in the AX path (**MeOH/IX–MeOH/I**, ΔΔG = -26 – -1, Figure 3.5b). The effect of solvation on the subsequent aldehyde reduction (**VI–VIII**) varies with the conversion levels. Whereas the respective states are stabilized at low conversion levels, their energies gradually increase as the reaction progresses.

The *RS-pure* model represents the neat catalytic reaction. The reaction environment therefore drastically change in the course of the reaction from an ester to ethanol solution. Note, that the catalytic environment at all conversion levels is modelled as mixed solvent containing besides the substrate and the product also 10 mol.% KOtBu base promotor. The general trends observed with the *RS-pure* model resemble those established with the *RS-THF*, albeit with a more pronounced composition-dependency observed at each step. Here, the initial ester coordination (**I–III**) are destabilized by ΔΔG = +1 – +19). Here, the destabilizing effect is less pronounced than for the *RS-THF* model. A more pronounced effect of the *RS-pure* model is observed in the alkoxide formation and activation, where the species are significantly stabilized (**MeOH/IX–MeOH/I**, ΔΔG = -9 - -35, Figure 3.5b). During the aldehyde reduction the intermediates (**VI–VIII**) are, like in the *RS-THF* model, initially stabilized at lower ester conversion levels but destabilizes when the ester concentration increases in the mixture (ΔΔG = -19 – +10). The destabilizing effects are pronounced above 90% conversion in intermediates **V** and **VIII**, and between 50% and 70% conversion for intermediates **VI** and **VII**. The driving force of the *RS-pure* model is less pronounced than in the *RS-THF* model. In the *RS-THF* model the chemical potential along of the catalytic cycle is changed by ΔΔG = -60 to -16, while for *RS-pure* the ranges lies between ΔΔG = -44 to -10.

3.3.3. Microkinetic modelling

In the previous section, we demonstrate a profound impact of the composition of the reaction mixture on the relative stability of intermediates and transition states, and, accordingly on the heights of the free energy barriers and thermo-dynamics of the elementary steps as well as the overall ester hydrogenation process. In this section, the molecular in-sights of the different solvation models are converted into macroscopic observable reactivity parameters by a microkinetic model of the dynamic solution (MKM-DS) that explicitly accounts for the dynamic evolution of the reaction phase composition. Concentration-dependencies that have been identified in the *RS*-models are examined to investigate how these effects manifests themselves in the kinetic profiles. The reaction rates for the *GP*, *IS* and *RS*-models are presented as a function of ester conversion in Figures 3.6. The *GP*-model and the *IS*-model do not account for the changes in medium composition during the reaction and therefore predict a linear decrease of the reaction rate with the conversion. The *IS*-model yields a factor of 102-103 higher conversion rate via the HS path than

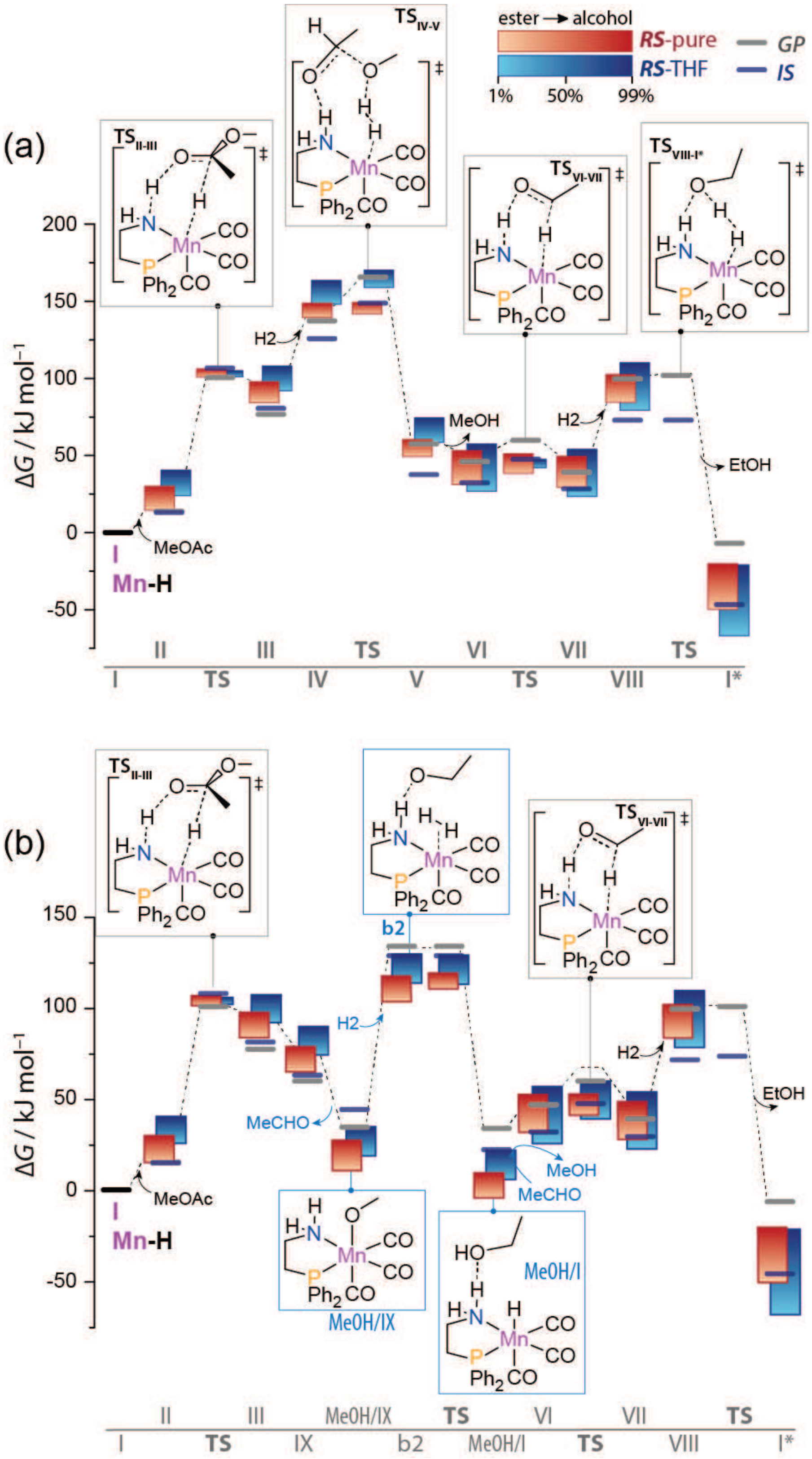

Figure 3.5: Standard *GP* and *IS*- as well as condition-dependent *RS* computed free energy diagrams of the (a) hydrogen-shuttle (HS) and (b) alkoxide reaction pathways. All four methods for calculating the energy contributions are displayed in the diagram.

the *GP*-model (Figure 3.6a). This is the direct consequence of the pronounced solvation of the key intermediates and transition states along the catalytic path. The stabilization by the solvent is particularly prominent for the highest-energy intermediate, **IV**, and the respective transition state, $TS_{\mathbf{IV\text{-}V}}$, along the HS pathway.

In the *RS-THF* model, at low and intermediate conversions, the rate linearly decreases with substrate depletion. However, at high conversion (X = 0.8–1) the changes in the composition and the polarity of the medium result in the substantial deviations from this trend in the AX pathway. The MKM-*RS* reveals a non-uniform effect of solvation on the relative preference of the two competing reaction paths. Although the *RS-THF* model yields a higher rate for the HS pathway than in the *GP*-model, for the AX pathway the *RS-THF* rate is 5-times slower than *GP* (Figure 3.6b). The *RS-pure* model yields a very different behaviour of the reaction rate with conversion than observed in the previous models. In the HS pathway (Figure 3.6a) the reaction rate starts to increase initially until it peaks at 50% conversion (X = 0.5). Then the rate declines rapidly. The kinetic profile mimics the evolution of the reaction barrier for the forward reaction of intermediate **VI** transforming to intermediate **VII**, which decreased rapidly after a conversion level of 50%. The effect observed at higher conversions is in line with that predicted in the *RS-THF* model. In the AX pathway (Figure 3.6b), the *RS-THF* model yields a similar shape reaction rate profile. The rate increases until ca. 50% conversion followed by a decline. This behaviour is not directly related to the evolution of any particular reaction energy barrier.

The comparison of the kinetic profiles for the *GP* model produced by the different solvation models points to a strong and non-linear effect of the composition of the reaction medium on the catalytic reaction. In line with the formal first order ester reduction, the idealized *GP* and *IS*-model show a beneficial effect of solvation on the reaction rate that decreases linearly with ester conversion. For all models, the catalytic reaction proceeds predominantly via the AX path with the competitive HS path showing much lower rates. For all models, the catalytic reaction proceeds predominantly via the AX path with the competitive HS path showing much lower rates. This can also be observed in the microkinetic model when both the AX and HS pathway are combined in a single MKM model. The AX models prevails for each solvent model by more than 99%. The *RS-THF* model exhibits minor deviations from the idealized linear behaviour that is most pronounced in the high conversion regime. For the *RS-pure* model, the abrupt changes in the solvation environment during the reaction manifests themselves in extreme kinetic effects. The reaction rate deviates strongly from the linear behaviour, which can be repatriated to swift changes in reaction barriers, especially at the low conversions. Importantly, these drastically different kinetic behaviours are not affecting one of the key experimental observable for the catalytic reaction, that is the apparent activation energy (E_{act}^{app}). Table 3.1 summarizes the MKM-derived E_{act}^{app} for the different models, reaction paths and at different conversion levels. The change in the reaction medium composition and the reaction path have a negligible effect on E_{act}^{app}. The *GP*-model yields an E_{act}^{app} of 55 kJ/mol, which is considerable smaller than that for the *IS* and

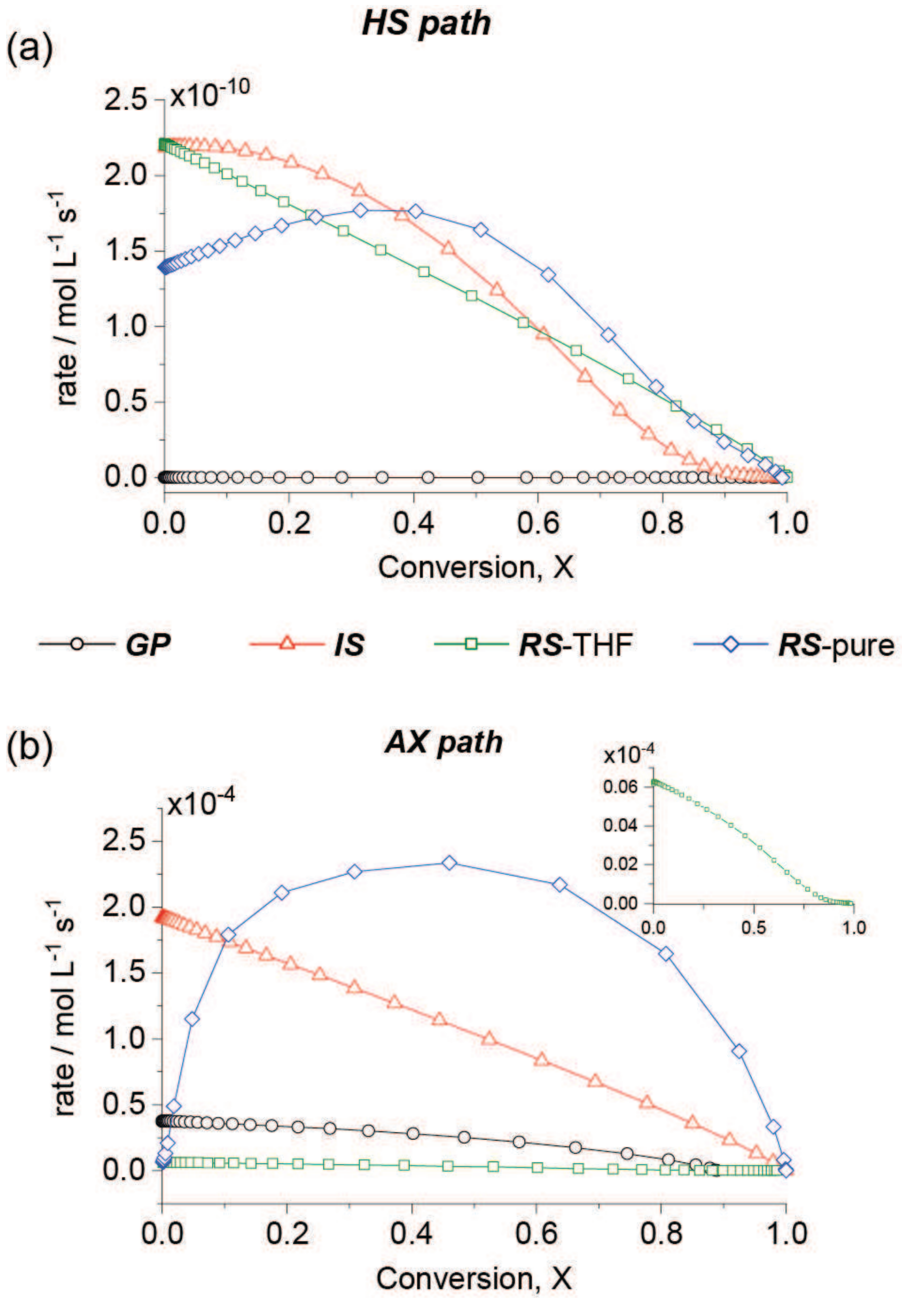

Figure 3.6: Kinetic profiles of the different solvation models in a) the HS pathway and b) the AX pathway. The reaction rate of alcohol production is plotted as a function of conversion.

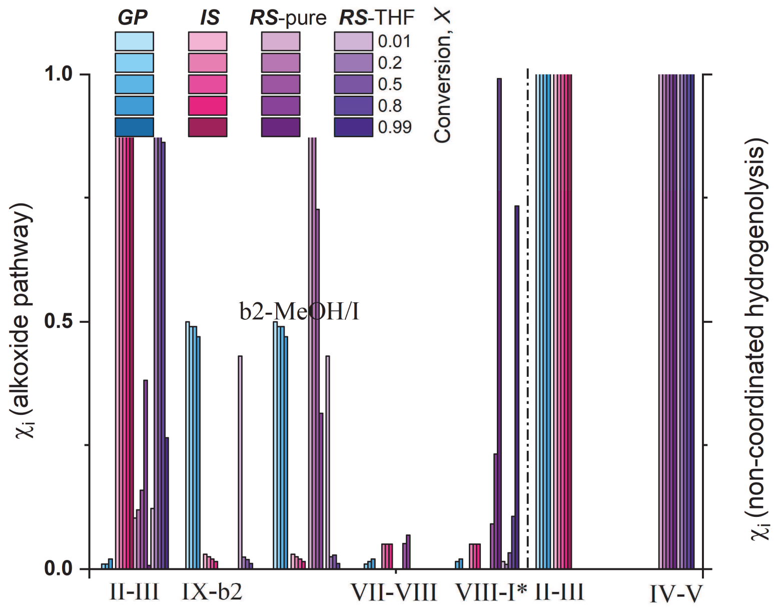

Figure 3.7: Bar diagram of degree of rate control in the AX pathway (left) and pathway proceeding through HS pathway (right). The steps contributing the most are shown for the four different methods at different points of conversions indicated by the colour scheme shown at the top. Note: The sum of the degree of rate control coefficients close to zero conversion is unity for both displayed pathways.

RS-models (65 kJ/mol and 68 kJ/mol, respectively). The large difference between the *GP* and solvation model results point to the importance of the initial ester coordination step for the overall reaction. Despite the less favourable ester activation in the *RS* models, the high reactivity in this case is probably due to more efficient promotion of the subsequent steps along the reaction path. It is also important to note that the apparent activation energy does not strictly correspond to the highest energy barrier but is a function of the free energy surface for the overall multistep mechanism. In the next sections a detailed analysis of the effects of the individual elementary steps on the overall kinetics is presented.

Next, we carried out a degree of rate control analysis to the influence of individual reaction steps on the overall reaction for the different models in the AX and HS pathway (Figure 3.7). The results of this analysis at different conversion levels are summarized in Figure 3.7. For the *GP* and *IS* model, in the HS path the initial ester hydrogenation (**II–III**) controls the rate at all conversions. For the *RS* solvation modes, the initial reduction of the ester by the absorbed hydrogen (**IV–V**) is the rate-determining steps. A more complex situation is revealed for the AX path. Whereas the alkoxide hydrogenolysis step (**IX–MeOH/I**) controls the rate in the *GP* model, for the reaction in THF solution (*IS*, *RS-THF*), the initial ester hydrogenation steps has the main contribution to the observed rate with a minor contribution of the alkoxide hydrogenolysis (**IX–MeOH/I**) and final ethanol production steps of the catalytic cycle (**VII–VIII**, **VIII–I***). For the pure solution (*RS-pure*), the methanol production step (**b2–MeOH/I**) has the greatest contribution. At higher conversions, the contribution of the latter steps increases for the *RS* models. This analysis further confirms that the initial ester activation is the key step in overall reaction with the alkoxide hydrogenolysis additionally contributing to the reaction especially for the idealized *GP* and *IS*-model.

Table 3.1: Apparent activation energies of the two pathways. Energies are given in kJ mol^{-1}.

	HS pathway				AX pathway			
Conversion	GP	IS	RS-pure	RS-THF	GP	IS	RS-pure	RS-THF
1%	55	66	66	68	57	66	66	68
20%	55	66	65	68	55	66	65	68
50%	55	66	65	68	55	66	65	67
80%	55	66	65	68	55	66	65	67
99%	55	66	65	68	55	66	65	67

3.4. Conclusion

In conclusion, we have investigated the effect of the dynamic evolution of the medium composition on the kinetics of homogeneous ester hydrogenation with Mn-P,N catalyst. Four different systems were analysed taking into account different descriptions of the solvent environment and the specific composition of the reaction medium. The effect of four different models on the reaction energies in different states of solvation was analysed. In the idealized *GP* and *IS* model the energies are stationary representing the gas phase corrections and corrections in a pure THF environment, respectively. The operando *RS-pure* and *RS-THF* models are used to include dynamic corrections and account for the changes of the reaction medium in the course of the reaction. The *RS-pure* model serves as an illustration of a reaction medium with reactants, products, additives and base present, while the *RS-THF* model portrays the reaction medium with THF present. In the models with stationary energies, reaction kinetics are linear, while the dynamic model display kinetics that depend on the change of the Gibbs free energy along the reaction coordinate. In the degree of rate control the *GP* model and *RS-pure* model stand out from the other three models as the recovery of the alkoxide is the rate-controlling step. This coincides with being the most energy-demanding step in these models. The apparent activation energies on the other hand have been found to be unaffected by the different corrections because of the assumption that the reaction conditions do not affect substantially the fundamental potential energy surface, while determining the free energy surfaces. From our investigation, we can conclude that while observing strong non-linear effects in the kinetic models of the dynamic representations, these effects may not manifest themselves within the macroscopic experimentally accessible kinetic descriptors. The *RS*-type descriptions of the solvent environment that explicitly accounts for the solvent composition are most representative to practical homogeneous catalyst systems used in the experimental studies.

Thus, our results demonstrate that the model accuracy of the computed parameters of homogeneous Mn-catalysed ester hydrogenation reaction depends on the choice of the system description. For predicting the macroscopic average reaction characteristics such as the apparent activation energy, all considered solvent descriptions give similar outcome. The kinetic behaviour of the catalyst systems and their microscopic characteristics, however, depend strongly on the chemical composition of the catalytic system and conditions, and should thus best be described with a realistic solvent model allowing for simulating dynamic mixed-solvent environments.

Elementary Reactions Steps

Below, the elementary reactions for the HS- and AX-pathway are summarized.

HS-pathway

$$\frac{d[I]}{dt} = -1 * (k_{I-II} * [I] * [ester] - k_{II-I} * [II]) + 1 * (k_{VIII-I} * [VIII] - k_{I-VIII} * [I] * [EtOH])$$

$$\frac{d[II]}{dt} = +1 * (k_{I-II} * [I] * [ester] - k_{II-I} * [II]) - 1 * (k_{II-III} * [II] - k_{III-II} * [III])$$

$$\frac{d[III]}{dt} = +1 * (k_{II-III} * [II] - k_{III-II} * [III]) - 1 * (k_{III-IV} * [III] - k_{IV-III} * [IV])$$

$$\frac{d[IV]}{dt} = +1 * (k_{III-IV} * [III] - k_{IV-III} * [IV]) - 1 * (k_{IV-V} * [IV] - k_{V-IV} * [V])$$

$$\frac{d[V]}{dt} = +1 * (k_{IV-V} * [IV] - k_{V-VI} * [V]) - 1 * (k_{V-VI} * [V] * [MeOH] - k_{VI-V} * [VI])$$

$$\frac{d[VI]}{dt} = +1 * (k_{V-VI} * [V] * [MeOH] - k_{VI-V} * [VI]) - 1 * (k_{VI-VII} * [VI] - k_{VII-VI} * [VII])$$

$$\frac{d[VII]}{dt} = +1 * (k_{VI-VII} * [VI] - k_{VII-VI} * [VII]) - 1 * (k_{VII-VIII} * [VII] - k_{VIII-VII} * [VIII])$$

$$\begin{aligned}\frac{d[VIII]}{dt} = {} & +1 * (k_{VII-VIII} * [VII] - k_{VIII-VII} * [VIII]) \\ & -1 * (k_{VIII-I} * [VIII] - k_{I-VIII} * [I] * [EtOH])\end{aligned}$$

$$\frac{d[ester]}{dt} = -1 * (k_{I-II} * [I] * [ester] - k_{II-I} * [II])$$

$$\frac{d[EtOH]}{dt} = +1 * (k_{VIII-I} * [VIII] - k_{I-VIII} * [I] * [EtOH])$$

$$\frac{d[MeOH]}{dt} = -1 * (k_{V-VI} * [V] * [MeOH] - k_{VI-V} * [VI])$$

AX-pathway

$$\frac{d[I]}{dt} = -1 * (k_{I-II} * [I] * [ester] - k_{II-I} * [II]) + 1 * (k_{VIII-I} * [VIII] - k_{I-VIII} * [I] * [EtOH])$$

$$\frac{d[II]}{dt} = +1 * (k_{I-II} * [I] * [ester] - k_{II-I} * [II]) - 1 * (k_{II-III} * [II] - k_{III-II} * [III])$$

$$\frac{d[III]}{dt} = +1 * (k_{II-III} * [II] - k_{III-II} * [III]) - 1 * (k_{III-IX} * [III] - k_{IX-III} * [IX])$$

$$\frac{d[IX]}{dt} = +1 * (k_{III-IX} * [III] - k_{IX-III} * [IX])$$
$$-1 * (k_{IX-MeOH} * [IX] - k_{MeOH-IX} * [MeOH] * [aldehyde])$$

$$\frac{d[MeOH]}{dt} = +1 * (k_{IX-MeOH} * [IX] - k_{MeOH-IX} * [MeOH] * [aldehyde])$$
$$-1 * (k_{MeOH-b2} * [MeOH] - k_{b2-MeOH} * [b2])$$

$$\frac{d[b2]}{dt} = +1 * (k_{MeOH-b2} * [MeOH] - k_{b2-MeOH} * [b2])$$
$$-1 * (k_{b2-MeOH} * [b2] - k_{MeOH-b2} * [MeOH])$$

$$\frac{d[MeOH]}{dt} = -1 * (k_{b2-MeOH} * [b2] - k_{MeOH-b2} * [MeOH])$$
$$+1 * (k_{MeOH-V} * [MeOH] * [aldehyde] - k_{V-MeOH} * [V])$$

$$\frac{d[VI]}{dt} = +1 * (k_{V-VI} * [V] * [MeOH] - k_{VI-V} * [VI]) - 1 * (k_{VI-VII} * [VI] - k_{VII-VI} * [VII])$$

$$\frac{d[VII]}{dt} = +1 * (k_{VI-VII} * [VI] - k_{VII-VI} * [VII]) - 1 * (k_{VII-VIII} * [VII] - k_{VIII-VII} * [VIII])$$

$$\frac{d[VIII]}{dt} = +1 * (k_{VII-VIII} * [VII] - k_{VIII-VII} * [VIII]) \\ -1 * (k_{VIII-I} * [VIII] - k_{I-VIII} * [I] * [EtOH])$$

$$\frac{d[ester]}{dt} = -1 * (k_{I-II} * [I] * [ester] - k_{II-I} * [II])$$

$$\frac{d[EtOH])}{dt} = +1 * (k_{VIII-I} * [VIII] - k_{I-VIII} * [I] * [EtOH]) \\ +1 * (k_{VIII-I} * [VIII] - k_{I-VIII} * [I] * [EtOH])$$

$$\frac{d[aldehyde]}{dt} = +1 * (k_{IX-MeOH} * [IX] - k_{MeOH-IX} * [MeOH] * [aldehyde]) \\ -1 * (k_{MeOH-V} * [MeOH] * [aldehyde] - k_{V-MeOH} * [V])$$

$$\frac{d[MeOH]}{dt} = -1 * (k_{V-VI} * [V] * [MeOH] - k_{VI-V} * [VI])$$

References

[1] A. M. Krieger, P. Kuliaev, F. Q. Armstrong Hall, D. Sun, and E. A. Pidko, *Composition- and Condition-Dependent Kinetics of Homogeneous Ester Hydrogenation by a Mn-Based Catalyst,* J. Phys. Chem. C **124**, 26990 (2020).

[2] L. Schober, *Sustainable synthesis of pharmaceuticals: using transition-metal complexes as catalysts,* Green Process. Synth. **7**, 558 (2018).

[3] C. Gunanathan and D. Milstein, *Applications of Acceptorless Dehydrogenation and Related Transformations in Chemical Synthesis,* Science (80-.). **341**, 1229712 (2013).

[4] T. Irrgang and R. Kempe, *3d-Metal Catalyzed N- and C-Alkylation Reactions via Borrowing Hydrogen or Hydrogen Autotransfer,* Chem. Rev. **119**, 2524 (2019).

[5] L. Alig, M. Fritz, and S. Schneider, *First-Row Transition Metal (De)Hydrogenation Catalysis Based On Functional Pincer Ligands,* Chem. Rev. **119**, 2681 (2019).

[6] W. Liu, B. Sahoo, K. Junge, and M. Beller, *Cobalt Complexes as an Emerging Class of Catalysts for Homogeneous Hydrogenations,* Acc. Chem. Res. **51**, 1858 (2018).

[7] D. Wei and C. Darcel, *Iron Catalysis in Reduction and Hydrometalation Reactions,* Chem. Rev. **119**, 2550 (2019).

[8] D. Formenti, F. Ferretti, F. K. Scharnagl, and M. Beller, *Reduction of Nitro Compounds Using 3d-Non-Noble Metal Catalysts,* Chem. Rev. **119**, 2611 (2019).

[9] J. P. Reid and M. S. Sigman, *Comparing quantitative prediction methods for the discovery of small-molecule chiral catalysts,* Nat. Rev. Chem. **2**, 290 (2018).

[10] M. G. Quesne, F. Silveri, N. H. de Leeuw, and C. R. A. Catlow, *Advances in Sustainable Catalysis: A Computational Perspective,* Front. Chem. **7** (2019), 10.3389/fchem.2019.00182.

[11] A. Nandy, J. Zhu, J. P. Janet, C. Duan, R. B. Getman, and H. J. Kulik, *Machine Learning Accelerates the Discovery of Design Rules and Exceptions in Stable Metal–Oxo Intermediate Formation,* ACS Catal. **9**, 8243 (2019).

[12] H. J. Kulik, *Making machine learning a useful tool in the accelerated discovery of transition metal complexes,* WIREs Comput. Mol. Sci. **10** (2020), 10.1002/wcms.1439.

[13] C. B. Santiago, J.-Y. Guo, and M. S. Sigman, *Predictive and mechanistic multivariate linear regression models for reaction development,* Chem. Sci. **9**, 2398 (2018).

[14] K. D. Vogiatzis, M. V. Polynski, J. K. Kirkland, J. Townsend, A. Hashemi, C. Liu, and E. A. Pidko, *Computational Approach to Molecular Catalysis by 3d Transition Metals: Challenges and Opportunities,* Chem. Rev. **119**, 2453 (2019).

[15] S. J. Klippenstein, V. S. Pande, and D. G. Truhlar, *Chemical Kinetics and Mechanisms of Complex Systems: A Perspective on Recent Theoretical Advances,* J. Am. Chem. Soc. **136**, 528 (2014).

[16] A. J. Cohen, P. Mori-Sánchez, and W. Yang, *Challenges for Density Functional Theory,* Chem. Rev. **112**, 289 (2012).

[17] S.-C. Qi, J.-i. Hayashi, and L. Zhang, *Recent application of calculations of metal complexes based on density functional theory,* RSC Adv. **6**, 77375 (2016).

[18] E. Brémond, I. Ciofini, J. C. Sancho-García, and C. Adamo, *Nonempirical Double-Hybrid Functionals: An Effective Tool for Chemists,* Acc. Chem. Res. **49**, 1503 (2016).

[19] T. M. Maier, A. V. Arbuznikov, and M. Kaupp, *Local hybrid functionals: Theory, implementation, and performance of an emerging new tool in quantum chemistry and beyond,* Wiley Interdiscip. Rev. Comput. Mol. Sci. **9**, e1378 (2019).

[20] S. Ghosh, P. Verma, C. J. Cramer, L. Gagliardi, and D. G. Truhlar, *Combining Wave Function Methods with Density Functional Theory for Excited States,* Chem. Rev. **118**, 7249 (2018).

[21] E. A. Pidko, *Toward the Balance between the Reductionist and Systems Approaches in Computational Catalysis: Model versus Method Accuracy for the Description of Catalytic Systems,* ACS Catal. **7**, 4230 (2017).

[22] B. Mennucci and R. Cammi, eds., *Continuum Solvation Models in Chemical Physics* (John Wiley & Sons, Ltd, Chichester, UK, 2007).

[23] C. J. Cramer and D. G. Truhlar, *Implicit Solvation Models: Equilibria, Structure, Spectra, and Dynamics,* Chem. Rev. **99**, 2161 (1999).

[24] C. J. Cramer and D. G. Truhlar, *A Universal Approach to Solvation Modeling,* Acc. Chem. Res. **41**, 760 (2008).

[25] L. Grajciar, C. J. Heard, A. A. Bondarenko, M. V. Polynski, J. Meeprasert, E. A. Pidko, and P. Nachtigall, *Towards operando computational modeling in heterogeneous catalysis,* Chem. Soc. Rev. **47**, 8307 (2018).

[26] P. O. Kuliaev and E. A. Pidko, *Operando Modeling of Multicomponent Reactive Solutions in Homogeneous Catalysis: from Non-standard Free Energies to Reaction Network Control,* ChemCatChem **12**, 795 (2020).

[27] Y. Kim, J. R. Mohrig, and D. G. Truhlar, *Free-Energy Surfaces for Liquid-Phase Reactions and Their Use To Study the Border Between Concerted and Nonconcerted α,β-Elimination Reactions of Esters and Thioesters,* J. Am. Chem. Soc. **132**, 11071 (2010).

[28] S. Werkmeister, K. Junge, and M. Beller, *Catalytic Hydrogenation of Carboxylic Acid Esters, Amides, and Nitriles with Homogeneous Catalysts,* Org. Process Res. Dev. **18**, 289 (2014).

[29] J. Pritchard, G. A. Filonenko, R. van Putten, E. J. M. Hensen, and E. A. Pidko, *Heterogeneous and homogeneous catalysis for the hydrogenation of carboxylic acid derivatives: history, advances and future directions,* Chem. Soc. Rev. **44**, 3808 (2015).

[30] P. A. Dub, R. J. Batrice, J. C. Gordon, B. L. Scott, Y. Minko, J. G. Schmidt, and R. F. Williams, *Engineering Catalysts for Selective Ester Hydrogenation,* Org. Process Res. Dev. **24**, 415 (2020).

[31] P. A. Dub and T. Ikariya, *Catalytic Reductive Transformations of Carboxylic and Carbonic Acid Derivatives Using Molecular Hydrogen,* ACS Catal. **2**, 1718 (2012).

[32] W. Kuriyama, T. Matsumoto, O. Ogata, Y. Ino, K. Aoki, S. Tanaka, K. Ishida, T. Kobayashi, N. Sayo, and T. Saito, *Catalytic Hydrogenation of Esters. Development of an Efficient Catalyst and Processes for Synthesising (R)-1,2-Propanediol and 2-(l-Menthoxy)ethanol,* Org. Process Res. Dev. **16**, 166 (2012).

[33] D. Spasyuk, S. Smith, and D. G. Gusev, *Replacing Phosphorus with Sulfur for the Efficient Hydrogenation of Esters,* Angew. Chemie **125**, 2598 (2013).

[34] G. A. Filonenko, M. J. B. Aguila, E. N. Schulpen, R. van Putten, J. Wiecko, C. Müller, L. Lefort, E. J. M. Hensen, and E. A. Pidko, *Bis-N-heterocyclic Carbene Aminopincer Ligands Enable High Activity in Ru-Catalyzed Ester Hydrogenation,* J. Am. Chem. Soc. **137**, 7620 (2015).

[35] T. Zell, Y. Ben-David, and D. Milstein, *Unprecedented Iron-Catalyzed Ester Hydrogenation. Mild, Selective, and Efficient Hydrogenation of Trifluoroacetic Esters to Alcohols Catalyzed by an Iron Pincer Complex,* Angew. Chemie **126**, 4773 (2014).

[36] S. Chakraborty, H. Dai, P. Bhattacharya, N. T. Fairweather, M. S. Gibson, J. A. Krause, and H. Guan, *Iron-Based Catalysts for the Hydrogenation of Esters to Alcohols,* J. Am. Chem. Soc. **136**, 7869 (2014).

[37] D. Spasyuk, S. Smith, and D. G. Gusev, *From Esters to Alcohols and Back with Ruthenium and Osmium Catalysts,* Angew. Chemie **124**, 2826 (2012).

[38] A. Mukherjee, A. Nerush, G. Leitus, L. J. W. Shimon, Y. Ben David, N. A. Espinosa Jalapa, and D. Milstein, *Manganese-Catalyzed Environmentally Benign Dehydrogenative Coupling of Alcohols and Amines to Form Aldimines and H2: A Catalytic and Mechanistic Study,* J. Am. Chem. Soc. **138**, 4298 (2016).

[39] M. Mastalir, M. Glatz, N. Gorgas, B. Stöger, E. Pittenauer, G. Allmaier, L. F. Veiros, and K. Kirchner, *Divergent Coupling of Alcohols and Amines Catalyzed by Isoelectronic Hydride Mn I and Fe II PNP Pincer Complexes,* Chem. - A Eur. J. **22**, 12316 (2016).

[40] S. Elangovan, M. Garbe, H. Jiao, A. Spannenberg, K. Junge, and M. Beller, *Hydrogenation of Esters to Alcohols Catalyzed by Defined Manganese Pincer Complexes,* Angew. Chemie **128**, 15590 (2016).

[41] A. Zirakzadeh, K. Kirchner, A. Roller, B. Stöger, M. D. Carvalho, and L. P. Ferreira, *Synthesis, coordination behavior and structural features of chiral iron(II) PNP diferrocene complexes,* RSC Adv. **6**, 11840 (2016).

[42] D. G. Gusev, *Dehydrogenative Coupling of Ethanol and Ester Hydrogenation Catalyzed by Pincer-Type YNP Complexes,* ACS Catal. **6**, 6967 (2016).

[43] D. Kim, L. Le, M. J. Drance, K. H. Jensen, K. Bogdanovski, T. N. Cervarich, M. G. Barnard, N. J. Pudalov, S. M. M. Knapp, and A. R. Chianese, *Ester Hydrogenation Catalyzed by CNN-Pincer Complexes of Ruthenium,* Organometallics **35**, 982 (2016).

[44] G. A. Filonenko, R. van Putten, E. J. M. Hensen, and E. A. Pidko, *Catalytic (de)hydrogenation promoted by non-precious metals – Co, Fe and Mn: recent advances in an emerging field,* Chem. Soc. Rev. **47**, 1459 (2018).

[45] R. van Putten, E. A. Uslamin, M. Garbe, C. Liu, A. Gonzalez-de Castro, M. Lutz, K. Junge, E. J. M. Hensen, M. Beller, L. Lefort, and E. A. Pidko, *Non-Pincer-Type Manganese Complexes as Efficient Catalysts for the Hydrogenation of Esters,* Angew. Chemie Int. Ed. **56**, 7531 (2017).

[46] D. H. Nguyen, X. Trivelli, F. Capet, J.-F. Paul, F. Dumeignil, and R. M. Gauvin, *Manganese Pincer Complexes for the Base-Free, Acceptorless Dehydrogenative Coupling of Alcohols to Esters: Development, Scope, and Understanding,* ACS Catal. **7**, 2022 (2017).

[47] M. B. Widegren, G. J. Harkness, A. M. Z. Slawin, D. B. Cordes, and M. L. Clarke, *A Highly Active Manganese Catalyst for Enantioselective Ketone and Ester Hydrogenation,* Angew. Chemie Int. Ed. **56**, 5825 (2017).

[48] A. Chowdhury, S. Biswas, A. Pramanik, and P. Sarkar, *Mechanistic insights into the non-bifunctional hydrogenation of esters by Co(II) pincer complexes: a DFT study,* Dalt. Trans. **48**, 16083 (2019).

[49] S. C. Mandal, K. S. Rawat, S. Nandi, and B. Pathak, *Theoretical insights into CO 2 hydrogenation to methanol by a Mn–PNP complex,* Catal. Sci. Technol. **9**, 1867 (2019).

[50] P. A. Dub and J. C. Gordon, *The role of the metal-bound N–H functionality in Noyori-type molecular catalysts,* Nat. Rev. Chem. **2**, 396 (2018).

[51] P. A. Dub, N. J. Henson, R. L. Martin, and J. C. Gordon, *Unravelling the Mechanism of the Asymmetric Hydrogenation of Acetophenone by [RuX2(diphosphine)(1,2-diamine)] Catalysts,* J. Am. Chem. Soc. **136**, 3505 (2014).

[52] C. Wohlfarth, *Dielectric constant of methyl acetate,* (2008) pp. 171–171.

[53] *Methanol Dielectric Constant: Datasheet from "Dortmund Data Bank (DDB) – Thermophysical Properties Edition 2014" in SpringerMaterials (https://materials.springer.com/thermophysical/docs/dec_c110),* .

[54] *Ethanol Dielectric Constant: Datasheet from "Dortmund Data Bank (DDB) – Thermophysical Properties Edition 2014" in SpringerMaterials (https://materials.springer.com/thermophysical/docs/dec_c11),* .

[55] J. W. Ochterski, *Thermochemistry in Gaussian,* (2000).

[56] A. Klamt, *Conductor-like Screening Model for Real Solvents: A New Approach to the Quantitative Calculation of Solvation Phenomena,* J. Phys. Chem. **99**, 2224 (1995).

[57] M. J. Frisch, G. W. Trucks, H. B. Schlegel, G. E. Scuseria, M. A. Robb, J. R. Cheeseman, G. Scalmani, V. Barone, G. A. Petersson, H. Nakatsuji, X. Li, M. Caricato, A. V. Marenich, J. Bloino, B. G. Janesko, R. Gomperts,

B. Mennucci, H. P. Hratchian, J. V. Ortiz, A. F. Izmaylov, J. L. Sonnenberg, D. Williams-Young, F. Ding, F. Lipparini, F. Egidi, J. Goings, B. Peng, A. Petrone, T. Henderson, D. Ranasinghe, V. G. Zakrzewski, J. Gao, N. Rega, G. Zheng, W. Liang, M. Hada, M. Ehara, K. Toyota, R. Fukuda, J. Hasegawa, M. Ishida, T. Nakajima, Y. Honda, O. Kitao, H. Nakai, T. Vreven, K. Throssell, J. A. Montgomery Jr., J. E. Peralta, F. Ogliaro, M. J. Bearpark, J. J. Heyd, E. N. Brothers, K. N. Kudin, V. N. Staroverov, T. A. Keith, R. Kobayashi, J. Normand, K. Raghavachari, A. P. Rendell, J. C. Burant, S. S. Iyengar, J. Tomasi, M. Cossi, J. M. Millam, M. Klene, C. Adamo, R. Cammi, J. W. Ochterski, R. L. Martin, K. Morokuma, O. Farkas, J. B. Foresman, and D. J. Fox, *Gaussian16 Revision C.01,* (2016).

[58] C. Adamo and V. Barone, *Toward reliable density functional methods without adjustable parameters: The PBE0 model,* J. Chem. Phys. **110**, 6158 (1999).

[59] S. Grimme, S. Ehrlich, and L. Goerigk, *Effect of the damping function in dispersion corrected density functional theory,* J. Comput. Chem. **32**, 1456 (2011).

[60] A. Klamt, *The COSMO and COSMO-RS solvation models,* WIREs Comput. Mol. Sci. **1**, 699 (2011).

[61] C. T. Campbell, *The Degree of Rate Control: A Powerful Tool for Catalysis Research,* ACS Catal. **7**, 2770 (2017).

[62] P. Linstrom, *NIST chemistry WebBook, NIST standard reference database 69,* (1997).

[63] O. N. Temkin, *Effect of Medium on Reaction Rates in Homogeneous Catalysis with Metal Complexes,* in *Homog. Catal. with Met. Complexes* (John Wiley & Sons, Ltd, Chichester, UK, 2012) pp. 741–796.

4

Metal-Ligand Cooperative Activation

This chapter has been published in Z. Anorg. Allg. Chem. **647** (2021) [1].

Reversible dissociation of the H-X bond (M-L + H-X -> M(X)-L(H); ΔG_{HX}) is an important step during preactivation, catalysis and possible deactivation of acid-base cooperative pincer based transition metal catalysts (M-L). Herein we carried out a high-throughput computational investigation of the thermodynamic stability of different adducts in various functionalized Mn(I) based pincer complexes. We used a combination of density functional theory (DFT) and density functional tight binding (DFTB) calculations to analyse ΔG_{HX} of more than 700 M(X)-L(H) intermediates based on functionalized variants of four pincer type ligand scaffolds derived from PCP, CNC, PNP and SNS ligands. We discovered linear scaling relations between ΔG_{HX} of various species. Strongest correlations were found between species of similar size and chemical nature e.g. ΔG_{tBuOH} correlated best with ΔG_{iPrOH} and worst with ΔG_{HBr}. Such scaling relations can be useful for property based screening of catalysts and selection of (co)solvent/substrate/base for optimized reaction conditions. We also investigated the influence of the ligand backbone and the functionalization of donor and backbone sites in the ligand. Our analysis reveals the crucial role of the second coordination sphere functionalization for the reactivity of the complexes with impact in some cases exceeding that of the variation of the functional groups directly attached to the donor atoms.

4.1. Introduction

Pincer complexes are important catalysts in organometallic chemistry for multiple applications such as transformation and synthesis of imines, amines, peptides, pyridines, pyrroles, acetals, and carboxylic acid derivatives, such as esters, ketones and amides.[2–4] Owing to their success with (de)hydrogenation of a wide scope of substrates, pincer complexes have been adopted favourably by the pharmaceutical, fine chemicals and the energy industry[5] (representative examples shown in Figure 4.1a and b). The well-defined geometry and tridentate coordination mode of this class of complexes offers a stable catalytic structure. Most highly active pincers such as Ru-MACHO complex[6, 7] and Nozaki's Ir-PNP complex[8] are based on expensive Ru and Ir metals. Catalytic systems based on such metals are not desirable for large scale ubiquitous applications due to high cost and limited availability. Several successful examples of pincer catalysts based on earth abundant 3d transition metals (TMs) such as Fe and Mn have been realized in the last decade.[9, 10] However, the activity and stability of such catalysts based on first row TMs remains a challenge. Therefore, the development and optimization of catalysts based on 3d transition metals is an active and highly sought after area of research.[11–13] Manganese is particularly attractive as the active metal in such catalysts in view of its high biocompatibility, which is of interest for industries in the food or pharmaceutical sector.

Functionalization of the ligand scaffold can be used to explore the chemical space of TM pincers in the pursuit of highly active and stable catalysts based on first row TMs. In such an approach one can start with a ”skeleton” complex bearing a TM centre coordinated to a pincer scaffold. Selected sites on the scaffold or metal centre can be functionalized generating an ensemble of new TM complexes using various combinations of functional groups.[14–17] Experimentally only a handful of functionalized variants of pincer ligand scaffolds have been reported. Moreover, synthesis and subsequent testing of the catalytic activity of functionalized TM complexes quickly becomes intractable. Theoretical consideration of the functionalized variants that are synthetically not accessible can provide an insight into rational design principles. In this regard, computational methods are relevant and can be applied to screen through a large ensembles of functionalized TM complexes.[18, 19] Recently such approaches have been applied to screen TM complex including pincer complexes for activity, regioselectivity and ligand effects.[20–22]

Herein we screened the effect of functionalization of the ligand backbone on the stability of potential catalytic intermediates on Mn(I)-pincer complexes. The focus was on the determination the effect of the type of functionalization and the functionalization site (backbone/donor site). By choosing functionalization sites directly coordinated to the Mn(I)-centre, the effect of the first coordination sphere can be analysed. The effect of the second coordination sphere is rationalized by investigating functionalization on a site not directly coordinated to the metal. We chose five representative pincer ligand scaffolds, namely, PNP-(bis(3-phosphaneylpropyl)amine)-, SNS-(azanediylbis(ethane-1-thiol))-, CNC-(bis(2-(1H-3λ^4-imidazol-3-yl)ethyl)amine)-, PNN-(N^1-(2-phosphaneylethyl)ethane-1,2-diamine)-, and PCP-(N^1,N^3 - bis(phosphaneyl)benzene-1,3-diamine)- backbones coordinated to a Mn(I) centre stabilized by CO ligands as illustrated in Figure 4.1c. Our analysis included the pristine complexes as well as their catalytically relevant intermediates resulting in over 1200 structures based on the five selected pincer ligand scaffolds (Figure 4.1c). Pincer complexes based on these ligands have been reported for various transition metals, including manganese (Figure 4.1b).[9, 14, 23–32] SNS-,[33–38] CNC-,[39–44] PNP,[45] and PCP-ligands[46–50] are primarily known for their use in 4d- and 5d-transition metal catalysis (Figure 4.1a). Especially in 4d- and 5d-transition metal catalysis high turnover frequencies and turnover numbers are reported for the complexes.[32, 41, 43, 51]

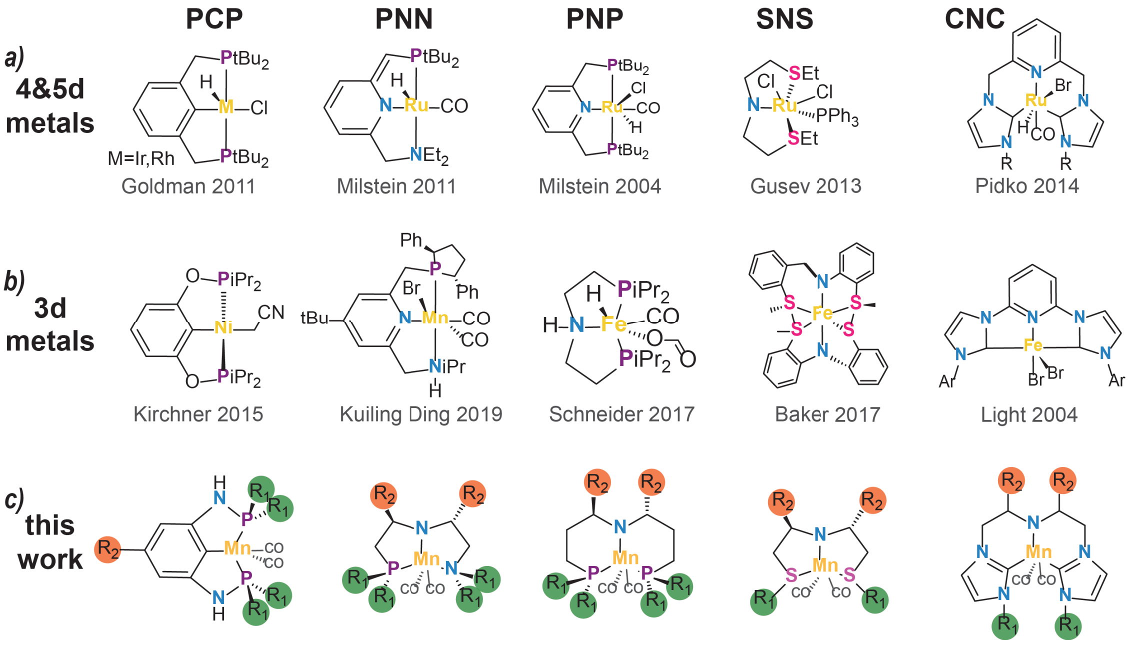

Figure 4.1: Representative transition metal pincer complexes of (a) 4d, 5d and (b) 3d metals, followed by (c) the catalyst scope of this work.

Literature on 3d-transition metals generally reports lower catalytic efficiencies,[31, 50] which indicates that there is opportunity to maximize their potential towards sustainable catalyst systems. Catalysts based on 3d metals are known to be more prone to deactivation and formation of resting states, limiting their reactivity.[5, 49]

Herein, we investigated Mn(I) -pincers as potential (de)hydrogenation catalysts. Possible applications are the storage of H_2 in unsaturated moieties such as CO_2, the reduction of organic substrates with H_2 gas or with hydrogen donors such as iPrOH.[52–54] Figure 4.2 illustrates representative catalytic cycles of dehydrogenation of methanol to acetone and hydrogenation of acetone to isopropanol. The Br adduct M(Br)–L(H) is a common precursor to the active form of Mn-pincers.[12] The activation of the catalyst is commonly carried out by the reaction with a strong base (e.g. KOH or KOtBu). This yields a 5-coordinated complex (M–L), regarded as a pristine activated catalyst and which features a Lewis acid site on the metal and the ligand can act as a Brønsted base i.e. the metal can coordinate with an electron donating species while the ligand can accept a H^+. The activated catalyst is susceptible for potential deactivation/inhibition through the metal-ligand cooperative addition of alcohol/water/base resulting in the formation of -OR adducts.[55] Alkoxide adduct of hydrogen donating alcohols such iPrOH, MeOH and EtOH are often formed as intermediates in the course of catalytic hydrogenation reactions, and can even act as the resting states limiting the catalytic performance depending on their stability.[49, 56–61] Competitive bonding of other species such as the solvent or the nucleophile base to the metal can slow down or even deactivate the catalyst.

For example, water can compete with methanol for the catalytically active site via the formation of a stable hydroxide adduct upon reaction with the catalyst or via ligand exchange with the methoxide adduct (Figure 4.2). To continue the catalytic cycle, the alkoxide adduct must convert to the hydride adduct M(H)-L(H), which in turn regenerates the catalyst by hydrogen evolution/transfer. Catalytic turnover is inhibited if the alkoxide adducts is very stable compared to the hydride adduct. Similarly, an excessively stable hydride adduct would render it inactive towards hydrogen liberation resulting in an adverse effect on the catalysis.

When employed as a hydrogenation catalysis, the hydride adduct is formed as the first step via heterolytic H_2 dissociation. A less stable hydride would be prone to H_2 recombination instead of catalytic turnover. On the other hand, excessive hydride stability would make it less reactive towards the hydride transfer steps of the catalytic cycle. The alkoxide adduct formed upon the hydride transfer to C=O must dissociate to regenerate the catalyst. Transfer hydrogenation reactions with e.g. isopropanol often proceeds via the formation of an intermediate alkoxide species. Excessive stability of this alkoxide adduct would have a deactivating effect and adversely affect the catalytic turnover. From a mechanistic perspective the relative stability of hydride, hydroxide and alkoxides intermediates are important for the catalytic turnover. Their relative stability, in accordance with the Sabatier's principle should be balanced and any excessive stabilization/destabilization would have an inhibiting effect on the catalyst.

In the present work we investigate functional strategies to tune the stability of aforementioned intermediates. Our results allow comparison of different ligand scaffolds and functionalization strategies in a common framework. We have identified linear free energy scaling relations between various intermediates. By analyzing relative stabilities of various adducts we analyse their competitive binding at the metal centre. We describe the impact of functionalization of the complexes near the metal centre and on the ligand backbone. Finally, we draw conclusions about catalyst behaviour and formulate perspectives on catalyst activation strategies, choice of solvent environment and possible deactivation species. The paper is organized as follows: in the computational methods section we describe the functionalization approach, computational model to investigate the thermodynamic parameters, and details of the quantum chemical calculations applied. Next we describe and discuss the results from our calculations. Finally we summarize the results and present our conclusions.

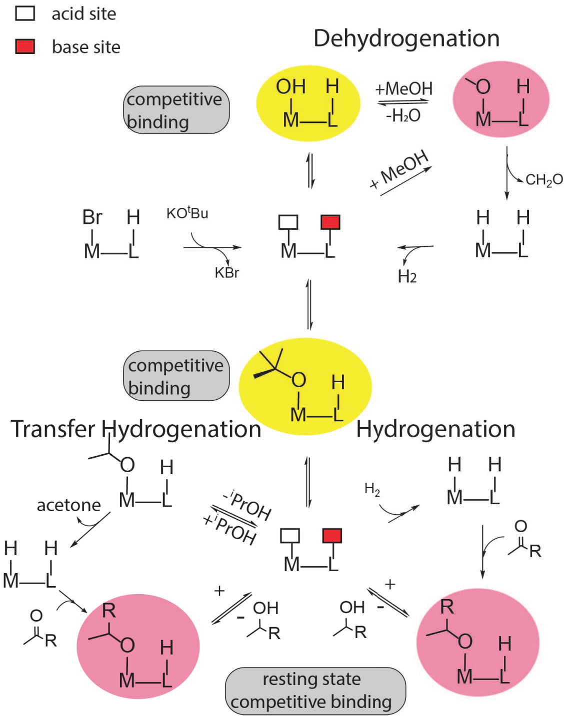

Figure 4.2: Representative catalytic cycles for dehydrogenation and hydrogenation reaction with possible competing and deactivation pathways. Dehydrogenation of methanol in aqueous phase and hydrogenation of acetone to iPrOH have been used as representative examples. Possible alkoxides and hydroxide based competing and resting states have been highlighted in yellow and red respectively.

4.2. Computational Details

Electronic structure calculations on the transition metal complexes were carried out either by using the extended density functional tight-binding (DFTB) or the density functional theory (DFT) methods. For a large number of calculations, a full DFT based approach is computationally expensive. Extended DFTB calculations via the xTB code from Grimme's group has recently emerged as a rapid tool with reasonable accuracy to predict geometry and thermochemistry of various chemical systems including TM complexes.[62] We therefore performed xTB calculations on all the complexes in our paper. On a selected number of TM complexes (432) based on CNC, PCP and PNN ligands, we also performed DFT calculations. xTB calculations on the same 432 complexes were compared with DFT based predictions to determine the accuracy of xTB.

4.2.1. Extended density functional tight-binding calculations

Extended DFTB calculations were performed using the xTB software suite (version 6.3.3).[63, 64] The GFN2-xTB method was applied for geometry optimization, using the verytight criteria. Hessian matrix calculations were performed for all optimized geometries to verify the absence of imaginary frequencies and that each geometry corresponds to a local minimum on its respective potential energy surface (PES). The GBSA solvation model parametrized for THF as implemented in xTB was used to account for solvent effects.

4.2.2. Density functional theory calculations

Density functional theory (DFT) calculations were performed using the Gaussian 16 C.01 suite of software.[65] All geometries were optimized using the BP86 functional with a def2-SVP basis set in the gas phase.[66] The combination of functional and basis set have shown reliable geometry predictions accompanied with low computational costs.[67, 68] Hessian calculations were performed to ensure that all optimized geometries were a minima on the PES (no imaginary mode). Zero-point energy and Gibbs free energy corrections to electronic energy were obtained from hessian calculations within the harmonic approximation under standard conditions (298.15K, 1bar). Single point (SP) energy calculations with the SMD[69] solvation (THF) model were carried out using the PBE0 hybrid functionals[70] with a triple zeta basis set (def2-TZVP) to further refine the electronic energies. SPs were also carried out using the BP86 functional.[71] We denote such composite methods BP86/def2-SVP//XC/def2-TZVP (THF), as BP86(THF) or PBE0(THF) depending on the exchange-correlation (XC) functional used for the SP single-point calculations. This allowed to investigate the impact of solvation (BP86(gas) vs BP86(THF)) and the functional (BP86(THF) vs PBE0(THF)) on the computed free energies. All DFT calculations were performed with dispersion correction (D3).[72] DFT calculations were performed for a selected number of complexes bearing CNC, PNN and PCP ligands. We focused our investigation on the addition of H-X species (X=H, OH, MeO, EtO, iPrO, tBuO, Br) across the catalyst which is represented as M–L, where M represents the metal centre and L represents the ligand. Addition of H–X across M–L leads to formation of M(X)-L(H) species, where metal forms an adduct with X and the ligand gets protonated. We estimated the thermodynamic stability of M(X)–L(H) by computing the Gibbs free energy change under standard conditions upon addition of H-X moiety across M-L bond (see equation below).

$$H - X + M - L \rightarrow M(X) - L(H)$$

$$\Delta G_{HX} = G(M(X) - L(H)) - G(M - L) - G(H - X)$$

4.3. Results and Discussion

4.3.1. Functionalization strategy

All functionalized geometries were obtained via an in-house developed automated python based workflow. We chose two different functionalization sites: four R_1 sites which are located near the metal centre, and two R_2 sites (only one in case of PCP) which functionalize the ligand backbone as shown in Figure 4.1. We chose to perform symmetric functionalizations meaning all four R_1 sites were kept the same, and both R_2 sites were also functionalized with the same ligand. R_1 and R_2 were however not constrained to be the same. In addition to functionalization sites on the

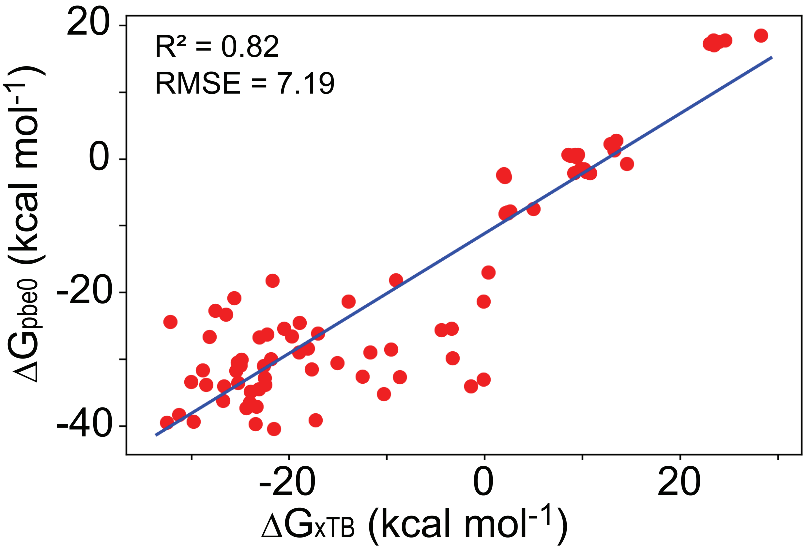

Figure 4.3: Correlation between Gibbs free energies (in kcal mol^{-1}) for addition of HBr computed using xTB (x-axis) and DFT (y-axis).

ligand, seven Mn-adducts were also considered which included vacant site (pristine complex), H, Br, MeO, iPrO, EtO and tBuO adducts. This functionalization scheme generated 1200 geometries of metal complexes. Out of these 1225 geometries, we filtered geometries where the pristine complex had a hemi-labile ligand resulting in a total of 732 geometries which are discussed in this work. We found that most PNN based complexes resulted in hemilabile ligand. Hemilability can arise as an artefact of xTB based geometry optimization or it can be genuinely present in the system. Since this would require further investigation we excluded all xTB based results for the PNN catalyst.

4.3.2. Comparison of xTB with DFT

Low computational cost and wide applicability of xTB calculations make them suitable for high throughput screening of TM complexes. The accuracy of xTB calculations has not been tested for Mn complexes. To investigate the accuracy of xTB calculations with respect to DFT based results, we computed CO stretching frequencies and ΔG_{HX} for selected complexes. Figure 4.3 compares xTB and DFT results for addition of HBr to Mn-PCP, Mn-PNN and Mn-CNC complexes. DFT and xTB computed ΔG_{HBr} agree well with R_2=0.82 and a RMSE (based on the linear fit) of 7.19 kcal mol^{-1}. The coefficient of correlation between xTB and DFT computed ΔG_{iPrOH} is relatively poor (R_2=0.28; RMSE=10.48kcal mol^{-1}) and the two methods reach only qualitative agreement for the addition of iPrOH.

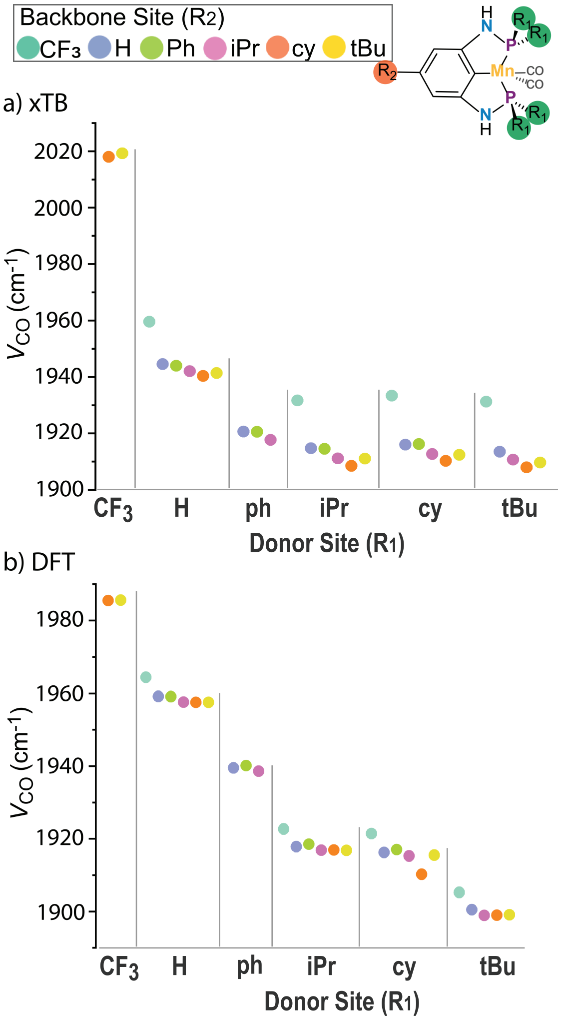

Figure 4.4: Vibrational frequencies in cm^{-1} per donor site and functional group.

To further compare the performance of xTB and DFT, we analysed the computed CO stretching frequencies, v(CO), for the carbonyl moieties in the Mn pincers. A comparison of the results obtained with the DFT and xTB methods for a representative case of Mn-PCP complex is presented in Figure 4.4. Both methodologies reveal a similar trend in computed v(CO). For a given R_1, electron donating R_2 groups give rise to lower v(CO). The plots also show that the electron donating effect of R_1 functionalization in this case is more important that that of the R_2, because of the major role of the electronic effects at the metal centre on the coordinated CO ligands. Furthermore, we observed a good agreement between xTB and DFT results when all systems with CF_3 functionalization are excluded from the dataset (R_2=0.85). xTB calculations seem to overestimate the CO stretching for CF_3 functionalized ligands for all pincer complexes considered in this study. Nevertheless, the comparison of ΔG_{HX} and v(CO) parameters point to a qualitative agreement between the results obtained with the xTB and DFT methods.

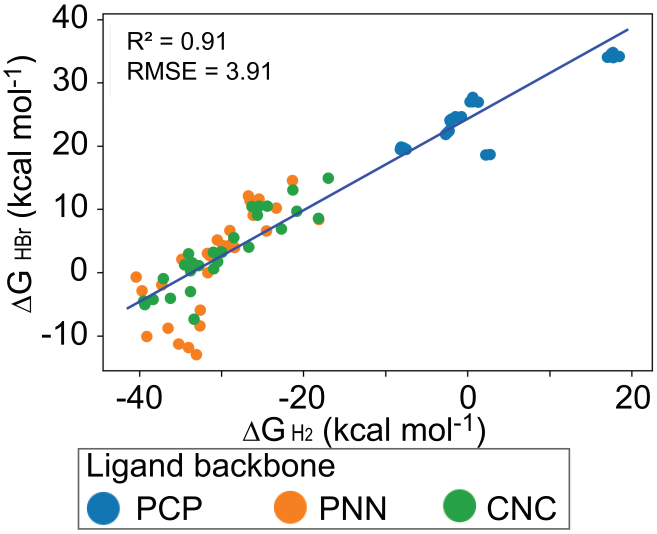

Figure 4.5: Comparison of DFT computed Gibbs free energy of formation (in kcal mol^{-1}) of bromide and hydride adducts in Mn-PCP, Mn-PNN and Mn-CNC complexes.

4.3.3. Scaling Relations and competitive adduct formation

The activation of H–X bonds is assumed to proceed via a metal-ligand cooperative heterolytic cleavage over the M–L site in all of the pincer complexes discussed here. We therefore, expect similar trends in Gibbs free energy for addition of H–X species, with differences arising from the nature of M-X bonding. Such similarities practically manifests themselves in scaling or linear free energy relationships between different substrates. Such relationships imply that having computed the ΔG_{HX_1} for a substrate HX_1, one can estimate the ΔG_{HX_i} for all other species that follow a linear scaling relation with HX_1. Figure 4.5 shows a significant correlation between the DFT-computed ΔG_{HBr} and ΔG_{H_2} using DFT (R_2=0.91), especially for PCP and CNC complexes. Therefore, the Gibbs free energy of the bromide adduct formation can be used to estimate the relative energy of formation of the hydride species. In our experience metal hydrides complexes are not described well using xTB.[73] Often the M-H bond was found to be very elongated (>2.8Å) in the structures obtained by the xTB-based geometry optimizations. However, Br complexes are described well and reasonable geometries were obtained with both xTB and DFT optimizations. Therefore, the scaling relationship that we observed between the bromide and hydride adduct becomes particularly practical because the ΔG_{HBr} computed using xTB can be directly used to estimate the stability of the active hydride intermediates in screening studies.

Figure 4.5 also shows that while both PCP and PNN complexes react with H_2 in an exergonic manner, the reaction is endergonic with Mn-CNC complexes. DFT calculations also revealed linear scaling relations among hydride, isopropoxide, bromide and hydroxide adducts. The correlation of ΔG_{H_2} with OH and iPrO adduct was found to be rather weak (R_2=0.53 and 0.55). We attribute this weaker correlation

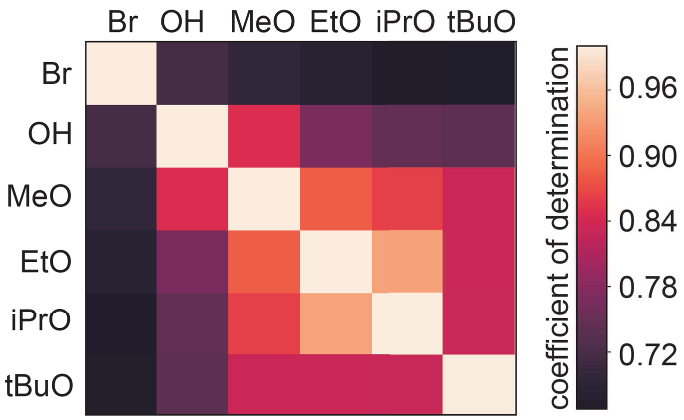

Figure 4.6: Correlation matrix of Gibbs free energy of formation in all ligand backbones investigated by xTB of the different metal adducts.

to differences in M–X bonds formed upon addition of H–X (M–OR vs. M–H) (vide infra). ΔG_{H_2O} and ΔG_{iPrOH} were found to have a moderate correlation with R_2=0.71. We also investigated the coefficient of determination between the xTB-computed ΔG_{HX} values. The resulting correlation matrix is shown in Figure 4.6. We observe that Gibbs free energies for addition of chemically similar species have higher coefficient of determination. For example, all alkoxides correlate well among each other but have relatively poor correlation with hydrides and bromides. Therefore, isopropoxide and ethoxide have the strongest correlation followed by the correlation between methoxide and ethoxide. The weakest correlation is between the Mn-alkoxides and the catalyst precursor (Mn-Br).

4.3.4. Adduct stability modulations via ligand modifications

Next we investigated the impact of the functionalization of donor site vs backbone on ΔG_{HX}. For this purpose we examined ΔG_{HBr} in two scenarios:

1) R_2=H with R_1 varied to investigate the impact of functionalization at the donor site
2) R_1= H with R_2 varied to investigate the impact of functionalization on the ligand backbone (Figure 4.4).

Functionalizations on the ligand either on donor or acceptor site can have a stabilizing or a destabilizing effect in two ways:

1) via (de)stabilization of the pristine catalyst
2) Electronic and/or steric (de)stabilization of the adduct moieties/.

The pristine complex can be (de)stabilized via geometric distortions and the resulting strain in the ligand scaffold introduced by functionalization. The adduct moiety such as an alkoxides can be destabilized by increased electronic density at the metal centre. On the other hand, the L-H bond in the adducts can be favourably stabilized by an increased electronic density at the ligand. Larger alkyl groups such as tBu/cy can also destabilize bulky alkoxides by steric repulsion. An accurate consideration of electronic effects is necessary to examine the impact of functionalization. Therefore we examined the impact of functionalization of ΔG_{HX} using DFT calculations.

4.3.5. Functionalization on donor site

R_2=H resulted in five PCP (R_1=H, Ph, iPr, cy, tBu), four CNC (R_1=CF3, Ph, iPr and cy) and three PNN (R_1=Ph, iPr and tBu) ligand complexes. For both PCP and PNN complexes, electron donating groups at R_1 destabilize the adduct leading to higher (more positive) ΔG_{HX}. In contrast to PCP and PNN complexes, the CNC complexes exhibit a different trend. The electron withdrawing CF_3 groups also destabilize Br and OH adducts. A detailed analysis of this divergent trend is beyond the scope of this paper. We speculate that these differences are related to the nature of Mn-C coordination in the CNC complexes. Furthermore, the R_1 functionalizations in this case are not performed on the C moiety coordinating the Mn centre unlike for the other complexes where the functionalized P/N/S are directly bound with the metal site.

4.3.6. Functionalization on ligand backbone

Primarily two factors control the impact of functionalization on the ligand backbone:

1) electronic effect which influences the basicity of the acceptor site and
2) strain in the geometry upon functionalization.

Electron releasing groups should increase the basicity of the acceptor site and, therefore, are expected to have a stabilizing effect. At the same, since electron releasing groups such as a tBu are bulkier they are also expected to introduce a high amount of strain in the coordinated ligand geometry. R_1=iPr resulted in 6 CPC and PNN, and 5 PCP complexes with Br coordinated to the Mn.

Variation of R_2 seems to have minimal impact on the PCP scaffold where ΔG_{HBr} shows little variation with the R_2=H being the most stable complex, and R_2=CF_3 being the least stable. This behaviour is expected since the R_2 site is located further away from the proton acceptor site on the ligand. For both Mn-PNN and Mn-CNC complexes, R_2=cy results in most favourable adduct formation. R_2=CF_3 leads to most destabilized adduct for the Mn-CNC, whereas R_2=tBu is most destabilizing functionalization for Mn-PNN. The additional stabilization of cy substitution is in contrast with the destabilization introduced by other electron donating groups namely Ph, iPr and tBu. The Hamett constants of cy and iPr are -0.05 and -0.04, respectively, indicating similar electron releasing behaviour via inductive effect.[74] We attribute the observed destabilizing effect of Ph, iPr and tBu groups, despite their electron donating nature, to the geometric strain. Analysis of geometric strain showed that R_2=cy scaffold had an effective stabilization of 4.15 kcal mol^{-1} relative to R_2=H. In contrast while R_2=iPr suffered a destabilization of 1.37 kcal mol^{-1}. Therefore both steric and inductive effects play an important role in stabilization of the Br adducts. Heatmap plots for the functionalization on donor and ligand backbone sites respectively represent the average impact of the choice of the functionalization groups. Both donor and backbone site functionalization leads to a great spread in average Gibbs free energy of formation, which can vary by up to

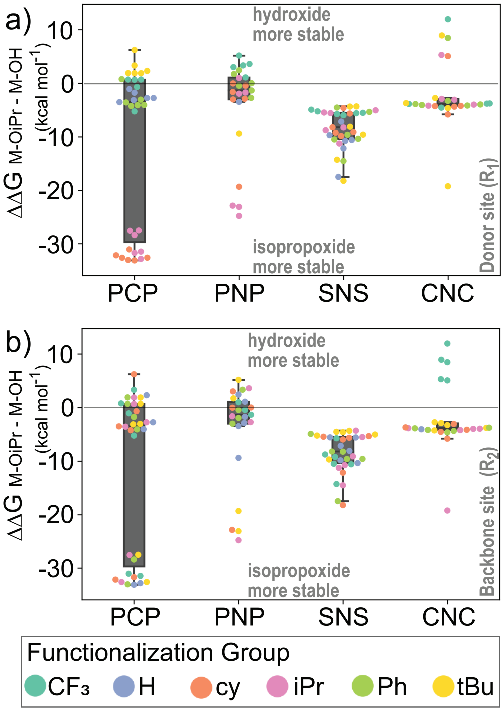

Figure 4.7: Comparison of isopropoxide stabilities with hydroxide per catalytic ligand group (in kcal mol^{-1}). Swarmplots are added to indicate the functionalization on a) catalyst donor site R_1 and b) catalyst backbone site R_2.

20 kcal mol^{-1} between different functionalizations. This reflects the degree of tunability of the catalytic properties that these ligand scaffolds can offer. Especially interesting are the qualitative changes in the average stability, where for example the substitution of CF_3 on the backbone site can turn the adduct formation from exergonic to endergonic. The relative range and standard deviation does not change significantly within the data sets.

4.3.7. Catalytic adduct species

With regards to the catalytic cycle, different adduct stabilities that play a significant role in activity and efficiency are examined. The heatmaps of the average formation Gibbs free energies shows the difference between the investigated adducts. The results indicate that the bromide adduct sustains substantial stability upon functionalization, especially for CNC complexes. The stabilities of the other adducts with similar structure such as MeO and EtO, or tBuO and iPrO are quite similar.

Boxplots comparing the difference formation Gibbs free energies for the catalysts with different ligands are shown in Figure 4.7 and 4.8 allow to analyse the trends in more detail. One interesting aspect in (de)hydrogenation chemistry is the choice of the base activator / promotor for the catalytic reaction. An enhanced stability of a complex formed with the base can result in inhibition and the catalyst can remain in a resting state. Here, we considered a model (de)hydrogenation of iPrOH reaction as an example.

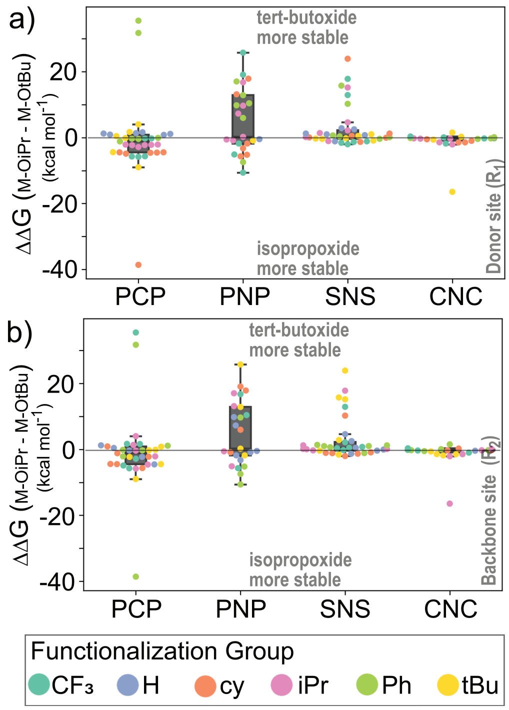

Figure 4.8: Comparison of isopropoxide stabilities with tert-butoxide per catalytic ligand group (in kcal mol^{-1}). Swarmplots are added to indicate the functionalization on a) catalyst donor site R$_1$ and b) catalyst backbone site R$_2$.

In Figure 4.7 and 4.8, the stability of isopropoxide to the adduct of two potential bases (KOH and KOtBu, respectively) is compared. The results show that a competition between the base (KOtBu) and iPrOH for complexation with the Mn centre is highly likely. However, the iPrO adduct was generally found to be more stable than the OH adduct for all Mn-pincers studied here. This concludes that KOH may represent a better choice for the systems where IPA dehydrogenation is important. Consistent with our observation, Beller and co-workers observed that switching from KOH to KOtBu lead to catalyst deactivation in dehydrogenation of methanol catalysed by a Mn-PNP pincer complex.[55]

4.4. Conclusions

In this investigation, we carried out a computational analysis of the effect of functionalization on different Mn-adducts of five types of pincer catalysts. Here, a data augmented approach was employed using fast xTB optimizations to analyse stabilities of metal adducts that can play a significant role in the catalytic cycle. The xTB results were compared to DFT calculations, which showed qualitative agreement and helped identifying the accuracy boundary of the accelerated xTB methodologies for studying Mn(I)-pincer complexes We identified linear scaling relation between Gibbs free energy for formation of different adducts, which can be used for rapid screening purposes.

Functionalization of the donor site directly affects the metal centre activation, as illustrated by the changes in the computed CO stretching frequencies. Increased electronic density at the metal centre and geometric strain both have destabilizing effects on the formation of alkoxides, hydroxide, bromides and hydride adducts. Comparison of relative stabilities of the isopropoxide adduct with hydroxide and tert-butoxide adducts showed that KOtBu can have a poisoning effect during iPrOH dehydrogenation, and that KOH would be a more suitable base.

In the outlook, this work is a first step in mechanism based high throughput screening of pincer ligand based catalysts. Development of data-augmented approaches to screen and design highly active homogeneous catalysts is an ongoing effort in our laboratory.

References

[1] A. M. Krieger, V. Sinha, A. V. Kalikadien, and E. A. Pidko, *Metal-ligand cooperative activation of HX (X=H, Br, OR) bond on Mn based pincer complexes,* Zeitschrift für Anorg. und Allg. Chemie **647**, 1486 (2021).

[2] S. Werkmeister, K. Junge, and M. Beller, *Catalytic Hydrogenation of Carboxylic Acid Esters, Amides, and Nitriles with Homogeneous Catalysts,* Org. Process Res. Dev. **18**, 289 (2014).

[3] L. Maser, L. Vondung, and R. Langer, *The ABC in pincer chemistry – From amine- to borylene- and carbon-based pincer-ligands,* Polyhedron **143**, 28 (2018).

[4] S. Werkmeister, J. Neumann, K. Junge, and M. Beller, *Pincer-Type Complexes for Catalytic (De)Hydrogenation and Transfer (De)Hydrogenation Reactions: Recent Progress,* Chem. - A Eur. J. **21**, 12226 (2015).

[5] P. A. Dub and J. C. Gordon, *The role of the metal-bound N–H functionality in Noyori-type molecular catalysts,* Nat. Rev. Chem. **2**, 396 (2018).

[6] W. Kuriyama, T. Matsumoto, O. Ogata, Y. Ino, K. Aoki, S. Tanaka, K. Ishida, T. Kobayashi, N. Sayo, and T. Saito, *Catalytic Hydrogenation of Esters. Development of an Efficient Catalyst and Processes for Synthesising (R)-1,2-Propanediol and 2-(l-Menthoxy)ethanol,* Org. Process Res. Dev. **16**, 166 (2012).

[7] T. Otsuka, A. Ishii, P. A. Dub, and T. Ikariya, *Practical Selective Hydrogenation of α-Fluorinated Esters with Bifunctional Pincer-Type Ruthenium(II) Catalysts Leading to Fluorinated Alcohols or Fluoral Hemiacetals,* J. Am. Chem. Soc. **135**, 9600 (2013).

[8] W. Aoki, N. Wattanavinin, S. Kusumoto, and K. Nozaki, *Development of Highly Active Ir–PNP Catalysts for Hydrogenation of Carbon Dioxide with Organic Bases,* Bull. Chem. Soc. Jpn. **89**, 113 (2016).

[9] M. Garbe, K. Junge, S. Walker, Z. Wei, H. Jiao, A. Spannenberg, S. Bachmann, M. Scalone, and M. Beller, *Manganese(I)-Catalyzed Enantioselective Hydrogenation of Ketones Using a Defined Chiral PNP Pincer Ligand,* Angew. Chemie Int. Ed. **56**, 11237 (2017).

[10] F. Kallmeier and R. Kempe, *Manganese Complexes for (De)Hydrogenation Catalysis: A Comparison to Cobalt and Iron Catalysts,* Angew. Chemie Int. Ed. **57**, 46 (2018).

[11] L. Alig, M. Fritz, and S. Schneider, *First-Row Transition Metal (De)Hydrogenation Catalysis Based On Functional Pincer Ligands,* Chem. Rev. **119**, 2681 (2019).

[12] G. A. Filonenko, R. van Putten, E. J. M. Hensen, and E. A. Pidko, *Catalytic (de)hydrogenation promoted by non-precious metals – Co, Fe and Mn: recent advances in an emerging field,* Chem. Soc. Rev. **47**, 1459 (2018).

[13] F. Agbossou-Niedercorn and C. Michon, *Bifunctional homogeneous catalysts based on first row transition metals in asymmetric hydrogenation,* Coord. Chem. Rev. **425**, 213523 (2020).

[14] S. Schneider, J. Meiners, and B. Askevold, *Cooperative Aliphatic PNP Amido Pincer Ligands – Versatile Building Blocks for Coordination Chemistry and Catalysis,* Eur. J. Inorg. Chem. **2012**, 412 (2012).

[15] K. J. Evans and S. M. Mansell, *Functionalised N-Heterocyclic Carbene Ligands in Bimetallic Architectures,* Chem. – A Eur. J. **26**, 5927 (2020).

[16] A. J. Canty, A. Ariafard, and G. Koten, *Computational Analysis of Mesomerism in para-Substituted mer-NCN Pincer Platinum(II) Complexes, Including its Relationships with Hammett σ p Substituent Parameters,* Chem. – A Eur. J. **26**, 15629 (2020).

[17] G. D. Batema, M. Lutz, A. L. Spek, C. A. van Walree, G. P. M. van Klink, and G. van Koten, *Organometallic benzylidene anilines: donor–acceptor features in NCN-pincer Pt(II) complexes with a 4-(E)-[(4-R-phenyl)imino]methyl substituent,* Dalt. Trans. **43**, 12200 (2014).

[18] P. Friederich, G. dos Passos Gomes, R. De Bin, A. Aspuru-Guzik, and D. Balcells, *Machine learning dihydrogen activation in the chemical space surrounding Vaska's complex,* Chem. Sci. **11**, 4584 (2020).

[19] J. P. Janet, F. Liu, A. Nandy, C. Duan, T. Yang, S. Lin, and H. J. Kulik, *Designing in the Face of Uncertainty: Exploiting Electronic Structure and Machine Learning Models for Discovery in Inorganic Chemistry,* Inorg. Chem. **58**, 10592 (2019).

[20] M. D. Wodrich, B. Sawatlon, E. Solel, S. Kozuch, and C. Corminboeuf, *Activity-Based Screening of Homogeneous Catalysts through the Rapid Assessment of Theoretically Derived Turnover Frequencies,* ACS Catal. **9**, 5716 (2019).

[21] B. Sawatlon, M. D. Wodrich, and C. Corminboeuf, *Unraveling Metal/Pincer Ligand Effects in the Catalytic Hydrogenation of Carbon Dioxide to Formate,* Organometallics **37**, 4568 (2018).

[22] M. D. Wodrich, M. Busch, and C. Corminboeuf, *Expedited Screening of Active and Regioselective Catalysts for the Hydroformylation Reaction,* Helv. Chim. Acta **101**, e1800107 (2018).

[23] M. Glatz, B. Stöger, D. Himmelbauer, L. F. Veiros, and K. Kirchner, *Chemoselective Hydrogenation of Aldehydes under Mild, Base-Free Conditions: Manganese Outperforms Rhenium,* ACS Catal. **8**, 4009 (2018).

[24] F. Bertini, M. Glatz, B. Stöger, M. Peruzzini, L. F. Veiros, K. Kirchner, and L. Gonsalvi, *Carbon Dioxide Reduction to Methanol Catalyzed by Mn(I) PNP Pincer Complexes under Mild Reaction Conditions,* ACS Catal. **9**, 632 (2019).

[25] S. Kostera, M. Peruzzini, K. Kirchner, and L. Gonsalvi, *Mild and Selective Carbon Dioxide Hydroboration to Methoxyboranes Catalyzed by Mn(I) PNP Pincer Complexes,* ChemCatChem **12**, 4625 (2020).

[26] L. Zhang, Z. Wang, Z. Han, and K. Ding, *Manganese-Catalyzed anti-Selective Asymmetric Hydrogenation of* α*-Substituted* β*-Ketoamides,* Angew. Chemie Int. Ed. **59**, 15565 (2020).

[27] F. Ling, J. Chen, S. Nian, H. Hou, X. Yi, F. Wu, M. Xu, and W. Zhong, *Manganese-Catalyzed Enantioselective Hydrogenation of Simple Ketones Using an Imidazole-Based Chiral PNN Tridentate Ligand,* Synlett **31**, 285 (2020).

[28] A. Kumar, P. Daw, N. A. Espinosa-Jalapa, G. Leitus, L. J. W. Shimon, Y. Ben-David, and D. Milstein, *CO2 activation by manganese pincer complexes through different modes of metal–ligand cooperation,* Dalt. Trans. **48**, 14580 (2019).

[29] L. Zhang, Y. Tang, Z. Han, and K. Ding, *Lutidine-Based Chiral Pincer Manganese Catalysts for Enantioselective Hydrogenation of Ketones,* Angew. Chemie Int. Ed. **58**, 4973 (2019).

[30] G. A. Filonenko, E. J. M. Hensen, and E. A. Pidko, *Mechanism of CO2 hydrogenation to formates by homogeneous Ru-PNP pincer catalyst: from a theoretical description to performance optimization,* Catal. Sci. Technol. **4**, 3474 (2014).

[31] F. Schneck, M. Finger, M. Tromp, and S. Schneider, *Chemical Non-Innocence of an Aliphatic PNP Pincer Ligand,* Chem. - A Eur. J. **23**, 33 (2017).

[32] J. Zhang, E. Balaraman, G. Leitus, and D. Milstein, *Electron-Rich PNP- and PNN-Type Ruthenium(II) Hydrido Borohydride Pincer Complexes. Synthesis, Structure, and Catalytic Dehydrogenation of Alcohols and Hydrogenation of Esters,* Organometallics **30**, 5716 (2011).

[33] N. Biswas, R. Sharma, and D. Srimani, *Ruthenium Pincer Complex Catalyzed Selective Synthesis of C-3 Alkylated Indoles and Bisindolylmethanes Directly from Indoles and Alcohols,* Adv. Synth. Catal. **362**, 2902 (2020).

[34] J. Schörgenhumer, A. Zimmermann, and M. Waser, *SNS-Ligands for Ru-Catalyzed Homogeneous Hydrogenation and Dehydrogenation Reactions,* Org. Process Res. Dev. **22**, 862 (2018).

[35] X. Chen, Y. Jing, and X. Yang, *Unexpected Direct Hydride Transfer Mechanism for the Hydrogenation of Ethyl Acetate to Ethanol Catalyzed by SNS Pincer Ruthenium Complexes,* Chem. - A Eur. J. **22**, 1950 (2016).

[36] D. Spasyuk, S. Smith, and D. G. Gusev, *Replacing Phosphorus with Sulfur for the Efficient Hydrogenation of Esters,* Angew. Chemie Int. Ed. **52**, 2538 (2013).

[37] T.-a. Koizumi, T. Teratani, K. Okamoto, T. Yamamoto, Y. Shimoi, and T. Kanbara, *Nickel(II) complexes bearing a pincer ligand containing thioamide units: Comparison between SNS- and SCS-pincer ligands,* Inorganica Chim. Acta **363**, 2474 (2010).

[38] U. K. Das, S. L. Daifuku, T. E. Iannuzzi, S. I. Gorelsky, I. Korobkov, B. Gabidullin, M. L. Neidig, and R. T. Baker, *Iron(II) Complexes of a Hemilabile SNS Amido Ligand: Synthesis, Characterization, and Reactivity,* Inorg. Chem. **56**, 13766 (2017).

[39] X. Wu, L. Ji, Y. Ji, E. H. Elageed, and G. Gao, *Hydrogenation of ethylene carbonate catalyzed by lutidine-bridged N-heterocyclic carbene ligands and ruthenium precursors,* Catal. Commun. **85**, 57 (2016).

[40] M. Hernández-Juárez, J. López-Serrano, P. Lara, J. P. Morales-Cerón, M. Vaquero, E. Álvarez, V. Salazar, and A. Suárez, *Ruthenium(II) Complexes Containing Lutidine-Derived Pincer CNC Ligands: Synthesis, Structure, and Catalytic Hydrogenation of C-N bonds,* Chem. - A Eur. J. **21**, 7540 (2015).

[41] G. A. Filonenko, E. Cosimi, L. Lefort, M. P. Conley, C. Copéret, M. Lutz, E. J. M. Hensen, and E. A. Pidko, *Lutidine-Derived Ru-CNC Hydrogenation Pincer Catalysts with Versatile Coordination Properties,* ACS Catal. **4**, 2667 (2014).

[42] A. R. Naziruddin, C.-L. Kuo, W.-J. Lin, W.-H. Lo, C.-S. Lee, B.-J. Sun, A. H. H. Chang, and W.-S. Hwang, *Ruthenium Complexes Bearing Unsymmetric CNC′ Pincer Ligands: Molecular Structures and Electronic Properties,* Organometallics **33**, 2575 (2014).

[43] S. Gründemann, M. Albrecht, J. A. Loch, J. W. Faller, and R. H. Crabtree, *Tridentate Carbene CCC and CNC Pincer Palladium(II) Complexes: Structure, Fluxionality, and Catalytic Activity,* Organometallics **20**, 5485 (2001).

[44] A. A. Danopoulos, N. Tsoureas, J. A. Wright, and M. E. Light, *N-Heterocyclic Pincer Dicarbene Complexes of Iron(II): C-2 and C-5 Metalated Carbenes on the Same Metal Center,* Organometallics **23**, 166 (2004).

[45] P. Edwards and R. Jaouhari, *Synthesis and characterization of complexes of nickel(II), palladium(II) and platinum(II) with the new bifunctional aminodiphosphine ligand HN(CH2CH2CH2PMe2)2,* Polyhedron **8**, 25 (1989).

[46] M. Gagliardo, P. A. Chase, S. Brouwer, G. P. M. van Klink, and G. van Koten, *Electronic Effects in PCP-Pincer Ru(II)-Based Hydrogen Transfer Catalysis,* Organometallics **26**, 2219 (2007).

[47] B. C. Gruver, J. J. Adams, S. J. Warner, N. Arulsamy, and D. M. Roddick, *Acceptor Pincer Chemistry of Ruthenium: Catalytic Alkane Dehydrogenation by (CF3 PCP)Ru(cod)(H),* Organometallics **30**, 5133 (2011).

[48] S. Tang, N. von Wolff, Y. Diskin-Posner, G. Leitus, Y. Ben-David, and D. Milstein, *Pyridine-Based PCP-Ruthenium Complexes: Unusual Structures and Metal–Ligand Cooperation,* J. Am. Chem. Soc. **141**, 7554 (2019).

[49] J. J. Adams, N. Arulsamy, and D. M. Roddick, *Acceptor PCP Pincer Iridium(I) Chemistry: Stabilization of Nonmeridional PCP Coordination Geometries,* Organometallics **30**, 697 (2011).

[50] S. Murugesan and K. Kirchner, *Non-precious metal complexes with an anionic PCP pincer architecture,* Dalt. Trans. **45**, 416 (2016).

[51] D. Spasyuk, S. Smith, and D. G. Gusev, *Replacing Phosphorus with Sulfur for the Efficient Hydrogenation of Esters,* Angew. Chemie **125**, 2598 (2013).

[52] K. Larmier, W.-C. Liao, S. Tada, E. Lam, R. Verel, A. Bansode, A. Urakawa, A. Comas-Vives, and C. Copéret, *CO2-to-Methanol Hydrogenation on Zirconia-Supported Copper Nanoparticles: Reaction Intermediates and the Role of the Metal-Support Interface,* Angew. Chemie Int. Ed. **56**, 2318 (2017).

[53] W.-H. Wang, Y. Himeda, J. T. Muckerman, G. F. Manbeck, and E. Fujita, *CO2 Hydrogenation to Formate and Methanol as an Alternative to Photo- and Electrochemical CO2 Reduction,* Chem. Rev. **115**, 12936 (2015).

[54] H. Yang, C. Zhang, P. Gao, H. Wang, X. Li, L. Zhong, W. Wei, and Y. Sun, *A review of the catalytic hydrogenation of carbon dioxide into value-added hydrocarbons,* Catal. Sci. Technol. **7**, 4580 (2017).

[55] M. Andérez-Fernández, L. K. Vogt, S. Fischer, W. Zhou, H. Jiao, M. Garbe, S. Elangovan, K. Junge, H. Junge, R. Ludwig, and M. Beller, *A Stable Manganese Pincer Catalyst for the Selective Dehydrogenation of Methanol,* Angew. Chemie Int. Ed. **56**, 559 (2017).

[56] C. J. A. Daley and S. H. Bergens, *The First Complete Identification of a Diastereomeric Catalyst−Substrate (Alkoxide) Species in an Enantioselective Ketone Hydrogenation. Mechanistic Investigations,* J. Am. Chem. Soc. **124**, 3680 (2002).

[57] R. J. Hamilton and S. H. Bergens, *An Unexpected Possible Role of Base in Asymmetric Catalytic Hydrogenations of Ketones. Synthesis and Characterization of Several Key Catalytic Intermediates,* J. Am. Chem. Soc. **128**, 13700 (2006).

[58] R. J. Hamilton and S. H. Bergens, *Direct Observations of the Metal−Ligand Bifunctional Addition Step in an Enantioselective Ketone Hydrogenation,* J. Am. Chem. Soc. **130**, 11979 (2008).

[59] M. Zimmer-De Iuliis and R. H. Morris, *Kinetic Hydrogen/Deuterium Effects in the Direct Hydrogenation of Ketones Catalyzed by a Well-Defined Ruthenium Diphosphine Diamine Complex,* J. Am. Chem. Soc. **131**, 11263 (2009).

[60] A. Passera and A. Mezzetti, *Mn(I) and Fe(II)/PN(H)P Catalysts for the Hydrogenation of Ketones: A Comparison by Experiment and Calculation,* Adv. Synth. Catal. **361**, 4691 (2019).

[61] J. Pham, C. E. Jarczyk, E. F. Reynolds, S. E. Kelly, T. Kim, T. He, J. M. Keith, and A. R. Chianese, *The key role of the latent N–H group in Milstein's catalyst for ester hydrogenation,* Chem. Sci. **12**, 8477 (2021).

[62] C. Bannwarth, E. Caldeweyher, S. Ehlert, A. Hansen, P. Pracht, J. Seibert, S. Spicher, and S. Grimme, *Extended tight-bindingquantum chemistry methods,* WIREs Comput. Mol. Sci. **11** (2021), 10.1002/wcms.1493.

[63] C. Bannwarth, S. Ehlert, and S. Grimme, *GFN2-xTB-An Accurate and Broadly Parametrized Self-Consistent Tight-Binding Quantum Chemical Method with Multipole Electrostatics and Density-Dependent Dispersion Contributions,* J. Chem. Theory Comput. **15**, 1652 (2019).

[64] S. Grimme, C. Bannwarth, and P. Shushkov, *A Robust and Accurate Tight-Binding Quantum Chemical Method for Structures, Vibrational Frequencies, and Noncovalent Interactions of Large Molecular Systems Parametrized for All spd-Block Elements (Z = 1–86),* J. Chem. Theory Comput. **13**, 1989 (2017).

[65] M. J. Frisch, G. W. Trucks, H. B. Schlegel, G. E. Scuseria, M. A. Robb, J. R. Cheeseman, G. Scalmani, V. Barone, G. A. Petersson, H. Nakatsuji, X. Li, M. Caricato, A. V. Marenich, J. Bloino, B. G. Janesko, R. Gomperts, B. Mennucci, H. P. Hratchian, J. V. Ortiz, A. F. Izmaylov, J. L. Sonnenberg, D. Williams-Young, F. Ding, F. Lipparini, F. Egidi, J. Goings, B. Peng, A. Petrone, T. Henderson, D. Ranasinghe, V. G. Zakrzewski, J. Gao, N. Rega, G. Zheng, W. Liang, M. Hada, M. Ehara, K. Toyota, R. Fukuda, J. Hasegawa, M. Ishida, T. Nakajima, Y. Honda, O. Kitao, H. Nakai, T. Vreven, K. Throssell, J. A. Montgomery Jr., J. E. Peralta, F. Ogliaro, M. J. Bearpark, J. J. Heyd, E. N.

Brothers, K. N. Kudin, V. N. Staroverov, T. A. Keith, R. Kobayashi, J. Normand, K. Raghavachari, A. P. Rendell, J. C. Burant, S. S. Iyengar, J. Tomasi, M. Cossi, J. M. Millam, M. Klene, C. Adamo, R. Cammi, J. W. Ochterski, R. L. Martin, K. Morokuma, O. Farkas, J. B. Foresman, and D. J. Fox, *Gaussian16 Revision C.01,* (2016).

[66] F. Weigend and R. Ahlrichs, *Balanced basis sets of split valence, triple zeta valence and quadruple zeta valence quality for H to Rn: Design and assessment of accuracy,* Phys. Chem. Chem. Phys. **7**, 3297 (2005).

[67] M. Bühl and H. Kabrede, *Geometries of Transition-Metal Complexes from Density-Functional Theory,* J. Chem. Theory Comput. **2**, 1282 (2006).

[68] K. P. Jensen, B. O. Roos, and U. Ryde, *Performance of density functionals for first row transition metal systems,* J. Chem. Phys. **126**, 014103 (2007).

[69] A. V. Marenich, C. J. Cramer, and D. G. Truhlar, *Universal Solvation Model Based on Solute Electron Density and on a Continuum Model of the Solvent Defined by the Bulk Dielectric Constant and Atomic Surface Tensions,* J. Phys. Chem. B **113**, 6378 (2009).

[70] C. Adamo and V. Barone, *Toward reliable density functional methods without adjustable parameters: The PBE0 model,* J. Chem. Phys. **110**, 6158 (1999).

[71] A. D. Becke, *Density-functional exchange-energy approximation with correct asymptotic behavior,* Phys. Rev. A **38**, 3098 (1988).

[72] E. Caldeweyher, C. Bannwarth, and S. Grimme, *Extension of the D3 dispersion coefficient model,* J. Chem. Phys. **147**, 034112 (2017).

[73] V. Sinha, J. J. Laan, and E. A. Pidko, *Accurate and rapid prediction of pK_a of transition metal complexes: semiempirical quantum chemistry with a data-augmented approach,* Phys. Chem. Chem. Phys. **23**, 2557 (2021).

[74] C. Hansch, A. Leo, and R. W. Taft, *A survey of Hammett substituent constants and resonance and field parameters,* Chem. Rev. **91**, 165 (1991).

5

The Impact of Computational Uncertainties

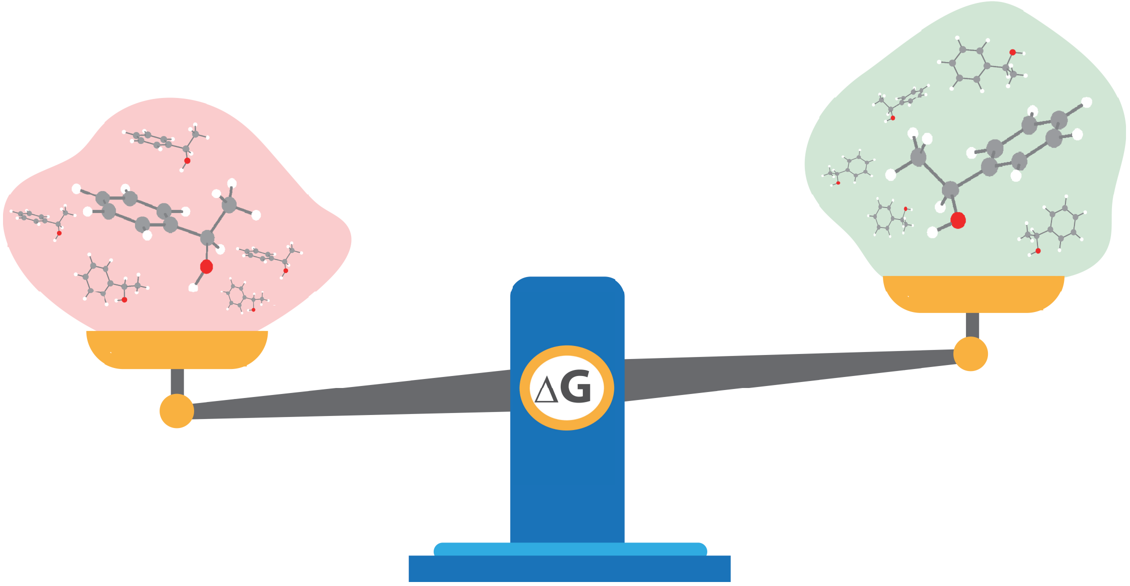

This chapter has been published in ChemCatChem **13** (2021) [1].

Selectivity control is one of the most important functions of a catalyst. In asymmetric catalysis the enantiomeric excess (e.e.) is a property of major interest, with a lot of effort dedicated to developing the most enantioselective catalyst, understanding the origin of selectivity and predicting stereo selectivity. Herein, we investigate the relationship between predicted selectivity and the uncertainties in the computed energetics of the catalytic reaction mechanism obtained by DFT calculations in a case study of catalytic asymmetric transfer hydrogenation (ATH) of ketones with an Mn-diamine catalyst. Data obtained from our analysis of DFT data by microkinetic modelling is compared to results from experiment. We discuss the limitations of the conventional reductionist approach of e.e. estimation from assessing the enantiodeterminative steps only. Our analysis shows that the energetics of other reaction steps in the reaction mechanism have a substantial impact on the predicted reaction selectivity. The uncertainty of DFT calculations within the commonly accepted energy ranges of chemical accuracy may reverse the predicted e.e. with the non-enenatiodeterminitive steps contributing to e.e. deviations of up to 25%.

5.1. Introduction

Asymmetric reduction catalysis is a powerful tool for the production of chiral compounds. Enantiomeric purity is desirable in the production of fine chemicals such as in the pharmaceutical and crop-protection industry.[2] Discovery of efficient enantioselective catalysts involves tedious works largely based on the trial and error approach. There is a long-standing dream of rational design based on ab initio calculations.[3] Substantial progress has been made in this direction in the recent years with the introduction of novel data-rich computational screening approaches allowing for rapid evaluation of diverse reactivity descriptors for transition metal catalysts and correlating them with defined reactivity metrics.[4–6] Despite great progress witnessed in the last decade[7, 8], computational elucidation of enantioselectivity still mostly follows synthesis instead of leading it, possibly introducing a bias towards the experimental outcome.[9–13] Density functional theory (DFT) is currently the method of choice for computing mechanisms and energetics of competing reaction paths in homogeneous catalysis by transition metals.[14–16] Although the accuracy of modern computational methods is being constantly improved through the efforts of a large community of researchers, reaching the chemical accuracy of 5 kJ mol^{-1} is still a great challenge for practical electronic structure methods.[17–19]

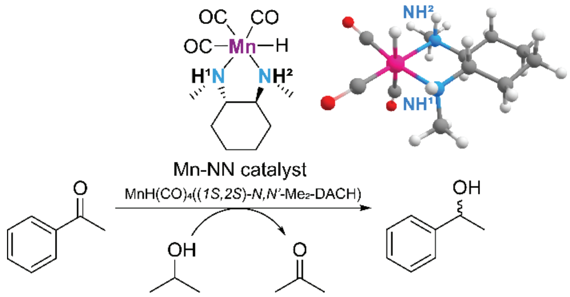

Figure 5.1: Mn-diamine catalyst with reaction site NH$_1$ and NH$_2$ and the model reaction of acetophenone to phenylethanol.

Besides the accuracy of the computational method, the uncertainty regarding the reaction mechanism and the nature of the catalytic species can also affect the predictive power. Multi-step mechanisms with relatively short-lived intermediates are common in homogenous catalysis resulting in highly complex kinetic behaviour. The enantioselectivity is determined by the relative rates of the two competing enantioselective paths. Given the high complexity of most catalytic mechanisms, in practice e.e. are commonly estimated by comparing only the computed barriers of the two enantiodetermining steps, while assuming that the other reaction steps in the reaction mechanism have only minor impact on the overall kinetics and the e.e. of the reaction.

One way to tackle the mechanistic complexity of catalysis are ab initio kinetic models. Microkinetic models offer the possibility to investigate complete reaction pathways by calculating rate constants and modelling concentration profiles.[20] More complex reaction processes can hence be considered and enantioselective excess can be determined while accounting for the whole reaction network. In this paper we investigate how minor variations in the energetics of the reaction pathway affect the selectivity of the catalyst using Mn(I)-catalysed transfer hydrogenation of acetophenone as a model reaction (Figure 5.1). Selective reduction of organic oxygenates and their derivatives such as ketones, carboxylic acid esters and nitriles is fundamental to the production of fragrances, pharmaceuticals and fine-chemicals.[21, 22] In this context, asymmetric catalysis has led to exceptional advances in chemical synthesis.[23, 24] Besides, catalyst use is one of the most cost-effective and environmentally responsible method to circumvent the need for stoichiometric reductants.[25, 26]

In recent years, significant progress has been made in the enantioselective (transfer) hydrogenation of polar C=O and C=N functionalities.[27–33] All these advances are aimed to achieve the highest possible yield and enantioselectivity under mild conditions. The asymmetric transfer hydrogenation of ketones by transition metal catalysts has been studied and the catalytic mechanism has been addressed by numerous computational and experimental works.[30, 34, 35] In the last decade substantial efforts were put in the development of new catalysts based on earth-abundant elements. Several efficient enantioselective Mn(I)-based reduction catalysts have been reported.[9, 10, 36] Transfer hydrogenation by acid-base cooperative catalysts has been investigated both computationally and experimentally.[37–46] Evidence has been presented for both an inner- and outer-sphere pathway have been provided.[47, 48]

Mn(I)-based enantioselective catalysts are rare and usually underperform compared to the efficiency of their Ru or Rh-based counterparts. Computational screening is an attractive approach to accelerate the development of such biocompatible and cheaper Mn-based enantioselective catalysts. Herein, we employ a DFT-based microkinetic modelling to explore how accurate e.e. predictions can be assuming the chemical accuracy of DFT calculations and taking a kinetic model of the complete catalytic cycle into account for a simple chiral Mn–diamine catalysts. We apply a multidimensional analysis to identify the factors contributing towards selectivity aside from the energy difference between the enantiodetermining steps.

5.2. The Enantiomeric Excess

Enantiomeric excess is defined as the excess of the major enantiomer over the other:[49, 50]

$$e.e. = \frac{|c^R - c^S|}{c^R + c^S}$$

The ratio of the *R*- to *S*-enantiomer is directly linked to the ratio of the rate constants for the two competing reaction channels for the conversion of the prochiral substance to the particular enantiomers, which is in turn is linked to the difference in apparent Gibbs free energies of activation of the two competing reaction paths of the diastereomeric transition state. Conventionally the intrinsic free energy of the enantiodetermining step is employed to reduce the kinetic complexity. Instead of the ratios of the overall rates, difference of activation free energies of the rate-determining steps are considered:

$$\frac{c_R}{c_S} = \frac{k_{c_R}}{k_{c_S}} = e^{-\frac{\Delta\Delta G^{\ddagger}}{RT}}$$

Combing the two equations enables us to determine the e.e. from the difference in the transition state energy of the two enantiomers in the stereo selective step.

$$e.e. = \frac{|e^{-\frac{\Delta\Delta G^{\ddagger}}{RT}} - 1|}{e^{-\frac{\Delta\Delta G^{\ddagger}}{RT}} + 1}$$

Therefore, the apparent barrier that is observed in experimental and theoretical investigation directly determines the value of our mathematical determined e.e. as shown in Figure 5.2.

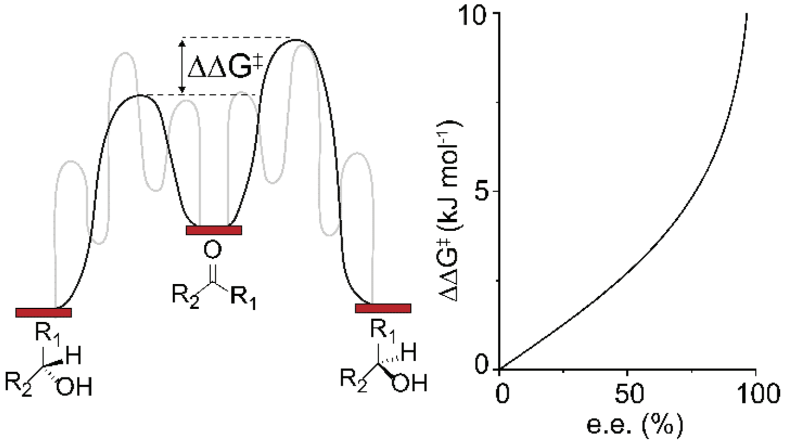

Figure 5.2: Relationship of the difference in the enantiodetermining transition state barrier and the enantiomeric excess assumed for the catalytic reaction.

5.3. Results and Discussion

In this work we considered the asymmetric Mn-diamine catalyst for the reduction of ketones. The hydrogenation of acetophenone to *R*- and *S*-phenylethanol was investigated as a model reaction. Figure 5.2 presents the postulated reaction mechanism along with the DFT-computed free energy diagram. The reaction can go along two channels distinguished as NH_1 and NH_2 here. Previous studies identified Mn(I)-alkoxide species as the key reaction intermediates. The catalytic cycle starts with a Mn-isopropoxide complex **1** that undergoes the β-H elimination to produce **2** that the Mn-hydrido complex with a weakly bound acetone molecule. Acetone is in the next step replaced by acetophenone substrate, which aligns its carbonyl group with the Mn-H and N-H moieties of the catalyst (**3**). The hydride from the metal centre is transferred to the ketone to form a stable alkoxide species **4**. This reaction step is also the enantiodetermining step, which dictates the chirality of the produced alcohol. In the most endergonic reaction step, 1-phenylethanol ($PhCH(OH)CH_3$) is liberated, leading to the formation of the dehydrogenated Mn-amido species **5**. In the final step of the catalytic cycle, isopropanol reacts with the dehydrogenated catalyst to regenerate the initial Mn(I)-isopropoxide state **1**.

The enantiodetermining step in the lowest energy reaction pathways of the formation of *R*- to *S*-phenylethanol shows a difference in Gibbs free energy of 6 kJ mol^{-1}. This difference translates with the equation 3 to an e.e. of 79%. The MKM model including all the reaction steps of the catalytic mechanism with the kinetic parameters directly computed from DFT predicts a similar e.e. of 77%, which (coincidentally) is in a perfect agreement with the experimental values in the range 72 - 75%. Next, we evaluated the sensitivity of the MKM-predicted e.e. to the variations in the computed energetics of the individual steps in the reaction mechanism. Figure 5.4 shows how the predicted e.e. change upon variations of the computed free energy barriers for different elementary steps with increments in the range from -5 to +5 kJ mol^{-1}. A maximum of two transition states were varied at the same instance in this analysis that are shown on the x- and y- axis of the diagram. The diagonal of Figure 5.4 therefore shows variations for the heights of the barriers of the individual elementary steps.

The most noticeable changes of the enantiomeric excess upon variation of one transition state barrier is observed for the enantiodetermining step (TS **3-4**). An increase or decrease of this barrier by only 2 kJ mol^{-1} leads to an e.e. of 61% to 87% (Figure 5.4). When the variation in the barrier height increased to 5 kJ mol^{-1} (i.e. “the chemical accuracy”) the resulting e.e. range covers 20% to 94% as expected from Figure 5.2. The variations in the barrier heights for the other steps in the catalytic mechanisms also affect the predicted e.e. but a lesser extent. Alterations in the two transition states that are neither stereospecific nor rate-determining (TS **1-2** and TS **6-1**) have little to no effect on the predicted enantioselectivity. On the other hand, the variations in the rate-determining step (TS **4-5**) affect notably the predicted e.e. If the production of *R*-phenylethanol (TS **4-5** *R*): -5 kJ mol^{-1}) is made more favourable the e.e. increases (<87%), and a significant lower e.e. is achieved when the formation of the S-enantiomer (TS **4-5** *S*: -5 kJ mol^{-1}) is enhanced (<67%).

The simultaneous change of two barriers gives rise to even more significant variations in the predicted enantioselectivity. Again the two reaction steps involved in the formation of the isopropoxide resting state (TS **6-1**) and Mn-hydride catalytic species (TS **1-2**), do not affect the enantioselectivity.

Especially interesting are comparisons of simultaneous variations of barriers in the *R*- and *S*-pathway or simultaneous variations in the enantiodetermining and rate-determining step. This is illustrated in more detail in Figure 5.6, where we visualize the enantiomeric excess achieved upon variation of two transition states. Considering the enantiodetermining step (TS **3-4**) a large range in the values of enantiomeric excess is observed (Figure 5.6a). The highest e.e. value (>98%) is

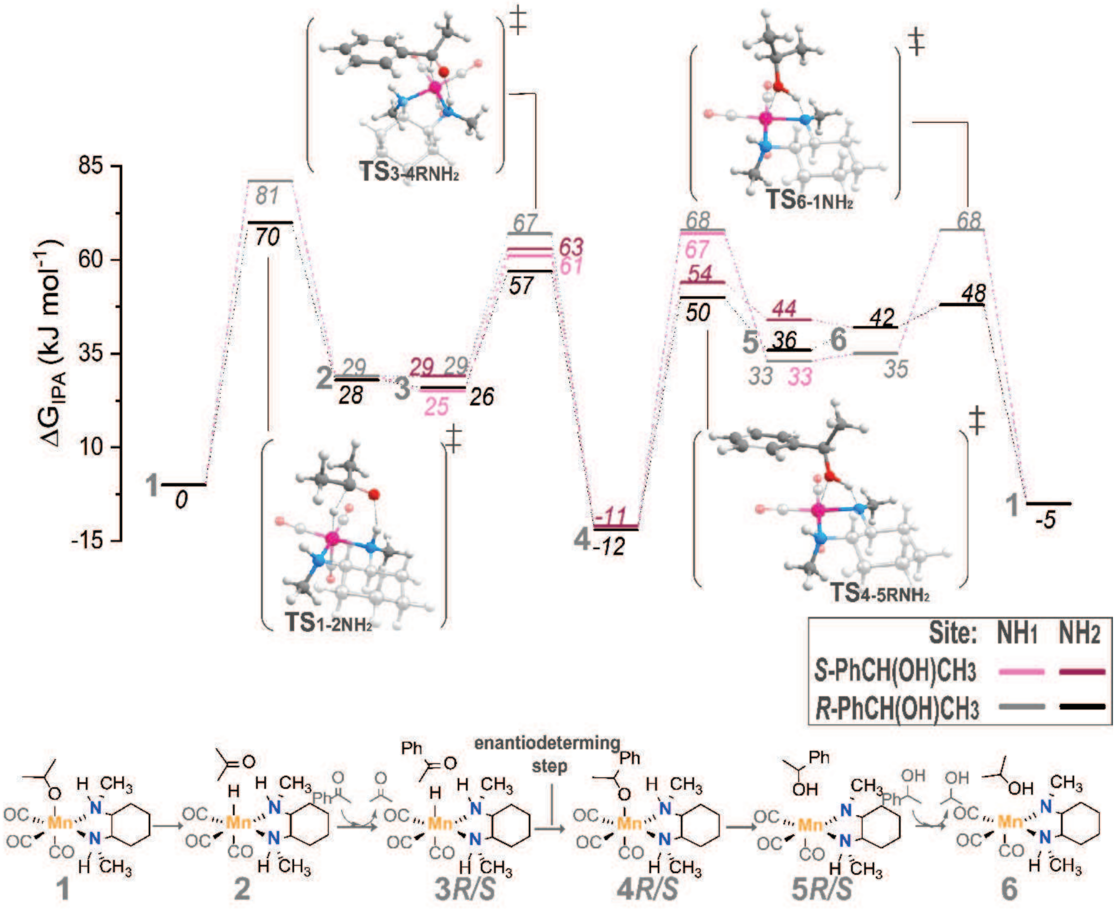

Figure 5.3: Standard Gibbs free energy diagram and the mechanism for the asymmetric transfer hydrogenation of acetophenone with isopropanol to *R*- and *S*-phenylethanol at both NH-reaction sites of Mn-N,N catalyst. Energies are given in kJ mol^{-1}.

observed when the barrier for the formation of *R*-phenylethanol is decreased while the barrier for S-phenylethanol is increased (TS **3-4** *R*: -5 kJ mol^{-1} and TS **3-4** *S*: +5 kJ mol^{-1}), enhancing the ΔΔG of the two enantiomers by 10 kJ mol^{-1}. The lowest and inverse e.e. (<-54) is detected in the other extreme case, in which the formation of the S-enantiomer is made more favourable while simultaneously lowering the barrier of the *R*-path (TS **3-4** *R*: +5 kJ mol^{-1} and TS **3-4** *S*: -5 kJ mol^{-1}). Small variations in the barrier height of the rate-determining step (TS **4-5**, Figure 5.6b) lead to a range in e.e. of 63% to 88%. This range of e.e. is narrower than that observed upon the variation of the enantiodetermining step only. Regarding simultaneous variations of rate-determining and enantiodetermining steps,

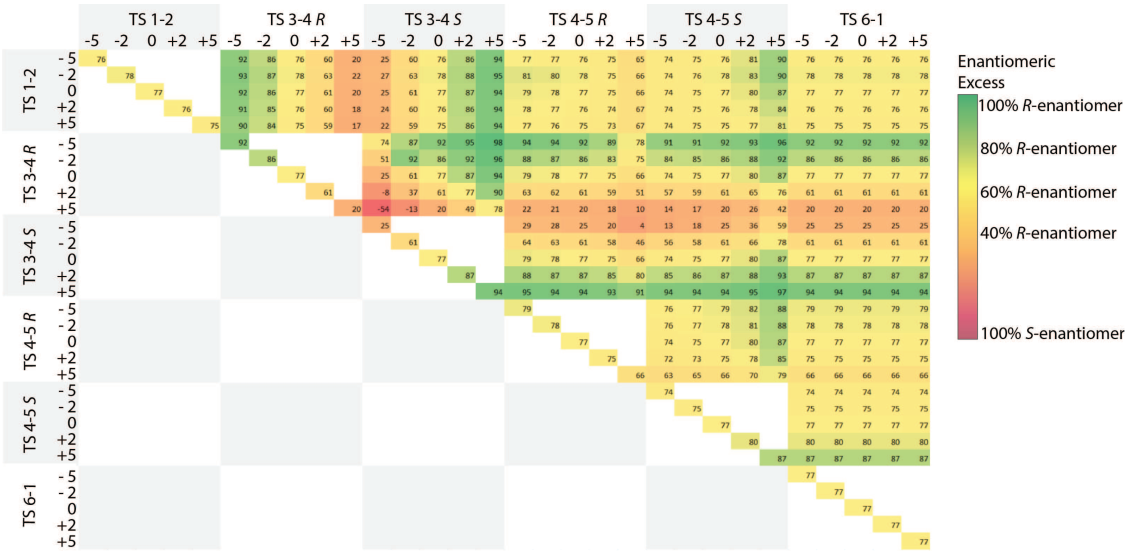

		TS 1-2					TS 3-4 *R*					TS 3-4 *S*					TS 4-5 *R*					TS 4-5 *S*					TS 6-1				
		-5	-2	0	+2	+5	-5	-2	0	+2	+5	-5	-2	0	+2	+5	-5	-2	0	+2	+5	-5	-2	0	+2	+5	-5	-2	0	+2	+5
TS 1-2	- 5	76					92	86	76	60	20	25	60	76	86	94	77	77	76	75	65	74	75	76	81	90	76	76	76	76	76
	- 2		78				93	87	78	63	22	27	63	78	88	95	81	80	78	75	66	74	76	78	83	90	78	78	78	78	78
	0			77			92	86	77	61	20	25	61	77	87	94	79	78	77	75	66	74	75	77	80	87	77	77	77	77	77
	+2				76		91	85	76	60	18	24	60	76	86	94	78	77	76	74	67	74	75	76	78	84	76	76	76	76	76
	+5					75	90	84	75	59	17	22	59	75	86	94	77	76	75	73	67	74	75	75	77	81	75	75	75	75	75
TS 3-4 *R*	- 5						92					74	87	92	95	98	94	94	92	89	78	91	91	92	93	96	92	92	92	92	92
	- 2							86				51	92	86	92	96	88	87	86	83	75	84	85	86	88	92	86	86	86	86	86
	0								77			25	61	77	87	94	79	78	77	75	66	74	75	77	80	87	77	77	77	77	77
	+2									61		-8	37	61	77	90	63	62	61	59	51	57	59	61	65	76	61	61	61	61	61
	+5										20	-54	-13	20	49	78	22	21	20	18	10	14	17	20	26	42	20	20	20	20	20
TS 3-4 *S*	- 5											25					29	28	25	20	4	13	18	25	36	59	25	25	25	25	25
	- 2												61				64	63	61	58	46	56	58	61	66	78	61	61	61	61	61
	0													77			79	78	77	75	66	74	75	77	80	87	77	77	77	77	77
	+2														87		88	87	87	85	80	85	86	87	88	93	87	87	87	87	87
	+5															94	95	94	94	93	91	94	94	94	95	97	94	94	94	94	94
TS 4-5 *R*	- 5																79					76	77	79	82	88	79	79	79	79	79
	- 2																	78				76	77	78	81	88	78	78	78	78	78
	0																		77			74	75	77	80	87	77	77	77	77	77
	+2																			75		72	73	75	78	85	75	75	75	75	75
	+5																				66	63	65	66	70	79	66	66	66	66	66
TS 4-5 *S*	- 5																					74					74	74	74	74	74
	- 2																						75				75	75	75	75	75
	0																							77			77	77	77	77	77
	+2																								80		80	80	80	80	80
	+5																									87	87	87	87	87	87
TS 6-1	- 5																										77				
	- 2																											77			
	0																												77		
	+2																													77	
	+5																														77

Figure 5.4: Multidimensional analysis of the transition state barriers (TS). Barriers were varied by -5 to 5 kJ mol^{-1}. Enantiomeric excess is displayed by a colour scale, dark green indicating high selectivity for the *R*-enantiomer and red indicating a dominance of the *S*-alcohol.

we can see that the rate-determining step can add to the effect that was already observed during the increase and decrease of the barrier of the enantiodetermining step (Figure 5.6c and d). The lowest e.e. value that was observed when only the barrier of the enatiodetermative step (TS **3-4** *R*: +5 kJ mol^{-1}) was changed by 20%. When the rate-determining step is altered concurrently (TS **3-4** *S*: -5 kJ mol^{-1} and TS **4-5** *R*: +5 kJ mol^{-1}) the selectivity can be decreased further to 4% e.e.

The analysis of the enantioselective excess shows that uncertainties in the computed free energy barriers for the stereo-inducing steps have a very significant effect on the selectivity. Especially the enantiodetermining reaction step dictates the selectivity of the reaction and is therefore most susceptible to changes in the barrier. Furthermore, our analysis demonstrates that the energetics of the rate-determining step also has a significant effect, introducing a change in selectivity by ca.10% when altered on its own and an additional change of 15% e.e. when the respective barriers are varied simultaneously with those of the enantiodetermative step. Next, the evolution of enantiomeric excess with substrate conversions was compared to data from the kinetic experiment. To analyse the data comprehensibly, the experimental e.e. at different conversion was compared to the data points obtained in the microkinetic model. The root mean square difference (RMSD) was calculated for these points and an analysis of changes in the trajectory was conducted when changing the barrier of transition states by 5, 2, -2 and -5 kJ mol^{-1} as shown in Figure 5.7. An example of how the MKM trajectory evolves for the original computed barriers and the best fit determined when changing the transition state energies compared to the experimentally determined data points is illustrated in Figure 5.5. The analysis of the changes in RMSD values is displayed in Figure 5.7. The alteration of computed transition states by 5 kJ mol^{-1} in one transition state can change the trajectory from a good fit shown in green to a poor fit depicted in

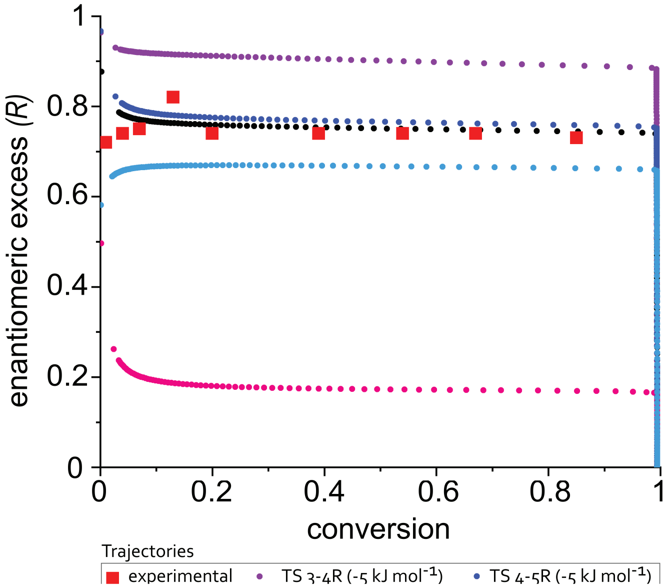

Figure 5.5: Trajectories of enantiomeric excess developing as a function of conversion of the experimental data (red) and various microkinetic model runs.

red. For the original unaltered pathway an RMSD of 4.4 is observed. Results of alterations in a single transition state are shown on the diagonal axis. The greatest effect is again observed by the transition state introducing stereoselectivity (TS **3-4**), inducing an RMSD value of almost 52 upon the increase of the respective TS **3-4** *R* barrier by 5 kJ mol^{-1}. Also the rate-determining step (TS **4-5**) has a significant effect on the trajectory, changing the RMSD to almost 16. In line with the prior analysis, the final step in the cycle TS **6-1** has no effect on the predictive power of the MKM. However, when the first reaction step (TS **1-2**), in which the Mn-hydride is formed, is reduced by 5kJ mol^{-1} it results in the best fit (RMSD=3.2). By reducing the barrier an initially higher e.e. value is achieved, which is also observed in the experimental data array. At 15% ester conversion the e.e. value accounts to 85%, which decreases in time until it levels of at around 77%.

The RMSD analysis of the variation of two concurrent reaction steps is in line with the results observed in the enantiomeric excess analysis. The stereospecific transition states (TS **3-4**, TS **4-5**) have the greatest impact on the trajectory, while varying the two other barriers (TS **1-2**, TS **6-1**) leads to little deviation from the trajectory. Conversely, when altering the reaction step leading to the formation of *R*- and *S*-phenylethanol simultaneously, the trajectory can be influenced significantly. Looking at the enantiodetermining step (TS **3-4**), decreasing both enantiomers by 5 kJ mol^{-1} leads to a very good fit with a RMSD with 2.6 (TS **3-4** *R*: -5 kJ mol^{-1} and TS **3-4** *S*: -5 kJ mol^{-1}). An increase in both barriers of the rate determining step (TS **4-5**) by 5 kJ mol^{-1} leads to a much poorer fit with a RMSD of 6 (TS **4-5** *R*: +5 kJ mol^{-1} and TS **4-5** *S*: +5 kJ mol^{-1}). Importantly, these changes do not affect the $\Delta\Delta G^{\ddagger}$ differences for the competing reaction channels.

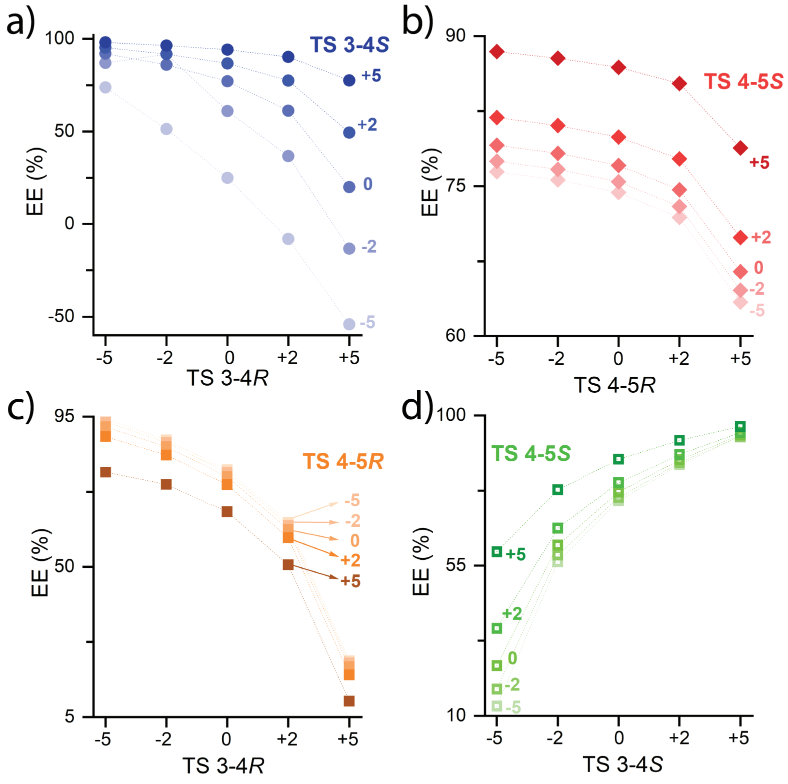

Figure 5.6: The effect of variation of two transition state barriers on the enantiomeric excess. The x-axis illustrates the changes from -5 to +5 kJ mol^{-1} in the first TS barrier. The changes in the second TS barrier is plotted in five different scattering plots, also varying from -5 to +5 kJ mol^{-1}, showing the resulting e.e. on the y-axis.

5.4. Conclusion

Herein we analysed the impact of the uncertainties in computed barriers and detailization of the kinetic model on the predicted enantioselectivity of a model ketone transfer hydrogenation reaction by a homogeneous Mn(I)-diamine catalyst. During the analysis we have focused on comparing the enantiomeric excess achieved during the progress of the reaction to concentration profiles from the analysis from microkinetic modelling. The predicted trajectory and the achieved enantiomeric excess at different stages of the reaction was compared to experimental data.

The microkinetic model that was built upon the reaction energy diagram calculate by DFT confirms that the enantiodetermining step influences the selectivity to the greatest extent. The rate-determining step can also vary the enantioselective excess significantly. The final e.e. is least influence by the two non-stereospecific steps.

However, the RMSD analysis showed that the time evolution of the enantiomeric excess can be affected by steps which are not affecting the final selectivity. This is the case since the enantioselective excess varies throughout the reaction trajectory.

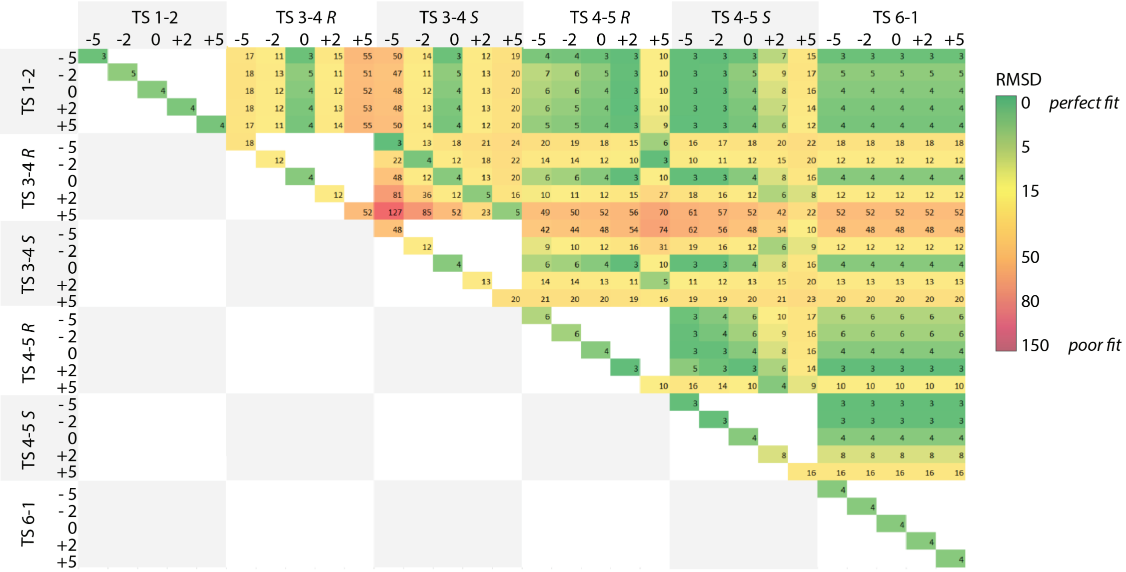

		TS 1-2					TS 3-4 *R*					TS 3-4 *S*					TS 4-5 *R*					TS 4-5 *S*					TS 6-1				
		-5	-2	0	+2	+5	-5	-2	0	+2	+5	-5	-2	0	+2	+5	-5	-2	0	+2	+5	-5	-2	0	+2	+5	-5	-2	0	+2	+5
TS 1-2	- 5	3					17	11	3	15	55	50	14	3	12	19	4	4	3	3	10	3	3	3	7	15	3	3	3	3	3
	- 2		5				18	13	5	11	51	47	11	5	13	20	7	6	5	3	10	3	3	5	9	17	5	5	5	5	5
	0			4			18	12	4	12	52	48	12	4	13	20	6	6	4	3	10	3	3	4	8	16	4	4	4	4	4
	+2				4		18	12	4	13	53	48	13	4	13	20	6	5	4	3	10	3	3	4	7	14	4	4	4	4	4
	+5					4	17	11	4	14	55	50	14	4	12	20	5	5	4	3	9	3	3	4	6	12	4	4	4	4	4
TS 3-4 *R*	- 5						18					3	13	18	21	24	20	19	18	15	6	16	17	18	20	22	18	18	18	18	18
	- 2							12				22	4	12	18	22	14	14	12	10	3	10	11	12	15	20	12	12	12	12	12
	0								4			48	12	4	13	20	6	6	4	3	10	3	3	4	8	16	4	4	4	4	4
	+2									12		81	36	12	5	16	10	11	12	15	27	18	16	12	6	8	12	12	12	12	12
	+5										52	127	85	52	23	5	49	50	52	56	70	61	57	52	42	22	52	52	52	52	52
TS 3-4 *S*	- 5											48					42	44	48	54	74	62	56	48	34	10	48	48	48	48	48
	- 2												12				9	10	12	16	31	19	16	12	6	9	12	12	12	12	12
	0													4			6	6	4	3	10	3	3	4	8	16	4	4	4	4	4
	+2														13		14	14	13	11	5	11	12	13	15	20	13	13	13	13	13
	+5															20	21	20	20	19	16	19	19	20	21	23	20	20	20	20	20
TS 4-5 *R*	- 5																6					3	4	6	10	17	6	6	6	6	6
	- 2																	6				3	4	6	9	16	6	6	6	6	6
	0																		4			3	3	4	8	16	4	4	4	4	4
	+2																			3		5	3	3	6	14	3	3	3	3	3
	+5																				10	16	14	10	4	9	10	10	10	10	10
TS 4-5 *S*	- 5																					3					3	3	3	3	3
	- 2																						3				3	3	3	3	3
	0																							4			4	4	4	4	4
	+2																								8		8	8	8	8	8
	+5																									16	16	16	16	16	16
TS 6-1	- 5																										4				
	- 2																											4			
	0																												4		
	+2																													4	
	+5																														4

Figure 5.7: Root mean square deviation analysis of the e.e. versus conversion trajectory with variations in transition state barriers. Barriers were varied by -5 to 5 kJ mol^{-1}. The RMSD is displayed by a colour scale, dark green indicating a good fit and red representing a poor fit with the experimental data.

Also here, the trajectory is most significantly influenced by the enantiodetermining step, followed by the rate-determining step.

In conclusion, we showed that the variations of the free energy barriers within the DFT uncertainty range of 10 kJ mol^{-1} can give rise to a complete reverse of the predicted enantioselectivity. Therefore, our analysis shows that an uncertainty of 5 kJ mol^{-1} in one transition state makes it impossible to predict reliably the enantioselective excess.

5.5. Experimental Section

All DFT calculations were carried out with the Gaussian16 C0.1 package.[51] The geometries of reaction intermediates and transition states were optimized with the PBE0-D3(BJ)/ def2-TZVP functional and basis set with a SMD solvent correction for isopropanol.[52] An ultrafine grid was uniformly used. The nature of each stationary point was confirmed by frequency analysis in which zero imaginary frequencies for minima and one for transition states were found. Reaction (ΔE) and activation energies (ΔE‡) were corrected for zero-point energy (ZPE) from the normal-mode frequency analysis. Electronic energies (ΔE) and entropies (ΔS) were used For the microkinetic model an in-house python script was used and the reaction kinetics was derived for a batch-type reactor. Reaction rate constants were calculated using the Eyring equation. The differential equations were solved with the real-valued variable-coefficient ordinary differential equation solver (vode) embedded in the python SciPy package, with the backward differentiation formulas (BDF) implementation for stiff problems. The relative and absolute tolerances were set at 1e-12. Time integration until reaching steady state was applied. The initial conditions of the MKM were based on the experimental conditions with 1:1:0.05 ratio of acetophenone to isopropanol to catalyst. The enantiomeric excess was determined at 70% conversion by the equation given in the previous section, using the concentrations of *R*- and *S*-phenylethanol. To determine the root mean square deviation (RMSD) the points of conversion and the measured e.e. from experimental data were compared to the nearest point of conversion in the microkinetic trajectory. The data points were processed with the formula for RMSD:

$$RMSD = \sqrt{\frac{\sum_{n=1}^{N}(\hat{y}_n - y_n)^2}{N}}$$

where $\hat{y}_n$ is the predicted enantiomeric excess from the microkinetic model, y_n is the observed e.e. from the experimental trajectory and N is the number of total data points regarded, which was 9.

Elementray Reactions Steps

Below, the elementary reactions are summarized.

$$\begin{aligned}\frac{d[1]}{dt} = &-(k_{1-2NH1} * [1] - k_{2NH1-1} * [2NH1]) - (k_{1-2NH2} * [1] - k_{2NH2-1} * [2NH2]) \\ &+(k_{1-6NH1} * [6NH1] - k_{1-6NH1} * [1]) \\ &+(k_{1-6NH2} * [6NH2] - k_{1-6NH2} * [1])\end{aligned}$$

$$\begin{aligned}\frac{d[2NH1]}{dt} = &+(k_{1-2NH1} * [1] - k_{2NH1-1} * [2NH1]) - (k_{2NH1-3RNH1} * [2NH1] \\ &*[acetophenone] - k_{3RNH1-2NH1} * [3RNH1] * [acetone]) - (k_{2NH1-3SNH1} * [2NH1] \\ &*[acetophenone] - k_{3SNH1-2NH1} * [3SNH1] * [acetone])\end{aligned}$$

$$\begin{aligned}\frac{d[2NH2]}{dt} = &+(k_{1-2NH2} * [1] - k_{2NH2-1} * [2NH2]) - (k_{2NH2-3RNH2} * [2NH2] \\ &*[acetophenone] - k_{3RNH2-2NH2} * [3RNH2] * [acetone]) - (k_{2NH2-3SNH2} \\ &*[2NH2] * [acetophenone] - k_{3SNH2-2NH2} * [3SNH2] * [acetone])\end{aligned}$$

$$\begin{aligned}\frac{d[3RNH1]}{dt} = &+(k_{2NH1-3RNH1} * [2NH1] * [acetophenone] - k_{3RNH1-2NH1} * [3RNH1] \\ &*[acetone]) - (k_{3RNH1-4R} * [3RNH1] - k_{4R-3RNH1} * [4R])\end{aligned}$$

$$\begin{aligned}\frac{d[3SNH1]}{dt} = &+(k_{2NH1-3SNH1} * [2NH1] * [acetophenone] - k_{3SNH1-2NH1} * [3SNH1] \\ &*[acetone]) - (k_{3SNH1-4S} * [3SNH1] - k_{4S-3SNH1} * [4S])\end{aligned}$$

$$\frac{d[3RNH2]}{dt} = +(k_{2NH2-3RNH2} * [2NH2] * [acetophenone] - k_{3RNH2-2NH2} * [3RNH2] * [acetone]) - (k_{3RNH2-4R} * [3RNH2] - k_{4R-3RNH2} * [4R])$$

$$\frac{d[3SNH2]}{dt} = +(k_{2NH2-3SNH2} * [2NH2] * [acetophenone] - k_{3SNH2-2NH2} * [3SNH2] * [acetone]) - (k_{3SNH2-4S} * [3SNH2] - k_{4S-3SNH2} * [4S])$$

$$\frac{d[4R]}{dt} = +(k_{3RNH1-4R} * [3RNH1] - k_{4R-3RNH1} * [4R]) + (k_{3RNH2-4R} * [3RNH2] - k_{4R-3RNH1} * [4R]) - (k_{4R-5RNH1} * [4R] - k_{5RNH1-4R} * [5RNH1]) - (k_{4R-5RNH2} * [4R] - k_{5RNH2-4R} * [5RNH2])$$

$$\frac{d[4S]}{dt} = +(k_{3SNH1-4S} * [3SNH1] - k_{4S-3SNH1} * [4S]) + (k_{3SNH2-4S} * [3SNH2] - k_{4S-3SNH1} * [4S]) - (k_{4S-5SNH1} * [4S] - k_{5SNH1-4S} * [5SNH1]) - (k_{4S-5SNH2} * [4S] - k_{5SNH2-4S} * [5SNH2])$$

$$\frac{d[5RNH1]}{dt} = +(k_{4R-5RNH1} * [4R] - k_{5RNH1-4R} * [5RNH1]) - (k_{5RNH1-6NH1} * [5RNH1] * [IPA] - k_{6NH1-5RNH1} * [6NH1] * [RPhCH(OH)CH3])$$

$$\frac{d[5SNH1]}{dt} = +(k_{4S-5SNH1} * [4S] - k_{5SNH1-4S} * [5SNH1]) - (k_{5SNH1-6NH1} * [5SNH1] * [IPA] - k_{6NH1-5SNH1} * [6NH1] * [SPhCH(OH)CH3])$$

$$\frac{d[5RNH2]}{dt} = +(k_{4R-5RNH2} * [4R] - k_{5RNH2-4R} * [5RNH2]) - (k_{5RNH2-6NH2} * [5RNH2] * [IPA] - k_{6NH2-5RNH2} * [6NH2] * [RPhCH(OH)CH3])$$

$$\frac{d[5SNH2]}{dt} = +(k_{4S-5SNH2} * [4S] - k_{5SNH2-4S} * [5SNH2]) - (k_{5SNH2-6NH2} * [5SNH2] * [IPA] - k_{6NH2-5SNH2} * [6NH2] * [SPhCH(OH)CH3])$$

$$\frac{d[6NH1]}{dt} = +(k_{5RNH1-6NH1} * [5RNH1] * [IPA] - k_{6NH1-5RNH1} * [6NH1] * [RPhCH(OH)CH3]) + (k_{5SNH1-6NH1} * [5SNH1] * [IPA] - k_{6NH1-5SNH1} * [6NH1] * [SPhCH(OH)CH3]) - (k_{6NH1-1} * [6NH1] - k_{1-6NH1} * [1])$$

$$\begin{aligned}\frac{d[6NH2]}{dt} = {} & +(k_{5RNH2-6NH2} * [5RNH2] * [IPA] - k_{6NH2-5RNH2} * [6NH2] * [RPhCH(OH)CH3]) \\ & +(k_{5SNH2-6NH2} * [5SNH2] * [IPA] - k_{6NH2-5SNH2} * [6NH2] * [SPhCH(OH)CH3]) \\ & -(k_{6NH2-1} * [6NH2] - k_{1-6NH2} * [1])\end{aligned}$$

$$\begin{aligned}\frac{d[acetophenone]}{dt} = {} & -(k_{2NH1-3RNH1} * [2NH1] * [acetophenone] - k_{3RNH1-2NH1} * [3RNH1] \\ & *[acetone]) - (k_{2NH1-3SNH1} * [2NH1] * [acetophenone] - k_{3SNH1-2NH1} \\ & *[3SNH1] * [acetone]) - (k_{2NH2-3RNH2} * [2NH2] * [acetophenone] \\ & -k_{3RNH2-2NH2} * [3RNH2] * [acetone]) - (k_{2NH2-3SNH2} * [2NH2] \\ & *[acetophenone] - k_{3SNH2-2NH2} * [3SNH2] * [acetone])\end{aligned}$$

$$\begin{aligned}\frac{d[acetone]}{dt} = {} & +(k_{2NH1-3RNH1} * [2NH1] * [acetophenone] - k_{3RNH1-2NH1} * [3RNH1]* \\ & [acetone]) + (k_{2NH1-3SNH1} * [2NH1] * [acetophenone] - k_{3SNH1-2NH1} \\ & *[3SNH1] * [acetone]) + (k_{2NH2-3RNH2} * [2NH2] * [acetophenone] \\ & -k_{3RNH2-2NH2} * [3RNH2] * [acetone]) + (k_{2NH2-3SNH2} * [2NH2] \\ & *[acetophenone] - k_{3SNH2-2NH2} * [3SNH2] * [acetone])\end{aligned}$$

$$\begin{aligned}\frac{d[IPA]}{dt} = {} & -(k_{5RNH1-6NH1} * [5RNH1] * [IPA] - k_{6NH1-5RNH1} * [6NH1] * [RPhCH(OH)CH3]) \\ & -(k_{5SNH1-6NH1} * [5SNH1] * [IPA] - k_{6NH1-5SNH1} * [6NH1] * [SPhCH(OH)CH3]) \\ & -(k_{5RNH2-6NH2} * [5RNH2] * [IPA] - k_{6NH2-5RNH2} * [6NH2] * [RPhCH(OH)CH3]) \\ & -(k_{5SNH2-6NH2} * [5SNH2] * [IPA] - k_{6NH2-5SNH2} * [6NH2] * [SPhCH(OH)CH3])\end{aligned}$$

$$\begin{aligned}\frac{d[RPhCH(OH)CH3]}{dt} = {} & +(k_{5RNH1-6NH1} * [5RNH1] * [IPA] - k_{6NH1-5RNH1} * [6NH1] \\ & *[RPhCH(OH)CH3]) + (k_{5RNH2-6NH2} * [5RNH2] * [IPA] \\ & -k_{6NH2-5RNH2} * [6NH2] * [RPhCH(OH)CH3])\end{aligned}$$

$$\begin{aligned}\frac{d[SPhCH(OH)CH3]}{dt} = {} & +(k_{5SNH1-6NH1} * [5SNH1] * [IPA] - k_{6NH1-5SNH1} * [6NH1] \\ & *[SPhCH(OH)CH3]) + (k_{5SNH2-6NH2} * [5SNH2] * [IPA] \\ & -k_{6NH2-5SNH2} * [6NH2] * [SPhCH(OH)CH3])\end{aligned}$$

References

[1] A. M. Krieger and E. A. Pidko, *The Impact of Computational Uncertainties on the Enantioselectivity Predictions: A Microkinetic Modeling of Ketone Transfer Hydrogenation with a Noyori-type Mn-diamine Catalyst,* ChemCatChem , cctc.202100341 (2021).

[2] W. A. Nugent, T. V. RajanBabu, and M. J. Burk, *Beyond Nature's Chiral Pool: Enantioselective Catalysis in Industry,* Science (80-.). **259**, 479 (1993).

[3] S. Hammes-Schiffer, *Catalysts by Design: The Power of Theory,* Acc. Chem. Res. **50**, 561 (2017).

[4] J. P. Janet, S. Ramesh, C. Duan, and H. J. Kulik, *Accurate Multiobjective Design in a Space of Millions of Transition Metal Complexes with Neural-Network-Driven Efficient Global Optimization,* ACS Cent. Sci. **6**, 513 (2020).

[5] H. J. Kulik, *Making machine learning a useful tool in the accelerated discovery of transition metal complexes,* WIREs Comput. Mol. Sci. **10** (2020), 10.1002/wcms.1439.

[6] M. Foscato and V. R. Jensen, *Automated in Silico Design of Homogeneous Catalysts,* ACS Catal. **10**, 2354 (2020).

[7] J. P. Reid and M. S. Sigman, *Comparing quantitative prediction methods for the discovery of small-molecule chiral catalysts,* Nat. Rev. Chem. **2**, 290 (2018).

[8] J. P. Reid and M. S. Sigman, *Holistic prediction of enantioselectivity in asymmetric catalysis,* Nature **571**, 343 (2019).

[9] A. Zirakzadeh, S. R. M. M. de Aguiar, B. Stöger, M. Widhalm, and K. Kirchner, *Enantioselective Transfer Hydrogenation of Ketones Catalyzed by a Manganese Complex Containing an Unsymmetrical Chiral PNP' Tridentate Ligand,* ChemCatChem **9**, 1744 (2017).

[10] M. Garbe, K. Junge, S. Walker, Z. Wei, H. Jiao, A. Spannenberg, S. Bachmann, M. Scalone, and M. Beller, *Manganese(I)-Catalyzed Enantioselective Hydrogenation of Ketones Using a Defined Chiral PNP Pincer Ligand,* Angew. Chemie Int. Ed. **56**, 11237 (2017).

[11] R. H. Morris, *Iron Group Hydrides in Noyori Bifunctional Catalysis,* Chem. Rec. **16**, 2644 (2016).

[12] C. Gunanathan and D. Milstein, *Applications of Acceptorless Dehydrogenation and Related Transformations in Chemical Synthesis,* Science (80-.). **341**, 1229712 (2013).

[13] M. Trincado, D. Banerjee, and H. Grützmacher, *Molecular catalysts for hydrogen production from alcohols,* Energy Environ. Sci. **7**, 2464 (2014).

[14] G. Ujaque and F. Maseras, *Applications of Hybrid DFT/Molecular Mechanics to Homogeneous Catalysis,* (2004) pp. 117–150.

[15] M. G. Quesne, F. Silveri, N. H. de Leeuw, and C. R. A. Catlow, *Advances in Sustainable Catalysis: A Computational Perspective,* Front. Chem. **7** (2019), 10.3389/fchem.2019.00182.

[16] T. Sperger, I. A. Sanhueza, I. Kalvet, and F. Schoenebeck, *Computational Studies of Synthetically Relevant Homogeneous Organometallic Catalysis Involving Ni, Pd, Ir, and Rh: An Overview of Commonly Employed DFT Methods and Mechanistic Insights,* Chem. Rev. **115**, 9532 (2015).

[17] J. Daubignard, R. J. Detz, A. C. H. Jans, B. de Bruin, and J. N. H. Reek, *Rational Optimization of Supramolecular Catalysts for the Rhodium-Catalyzed Asymmetric Hydrogenation Reaction,* Angew. Chemie Int. Ed. **56**, 13056 (2017).

[18] K. P. Kepp, *Accuracy of theoretical catalysis from a model of iron-catalyzed ammonia synthesis,* Commun. Chem. **1**, 63 (2018).

[19] R. J. Meier, *Are current DFT methods sufficiently reliable for real-world molecular systems?* Faraday Discuss. **124**, 405 (2003).

[20] M. Besora and F. Maseras, *Microkinetic modeling in homogeneous catalysis,* WIREs Comput. Mol. Sci. **8** (2018), 10.1002/wcms.1372.

[21] J. Pritchard, G. A. Filonenko, R. van Putten, E. J. M. Hensen, and E. A. Pidko, *Heterogeneous and homogeneous catalysis for the hydrogenation of carboxylic acid derivatives: history, advances and future directions,* Chem. Soc. Rev. **44**, 3808 (2015).

[22] J. Magano and J. R. Dunetz, *Large-Scale Carbonyl Reductions in the Pharmaceutical Industry,* Org. Process Res. Dev. **16**, 1156 (2012).

[23] R. Noyori, *Asymmetric Catalysis: Science and Opportunities (Nobel Lecture),* Angew. Chemie Int. Ed. **41**, 2008 (2002).

[24] H.-U. Blaser, C. Malan, B. Pugin, F. Spindler, H. Steiner, and M. Studer, *Selective Hydrogenation for Fine Chemicals: Recent Trends and New Developments,* Adv. Synth. Catal. **345**, 103 (2003).

[25] R. C. Hoye, *Reductions by the Alumino- and Borohydrides in Organic Synthesis, 2nd edition (Seyden-Penne, Jacqueline),* J. Chem. Educ. **76**, 33 (1999).

[26] G. W. Gribble, *Sodium borohydride in carboxylic acid media: a phenomenal reduction system,* Chem. Soc. Rev. **27**, 395 (1998).

[27] S. Werkmeister, J. Neumann, K. Junge, and M. Beller, *Pincer-Type Complexes for Catalytic (De)Hydrogenation and Transfer (De)Hydrogenation Reactions: Recent Progress,* Chem. - A Eur. J. **21**, 12226 (2015).

[28] P. A. Dub and T. Ikariya, *Catalytic Reductive Transformations of Carboxylic and Carbonic Acid Derivatives Using Molecular Hydrogen,* ACS Catal. **2**, 1718 (2012).

[29] H.-U. Blaser, B. Pugin, and F. Spindler, *Asymmetric Hydrogenation,* (2012) pp. 65–102.

[30] K. Matsumura, N. Arai, K. Hori, T. Saito, N. Sayo, and T. Ohkuma, *Chiral Ruthenabicyclic Complexes: Precatalysts for Rapid, Enantioselective, and Wide-Scope Hydrogenation of Ketones,* J. Am. Chem. Soc. **133**, 10696 (2011).

[31] W. Kuriyama, T. Matsumoto, O. Ogata, Y. Ino, K. Aoki, S. Tanaka, K. Ishida, T. Kobayashi, N. Sayo, and T. Saito, *Catalytic Hydrogenation of Esters. Development of an Efficient Catalyst and Processes for Synthesising (R)-1,2-Propanediol and 2-(l-Menthoxy)ethanol,* Org. Process Res. Dev. **16**, 166 (2012).

[32] T. Ikariya, K. Murata, and R. Noyori, *Bifunctional transition metal-based molecular catalysts for asymmetric syntheses,* Org. Biomol. Chem. **4**, 393 (2006).

[33] T. Ikariya and A. J. Blacker, *Asymmetric Transfer Hydrogenation of Ketones with Bifunctional Transition Metal-Based Molecular Catalysts †,* Acc. Chem. Res. **40**, 1300 (2007).

[34] F. Foubelo, C. Nájera, and M. Yus, *Catalytic asymmetric transfer hydrogenation of ketones: recent advances,* Tetrahedron: Asymmetry **26**, 769 (2015).

[35] T. Touge, T. Hakamata, H. Nara, T. Kobayashi, N. Sayo, T. Saito, Y. Kayaki, and T. Ikariya, *Oxo-Tethered Ruthenium(II) Complex as a Bifunctional Catalyst for Asymmetric Transfer Hydrogenation and H2 Hydrogenation,* J. Am. Chem. Soc. **133**, 14960 (2011).

[36] M. B. Widegren, G. J. Harkness, A. M. Z. Slawin, D. B. Cordes, and M. L. Clarke, *A Highly Active Manganese Catalyst for Enantioselective Ketone and Ester Hydrogenation,* Angew. Chemie Int. Ed. **56**, 5825 (2017).

[37] F. León, A. Comas-Vives, E. Álvarez, and A. Pizzano, *A combined experimental and computational study to decipher complexity in the asymmetric hydrogenation of imines with Ru catalysts bearing atropisomerizable ligands,* Catal. Sci. Technol. **11**, 2497 (2021).

[38] P. A. Dub and J. C. Gordon, *Metal–Ligand Bifunctional Catalysis: The "Accepted" Mechanism, the Issue of Concertedness, and the Function of the Ligand in Catalytic Cycles Involving Hydrogen Atoms,* ACS Catal. **7**, 6635 (2017).

[39] P. A. Dub and J. C. Gordon, *The mechanism of enantioselective ketone reduction with Noyori and Noyori–Ikariya bifunctional catalysts,* Dalt. Trans. **45**, 6756 (2016).

[40] C. Gunanathan and D. Milstein, *Bond Activation and Catalysis by Ruthenium Pincer Complexes,* Chem. Rev. **114**, 12024 (2014).

[41] R. Noyori and S. Hashiguchi, *Asymmetric Transfer Hydrogenation Catalyzed by Chiral Ruthenium Complexes,* Acc. Chem. Res. **30**, 97 (1997).

[42] S. E. Clapham, A. Hadzovic, and R. H. Morris, *Mechanisms of the H2-hydrogenation and transfer hydrogenation of polar bonds catalyzed by ruthenium hydride complexes,* Coord. Chem. Rev. **248**, 2201 (2004).

[43] R. Malacea, R. Poli, and E. Manoury, *Asymmetric hydrosilylation, transfer hydrogenation and hydrogenation of ketones catalyzed by iridium complexes,* Coord. Chem. Rev. **254**, 729 (2010).

[44] R. H. Morris, *Exploiting Metal–Ligand Bifunctional Reactions in the Design of Iron Asymmetric Hydrogenation Catalysts,* Acc. Chem. Res. **48**, 1494 (2015).

[45] W. Ai, R. Zhong, X. Liu, and Q. Liu, *Hydride Transfer Reactions Catalyzed by Cobalt Complexes,* Chem. Rev. **119**, 2876 (2019).

[46] P. A. Dub and J. C. Gordon, *The role of the metal-bound N–H functionality in Noyori-type molecular catalysts,* Nat. Rev. Chem. **2**, 396 (2018).

[47] S. Hashiguchi, A. Fujii, J. Takehara, T. Ikariya, and R. Noyori, *Asymmetric Transfer Hydrogenation of Aromatic Ketones Catalyzed by Chiral Ruthenium(II) Complexes,* J. Am. Chem. Soc. **117**, 7562 (1995).

[48] P. A. Dub, N. J. Henson, R. L. Martin, and J. C. Gordon, *Unravelling the Mechanism of the Asymmetric Hydrogenation of Acetophenone by [RuX2 (diphosphine)(1,2-diamine)] Catalysts,* J. Am. Chem. Soc. **136**, 3505 (2014).

[49] V. Schurig, *Terms for the Quantitation of a Mixture of Stereoisomers,* (2013) pp. 21–40.

[50] R. E. Gawley, *Do the Terms "% ee" and "% de" Make Sense as Expressions of Stereoisomer Composition or Stereoselectivity?* J. Org. Chem. **71**, 2411 (2006).

[51] M. J. Frisch, G. W. Trucks, H. B. Schlegel, G. E. Scuseria, M. A. Robb, J. R. Cheeseman, G. Scalmani, V. Barone, G. A. Petersson, H. Nakatsuji, X. Li, M. Caricato, A. V. Marenich, J. Bloino, B. G. Janesko, R. Gomperts, B. Mennucci, H. P. Hratchian, J. V. Ortiz, A. F. Izmaylov, J. L. Sonnenberg, D. Williams-Young, F. Ding, F. Lipparini, F. Egidi, J. Goings, B. Peng, A. Petrone, T. Henderson, D. Ranasinghe, V. G. Zakrzewski, J. Gao, N. Rega, G. Zheng, W. Liang, M. Hada, M. Ehara, K. Toyota, R. Fukuda, J. Hasegawa, M. Ishida, T. Nakajima, Y. Honda, O. Kitao, H. Nakai, T. Vreven, K. Throssell, J. A. Montgomery Jr., J. E. Peralta, F. Ogliaro, M. J. Bearpark, J. J. Heyd, E. N. Brothers, K. N. Kudin, V. N. Staroverov, T. A. Keith, R. Kobayashi, J. Normand, K. Raghavachari, A. P. Rendell, J. C. Burant, S. S. Iyengar, J. Tomasi, M. Cossi, J. M. Millam, M. Klene, C. Adamo, R. Cammi, J. W. Ochterski, R. L. Martin, K. Morokuma, O. Farkas, J. B. Foresman, and D. J. Fox, *Gaussian16 Revision C.01,* (2016).

[52] A. V. Marenich, C. J. Cramer, and D. G. Truhlar, *Universal Solvation Model Based on Solute Electron Density and on a Continuum Model of the Solvent*

Defined by the Bulk Dielectric Constant and Atomic Surface Tensions, J. Phys. Chem. B **113**, 6378 (2009).

6

Solvent-Assisted Ketone Reduction

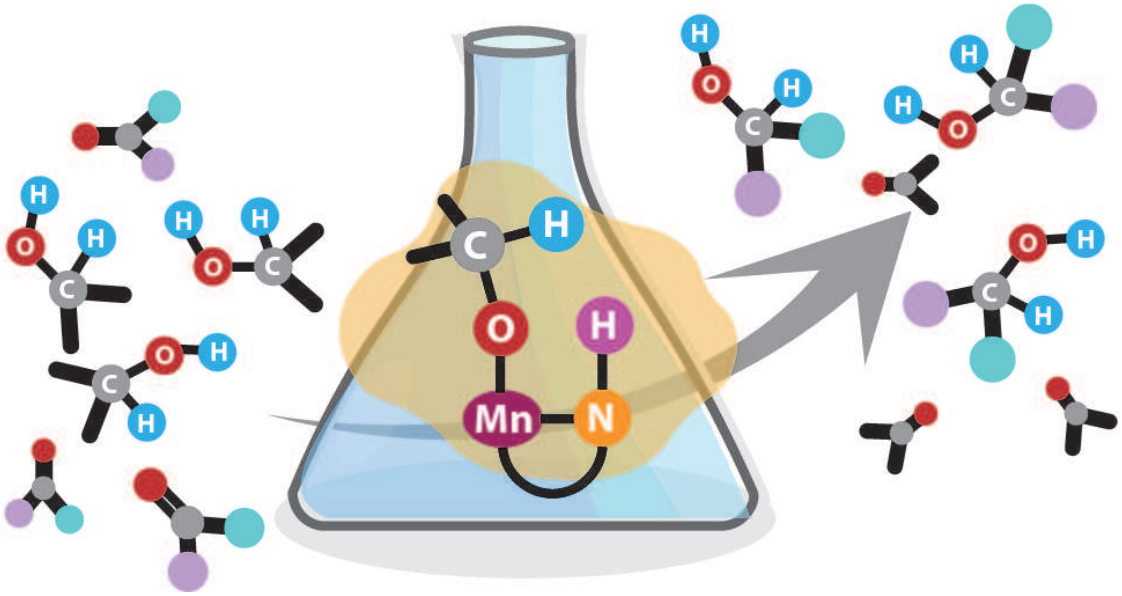

This chapter has been submitted to Organometallics

The choice of solvent and reaction conditions often defines the overall behaviour of a homogeneous catalytic system by affecting the preferred reaction mechanism and thus the activity and selectivity of the catalytic process. Here, we explore the role of solvation in the mechanism of ketone reduction by a model representative bifunctional Mn-diamine catalyst through DFT calculations in a microsolvated environment considering explicit solvent and fully solvated AIMD simulations for the key elementary steps. Our computational analysis reveals a possibility of an Meerwein-Ponndorf-Verley (MPV)-type mechanism in this system, which does not involve the participation of the N-H moiety and the formation of a transition metal hydride species in ketone conversion. This path has not been considered for Mn-based metal-ligand cooperative transfer hydrogenation homogeneous catalysis before. The MPV mechanism is strongly facilitated by the solvent molecules present in the reaction environment and can potentially contribute to the catalytic performance of other related catalyst systems. Calculations indicate that despite proceeding effectively in the second coordination sphere of the transition metal metal centre, the MPV reaction path retains the enantioselectivity preference induced by the presence of the small chiral N,N'-dimethyl-1,2-cyclohexanediamine ligand within the catalytic Mn(I) complex.

6.1. Introduction

Transfer hydrogenation (TH) is a simple and robust chemical transformations that can widely be used in both asymmetric and symmetric synthesis.[1] During the reaction a hydrogen donor molecule, present in excess, donates an H_2 equivalent to reduce a polar moiety in a substrate, e.g. to transform a carbonyl to a hydroxyl group. The reaction effectively shuffles dihydrogen from one alcohol to another. To control the selectivity of these reactions and the efficiency of the catalyst, it is imperative to understand the underlying mechanism in great detail. Besides understanding and predicting reactivity of a catalyst, the knowledge of a mechanism allows chemists to make great steps in the optimization of the chemical transformation. On one hand, if the mechanism of a process is known, deactivation pathways can be analysed and strategies can be implemented to circumvent the catalyst from escaping the productive catalytic cycle.[2] On the other hand, the reactivity, substrate scope and efficiency of a process can be tuned by fine-tuning and optimizing the molecular design of the catalyst.[3, 4]

From a mechanistic perspective TH requires a catalytic scaffold which can store H_2 equivalents from the alcohol moiety, and subsequently transfer it to the ketone function of the substrate. The transfer of H_2 equivalent from alcohol can occur via a homolytic, or via a heterolytic cleavage mechanism. The homolytic mechanism is inspired from the galactose oxidase enzyme and effectively involves hydrogen atom transfer steps.[5–7] The heterolytic pathway involves the acid-base chemistry wherein a base deprotonates the hydroxyl group of the alcohol, and a Lewis acid (LA) accepts a hydride (H^-) from the C-H moiety, which together represent the H_2 equivalent. Bifunctional catalytic scaffolds (M-L) that incorporate an LA in the form of a transition metal centre (M), and an amido ligand (L), which functions as Brønsted base, have been extensively investigated for the (de)hydrogenation catalysis.[8–10]

The TH reaction can be viewed as a combination of two events, namely, the oxidation of the alcohol, and the reduction of an unsaturated group, e.g. a C=O moiety, in the substrate. In the first oxidation step the alcohol get dehydrogenated over M-L to produce the M(H)-L(H) complex. In the next reduction step a substrate with C=O function accepts the hydride from the M(H) and a proton from the L(H) to complete the TH event. Two primary mechanisms have been discussed in the literature for the TH reaction by bifunctional transition metal catalysts, namely, the concerted and step-wise mechanisms (Figure 6.1).[11–17] In the concerted mechanism the hydride and the proton transfer steps occur within the same transition state (TS), which typically features a six-membered pericyclic configuration. In contrast, in the step-wise mechanism, the L-H moiety remains protonated during the hydride transfer TSs and the protonation of the alkoxide moiety at the final stage of the catalytic cycle proceeds in a separate elementary step.

The key assumption in both mechanisms is that the ligand directly participates in the catalytic process.[18] In the concerted mechanism the ligand functions as a reversible storage of H^+. In the step-wise mechanism the L-H moiety favourably orients the alkoxide moiety, which transfers the hydride, and polarized the C=O function for a favourable hydride insertion during the reduction event. The ability to reversibly pronate and deprotonate the nitrogen centre on the ligand is dictated by its pK_a value, and it has been proposed to be a determining factor between the concerted and the step-wise mechanism.[19–23] Interestingly, the Meerwein-

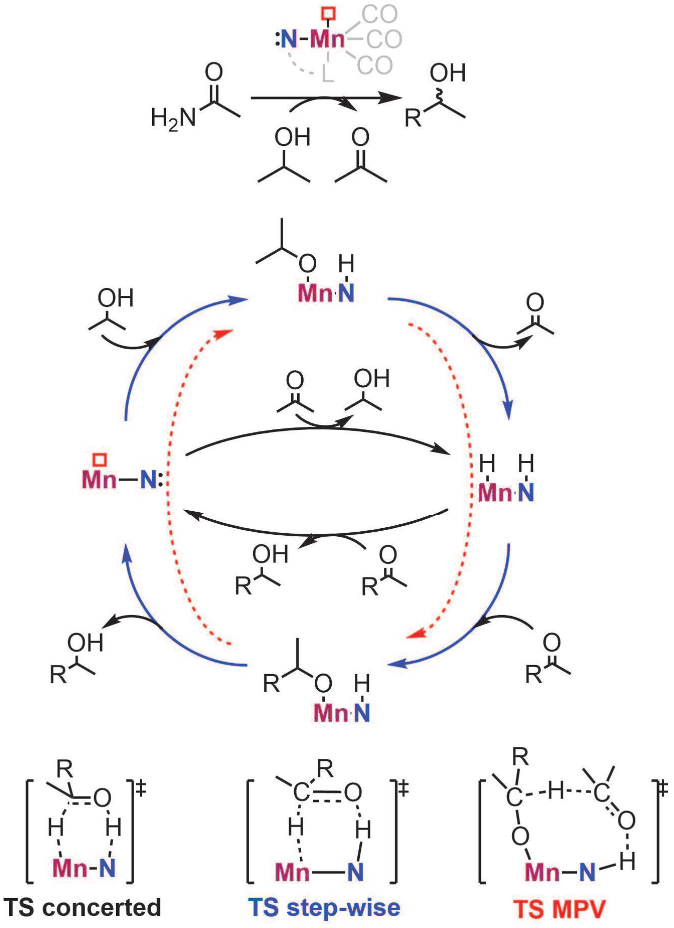

Figure 6.1: Main intermediates and transition states of a Mn-diamine catalysed ketone reduction for pathways proceeding through a concerted (black), stepwise (blue) and MPV-like (red) mechanism.

Ponndorf-Verley (MPV) mechanism, often considered for reduction reactions by metal alkoxides, has not been discussed in the literature for TH reactions catalysed by transition metal complexes.[24–27] In the MPV mechanism the proton and hydride transfer occurs directly between the reducing agent and the substrate via a cyclic TS facilitated by coordination to a LA. The MPV mechanism excludes the formation of metal hydride species, and the ligand is not expected to play any direct role. Earlier, MPV-like mechanism for the catalytic reduction of ketones has been eliminated from mechanistic considerations because of the unfavourable energetics computed for the respective cyclic transition state.[11, 13] While coordination of an alkoxide and a ketone at a metal centre can be energetically unfavourable, a solvent and ligand co-mediated possibility exists wherein the substrate is stabilized and oriented close to the metal alkoxide species via H-bonding interactions.

Improvements in computational strategies enables us to incorporate solvation effects more efficiently [21, 23, 28, 29] and reconsider mechanisms that have earlier been discarded.[30–32] Therefore, we herein reconsider the feasibility of an MPV-like mechanism for the asymmetric ketone reduction by a bifunctional Mn-diamine catalyst when explicit solvent description is applied. The cis-Mn(N,N′-dimethyl-1,2-cyclohexanediamine)$(CO)_3Br$ catalyst is chosen for this study due to its generic features, which makes it an attractive representative model system for mechanistic studies.[33]

6.2. Results and Discussion

Calculations to capture the effect of the solvent environments have been carried out with gas phase and microsolvated molecular models using density functional theory (DFT) calculations at PBE0-D3/6-311+G(d,p)//SMD level of theory, and fully explicit solvated ab initio molecular dynamics (AIMD) simulations. Our results reveal the active participation of the solvent in the transfer hydrogenation of the ketone by the Mn catalyst. Analysis of solvated intermediates from AIMD revealed that in addition to the substrate isopropanol, an additional isopropanol moiety from the solvent plays an important role in the mechanism. On the basis of the AIMD results we constructed a microsolvated model on which DFT calculations were performed for detailed and accurate analysis of the minimum energy reaction pathway (MERP). The microsolvated model included two isopropanol solvent molecules, one acting as a hydrogen donor and one merely participating by stabilizing intermediate and transition state structures. In addition continuum solvation in isopropanol using the SMD solvation model was applied. On the basis of the calculations a new catalytic pathway has been proposed presented in Figure 6.2. In the proposed pathway, the reaction starts with the active species I, in which the Mn-alkoxide (isopropoxide) complex forms a hydrogen bonded complex with the ketone substrate (acetophenone) at the N_1H-moiety of the ligand. Next, the alkoxide anion is replaced with the acetophenone from the Mn centre to form the activated species II. This steps proceeds endergonically ($\Delta G = 74$ kJ mol^{-1}) due to the energy loss associated with the formation of a separate ion pair between the isopropoxide anion and the cationic Mn complex. The isopropoxide ion is stabilized by hydrogen bonds with the N_2H-moiety and the additional isopropanol molecule (Structure II, Figure 6.2). At the next step, the hydride is transferred from the iPrO$^-$ ion to the Mn-bound acetophenone. This reaction is strongly exergonic ($\Delta G = -68$ kJ mol^{-1}) and proceeds with a barrier of only 35 kJ mol^{-1}. The hydride transfer yields acetone by-product and the alkoxide (1-phenylethoxide) complex III. An isopropanol molecule hydrogen-bonded with the N_1H-moiety (IV) next transfers its proton to the alkoxide species to form phenylethanol, which, in turn, hydrogen-bonds with the N_2H-moiety of the ligand. Simultaneously, the formed iPrO$^-$ binds with the undercoordianted Mn centre to form V and thus close the catalytic cycle. The amino-moiety on the ligand is therefore not directly participating in the key elementary steps with the exception of providing a pre-coordination handle that facilitates the reactive arrangement of the substrates in the vicinity of the Lewis acidic Mn site. A

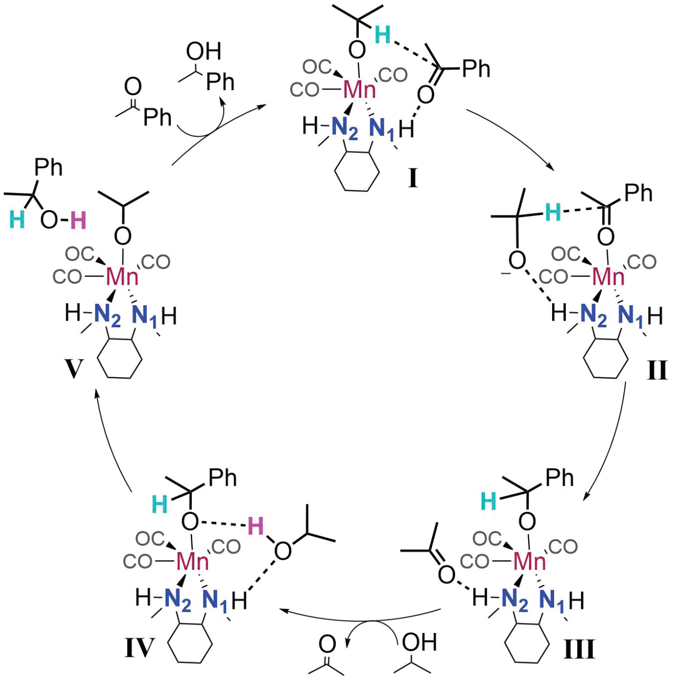

Figure 6.2: Proposed Meerwein-Ponndorf-Verley-type mechanism for ketone transfer hydrogenation by the Mn-NN catalyst facilitated by isopropanol solvent molecules.

similar solvent-assisted proton-transfer function of the cooperative ligand sites has been proposed for Noyori-type Ru hydrogenation catalysts by Dub et al.[21] Our calculations highlight the importance of the solvent participation in the catalytic carbonyl reduction by cooperative Mn(I) complexes. Most of the prior mechanistic proposals on the step-wise and concerted pathway for such systems imply that the N-H functionality is deprotonated and protonated to transfer the hydrogen equivalent. In the current mechanism, the hydrogen transfer molecule occurs directly from the solvent to the substrate. During the simulation it was verified that the N-H moiety stays protonated throughout the reaction pathway. A similar effect has been observed before for the (de)protonation steps in the reduction paths over Ru-H catalytic species.[29, 32] While the NH-functionality of the ligand backbone is not directly involved and stays protonated during the hydride transfer, it plays a crucial role in aligning the substrates to enable the hydride transfer. The stabilizing influence of the solvent environment for the rate-determining hydride transfer step (II - III) becomes apparent when the energetics computed with different models, namely, the gas phase, implicit solvation, and explicit (micro)solvation are compared (Figure 6.3). The Gibbs free energy of activation for the transformation of II to III is the highest in the gas phase (58 kJ mol^{-1}), followed by the implicit solvation model (44 kJ mol^{-1}), and the microsolvation model (35 kJ mol^{-1}). Thus, introduction of implicit solvation stabilizes the TS by 14 kJ mol^{-1}. The inclusion of microsolvation via an additional isopropanol molecule further reduced the barrier by 9 kJ mol^{-1}. Our previous computational studies showed that the one-step ketone reduction by Mn-H species (Figure 6.1) proceed with the barriers in the range

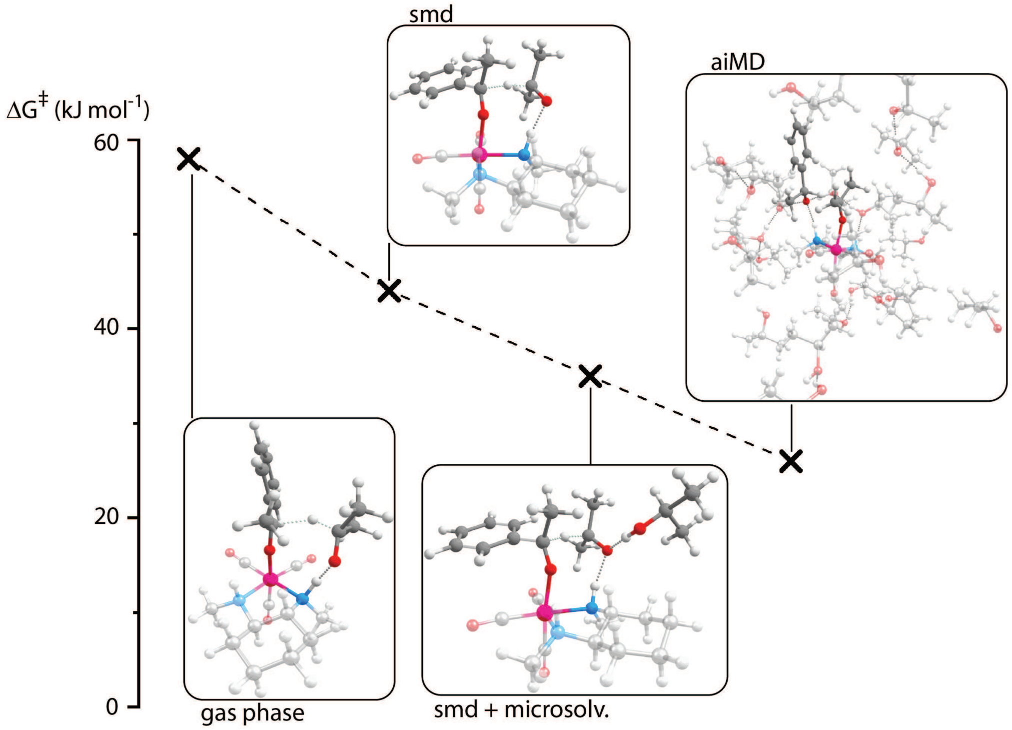

Figure 6.3: Gibbs free energy barriers and transition states structures of hydride transfer from II – III in the gas phase model, implicit SMD solvation model, a microsolvated model incorporating SMD solvation with an explicit isopropanol solvent molecule and AIMD model. Energies in kJ mol^{-1}.

70 – 80 kJ mol^{-1}.[33, 34] This suggests that the current solvent-assisted MPV-type outer-sphere reduction by Mn-alkoxide complexes can represent a viable competitive mechanism. This is in line with the observation that the Mn-hydride species were not identified for the current Mn-N,N system, which also does promote the direct hydrogenation of ketones with H_2. The effect of the explicit solvent on the

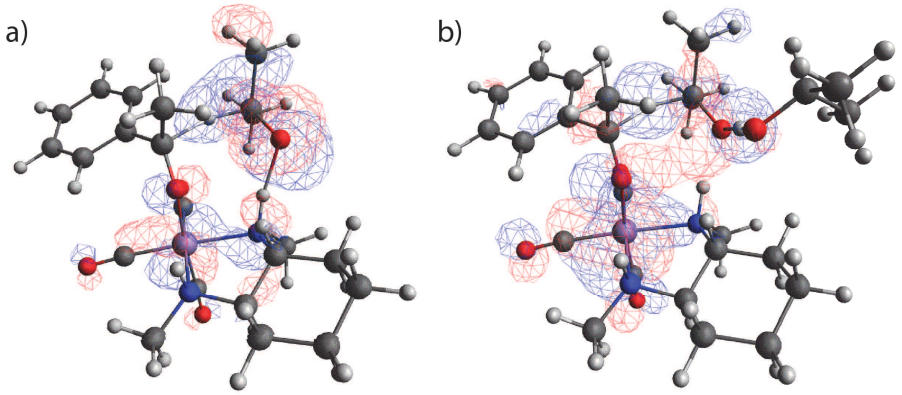

Figure 6.4: Highest occupied molecular orbitals of $TS_{\text{II-III}}$ a) in an implicit solvation SMD model and b) microsolvation model.

hydride-transfer step is observed when visualizing the highest occupied molecular orbitals (HOMOs) in the transition state structures. Figure 6.4 compares the HOMO of the TS computed in the implicit solvation (Figure 6.4a) and microsolvation (Figure 6.4b) models. The HOMO is substantially localized on the amine moiety in the former case. In the presence of an additional solvent molecules in the microsolvated model (Figure 6.4b), the OH moiety of the solvent isopropanol contributes to the HOMO instead. This indicates the stabilization of the charge density through the hydrogen bond offered by the isopropanol molecule.

To proceed with the catalytic cycle from state III, the acetone molecule is replaced by another isopropanol solvent molecule that forms a hydrogen bond with the NH-moiety (IV) of the Mn-catalyst. This is followed by a proton transfer from the isopropanol molecule to the Mn-alkoxide to yield phenylethanol. The coformed isopropoxide anion coordinates to the metal centre to form the starting alkoxide species (I).

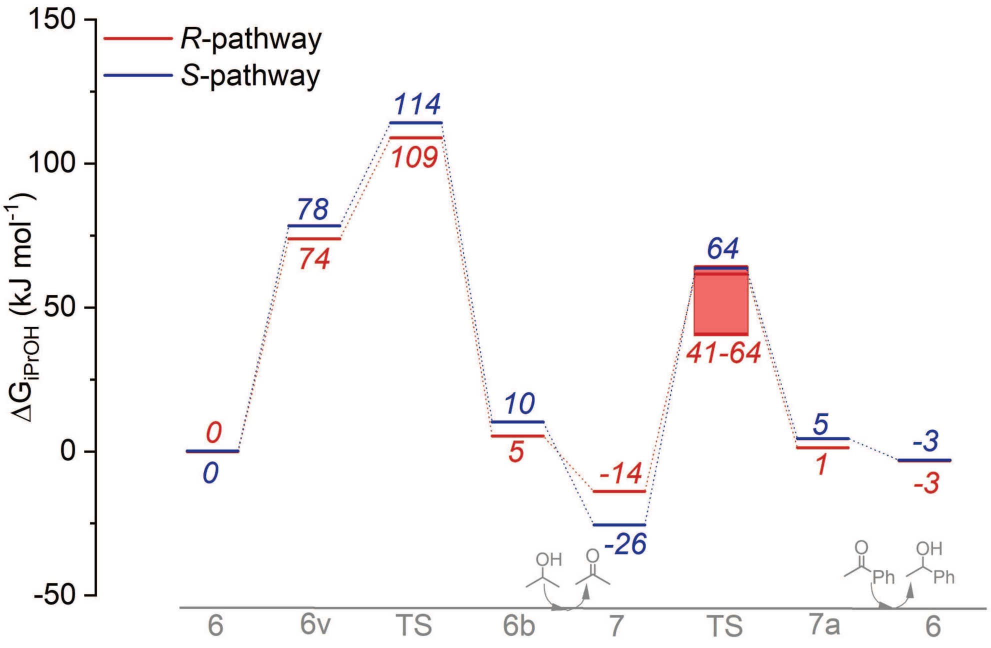

Figure 6.5: Reaction Gibbs free energy diagram for the reduction of acetophenone to *R*- and *S*-1-phenylethanol (red and blue) in the microsolvation model.

The complete reaction path for this mechanism was computed for both *R* and *S* enantiomers and the resulting reaction Gibbs free energy diagram is shown in Figure 6.5. The optimized geometries of all intermediates and transition states towards the formation of *R*-1-phenyletahnol are presented in Figure 6.6. Note that locating the transition state of intermediate IV*R* to V*R* was challenging because of the very shallow potential energy surface obtained with the SMD implicit solvation model. An ensemble of transition state-like structures have been identified, as indicated in the figure. The solvent environment plays a crucial role in this step. The transferred proton stems from one of the isopropanol molecules in the environment leading to a shallow energy surfaces. Since isopropanol is the main component of the system, this proton transfer process should be feasible in a real solvent environment. The recovery of the initial catalyst state is an endergonic process, in which the formed product of phenylethanol is replaced by an isopropanol molecule (V - I). The more facile reduction of acetophenone to *R*-penylethanol compared to its stereoisomer indicates that the asymmetric ligand backbone is able to induce chirality in the MPV mechanism. Our calculations reveal that the enantioselectivity-determining transition state (TS$_{\text{II-III}}$) is at the same time the highest energy barrier in overall catalytic process. The NH-moiety of the ligand still acts cooperatively with the reactive Mn Lewis acidic site. The NH site aids in directing the proton- and hydride-donor molecules to facilitate their reactions along the catalytic mechanism. The difference between the formation of the *R*- and *S*-enantiomers is 5 kJ mol^{-1}, which corresponds to an enantiomeric excess to above 70% and is in line with the experimentally reported value for this system.[33] Both cooperative NH-sites have been examined to allow the location of the MERP. Furthermore, we estimated the pK$_a$ for both N-H sites using DFT calculations. Estimated pK$_a$ 40 (in tetrahydrofuran) is consistent with our mechanistic finding that the N-H moiety remains protonated throughout the computed MERP. To investigate the explicit role of the solvent in the hydrogenation reaction we also performed ab initio molecular dynamics (AIMD) simulations with one explicit isopropanol solvent molecule, for both the *R* and *S* enantiomers formation. We considered a one-step hydride transfer pathway from an iPrO adduct to an acetophenone moiety in the solvent phase. The difference in C-H bond length of the donor and acceptor C moieties was considered as the reaction coordinate (Figure 6.7). Q < 0 corresponded to a "reactant-like" state of the system while Q > 0 represented a "product-like" state.

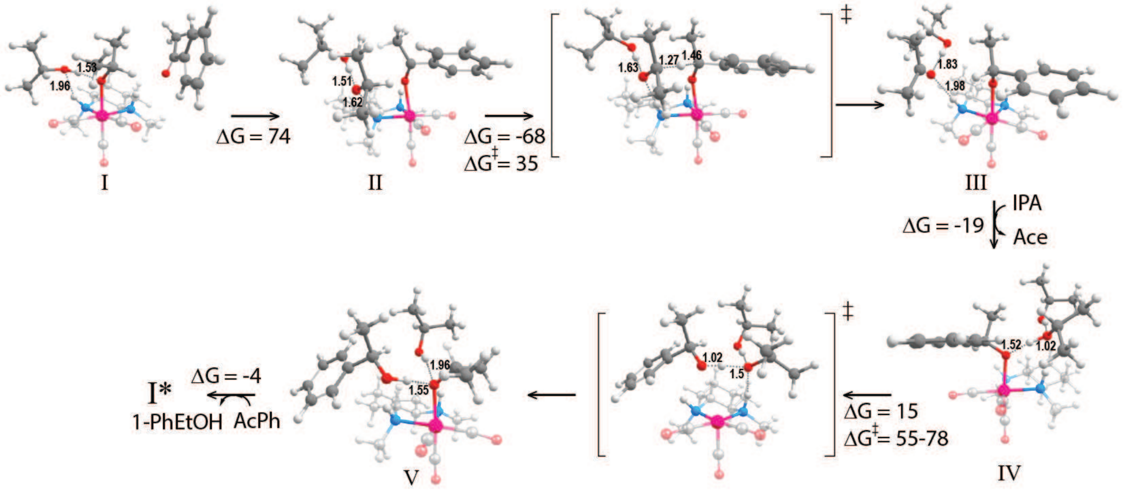

Figure 6.6: Structures of reaction intermediates and transition states of the MERP for the reduction of acetophenone to *R*-phenylethanol. Gibbs free energies in kJ mol^{-1}, bond distances in Å.

Constrained AIMD simulations were performed for several fixed values of Q (10 values between -2.26 Å ≤ Q ≤ 0.64 Å for *R*, and 10 values between -2.36 Å ≤ Q

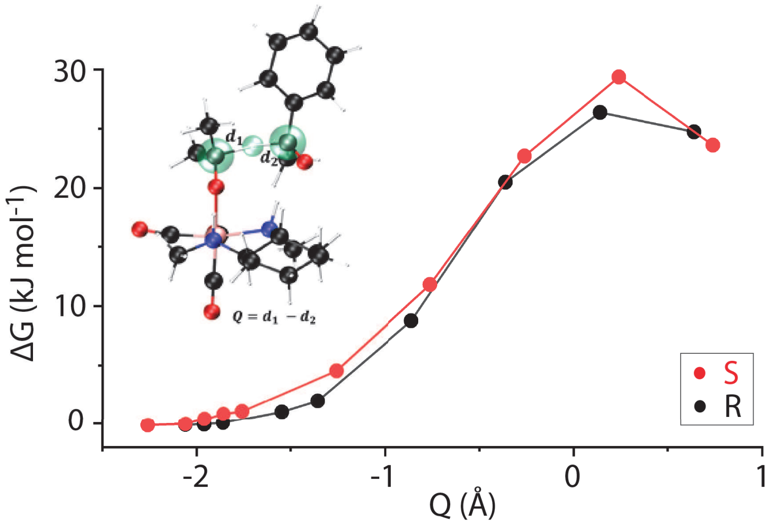

Figure 6.7: Gibbs free energy profiles for transfer of hydride from iPrO adducts to a solvated acetophenone moiety along the *S* and *R* pathways. Depiction of the reaction coordinate (Q) for hydride transfer in AIMD simulations displayed in the left corner. The C and H atoms directly involved in Q highlighted in green.

≤ 0.74 Å for *S*). The resulting Gibbs free energy profiles are shown in Figure 6.8. The hydride transfer was found to proceed with a free energy barrier of 29 kJ mol^{-1} for the *S* pathway, and 26 kJ mol^{-1} for the *R* pathway. Consistent with DFT computed MERP the *R*-pathway is found to proceed with a slightly lower barrier. Analysis of geometries close to the TS revealed that steric hindrance in the *S* isomer leads to less H-bind stabilization of the O moiety in acetophenone than the *R* isomer (Figure 6.8). This leads to lower barrier for the TS in the *R* isomer. Furthermore, analysis of AIMD computed trajectories showed that the N-H moiety stayed protonated during the hydride transfer reaction which is consistent with the DFT computed mechanism.

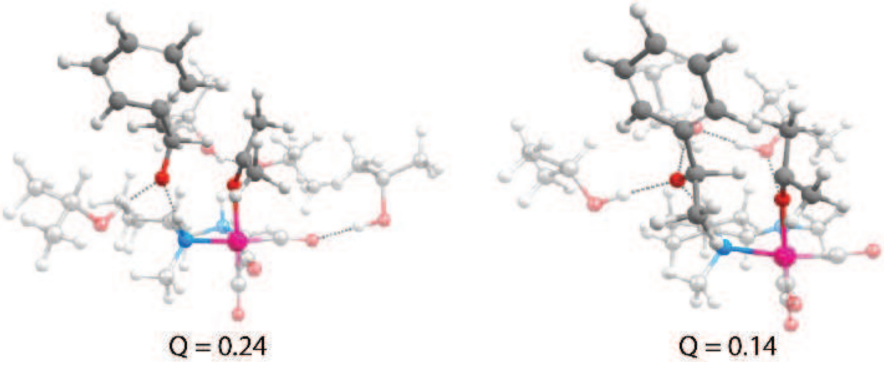

Figure 6.8: Snapshots of solvated geometries close to the transition state for (left) *S* and (right) *R* isomers. The AIMD model inspired the placement of solvent for DFT calculations.

We also show here that for the current catalytic system, the alkoxide can represent the catalytically active species in ketone transfer hydrogenation instead of being a resting state.[33, 35] In the alternative direct H2 hydrogenation reactions, the stable alkoxide adducts are often considered resting states, which explains the limited reactivity of the current and related Mn-diamine catalysts.

6.3. Conclusion

In this work, we have shown that an MPV-type mechanism can be feasible for the transfer hydrogenation of ketones by a bifunctional homogenous transition metal catalyst by computationally considering a representative example of Mn(I)-NN bidentate catalyst. Contrary to the conventionally proposed Mn-mediated hydride transfer mechanisms, the reduction of the ketone substrate by an Mn-alkoxide adduct proceeds via a direct hydride shift. The Mn centre acts as a Lewis acid polarizing the substrate and stabilizing the anionic intermediates. The N-H functionality of the bifunctional catalyst remains intact in the course of the reaction, while it facilitates the reduction reaction by directing the coordination of the substrate. Importantly, the ligand is not deprotonated during the catalytic reaction and therefore not directly involved in the reduction. Our DFT and AIMD calculations have shown that the N-H moiety serves as a supramolecular directing group that ensures positioning reactants in a proper orientation by H-bonding. The ketone is instead directly hydrogenated by the isopropanol solvent. The role of the solvent description is crucial as including solvation lowers the transition state barrier significantly. This work shows that unlike our earlier work suggests the alkoxide species can be the active species. The retention of the N-H bond is also possible in reductions with small molecules acting as hydrogen donor. The inclusion of additional solvent molecules in the theoretical description of the catalytic system is crucial for the feasibility of the mechanism.

6.4. Computational Details

All density functional theory (DFT) calculations were performed using the Gaussian16 C0.1 program.[36] The hybrid exchange-correlation functional PBE0[37] was used in combination with the 6-311+G(d,p) basis set on all atoms for geometry optimization and vibrational analysis. Van der Waals interactions are accounted for by the dispersion-corrected DFT-D3 (BJ) method.[38] The ultrafine grid was uniformly used. The nature of each stationary point was confirmed by frequency analysis, in which zero imaginary frequencies for minima and one for transition states. Gibbs free energies (ΔG) were calculated at a temperature of 333.15 K with a SMD solvent correction for isopropanol.[39] An ultrafine grid was uniformly used.

DFT-based Born Oppenheimer molecular dynamics were performed employing the CP2K package,[40] and using the BLYP functional[41, 42] supplemented by D3 dispersion corrections.[43] The system consisted of complexes I-*R*/I-*S* with 22 iPrOH molecules in a periodic cubic box (L=15 Å). A time step of 1.0 fs was used in our simulations. The temperature was controlled by a CSVR thermostat[44] and set at T = 360 K. Goedecker–Teter–Hutter (GTH) pseudopotentials were employed to account for the interactions of the nuclei and core electrons with the valence electrons. The electronic states were expanded using a DZV-GTH-PADE basis set for Manganese, and a TZVP-GTH basis set for all other atom types. The auxiliary plane waves were expanded up to 280 Ry. We used the constrained molecular dynamics method,[42, 45] to determine the Gibbs free energy profile where using a chosen reaction coordinate, Q, simulations were performed at several fixed values of Q. The free energy change upon changing from Q1 to Q2 is then computed according to the equation below. Here, <*F(Q)*> is the average constraint force measured for each value of Q. For each value of the reaction coordinate 15-20 ps of runs were performed. The average force was computed over the last 5 ps of production run.

$$\Delta G_{Q_1 \rightarrow Q_2} = -\int_{Q1}^{Q2} < F(Q) > \, dQ$$

Author's note

Alternative configurations have not been published in this chapter. In principle, to arrive at all possible intermediate and transition state structure, a more thorough configurational search is required. This has been carried out in the aiMD simulations but was not extended to the DFT calculations.

References

[1] R. Noyori, *Asymmetric Catalysis: Science and Oppurtunities,* Nobel Lect. , 186 (2001).

[2] R. H. Crabtree, *Deactivation in Homogeneous Transition Metal Catalysis: Causes, Avoidance, and Cure,* Chem. Rev. **115**, 127 (2015).

[3] C. Li, Y. Pan, Y. Feng, Y.-M. He, Y. Liu, and Q.-H. Fan, *Asymmetric Ruthenium-Catalyzed Hydrogenation of Terpyridine-Type N -Heteroarenes: Direct Access to Chiral Tridentate Nitrogen Ligands,* Org. Lett. **22**, 6452 (2020).

[4] J. Mahatthananchai, A. M. Dumas, and J. W. Bode, *Catalytic Selective Synthesis,* Angew. Chemie Int. Ed. **51**, 10954 (2012).

[5] D. Yin, S. Urresti, M. Lafond, E. M. Johnston, F. Derikvand, L. Ciano, J.-G. Berrin, B. Henrissat, P. H. Walton, G. J. Davies, and H. Brumer, *Structure–function characterization reveals new catalytic diversity in the galactose oxidase and glyoxal oxidase family,* Nat. Commun. **6**, 10197 (2015).

[6] F. Himo, L. A. Eriksson, F. Maseras, and P. E. M. Siegbahn, *Catalytic Mechanism of Galactose Oxidase: A Theoretical Study,* J. Am. Chem. Soc. **122**, 8031 (2000).

[7] N. Donati, M. Königsmann, D. Stein, L. Udino, and H. Grützmacher, *Iridium aminyl radical complexes as catalysts for the catalytic dehydrogenation of primary hydroxyl functions in natural products,* Comptes Rendus Chim. **10**, 721 (2007).

[8] O. Martínez-Ferraté, C. Werlé, G. Franciò, and W. Leitner, *Aminotriazole Mn(I) Complexes as Effective Catalysts for Transfer Hydrogenation of Ketones,* ChemCatChem **10**, 4514 (2018).

[9] A. Bruneau-Voisine, D. Wang, V. Dorcet, T. Roisnel, C. Darcel, and J.-B. Sortais, *Transfer Hydrogenation of Carbonyl Derivatives Catalyzed by an Inexpensive Phosphine-Free Manganese Precatalyst,* Org. Lett. **19**, 3656 (2017).

[10] K. Z. Demmans, M. E. Olson, and R. H. Morris, *Asymmetric Transfer Hydrogenation of Ketones with Well-Defined Manganese(I) PNN and PNNP Complexes,* Organometallics **37**, 4608 (2018).

[11] D. A. Alonso, P. Brandt, S. J. M. Nordin, and P. G. Andersson, *Ru(arene)(amino alcohol)-Catalyzed Transfer Hydrogenation of Ketones: Mechanism and Origin of Enantioselectivity,* J. Am. Chem. Soc. **121**, 9580 (1999).

[12] K.-J. Haack, S. Hashiguchi, A. Fujii, T. Ikariya, and R. Noyori, *The Catalyst Precursor, Catalyst, and Intermediate in the RuII-Promoted Asymmetric Hydrogen Transfer between Alcohols and Ketones,* Angew. Chemie Int. Ed. English **36**, 285 (1997).

[13] M. Yamakawa, H. Ito, and R. Noyori, *The Metal–Ligand Bifunctional Catalysis: A Theoretical Study on the Ruthenium(II)-Catalyzed Hydrogen Transfer between Alcohols and Carbonyl Compounds,* J. Am. Chem. Soc. **122**, 1466 (2000).

[14] C. P. Casey, S. W. Singer, D. R. Powell, R. K. Hayashi, and M. Kavana, *Hydrogen Transfer to Carbonyls and Imines from a Hydroxycyclopentadienyl Ruthenium Hydride: Evidence for Concerted Hydride and Proton Transfer,* J. Am. Chem. Soc. **123**, 1090 (2001).

[15] T. Higashi, S. Kusumoto, and K. Nozaki, *Cleavage of Si–H, B–H, and C–H Bonds by Metal–Ligand Cooperation,* Chem. Rev. **119**, 10393 (2019).

[16] C. P. Casey and J. B. Johnson, *Kinetic Isotope Effect Evidence for a Concerted Hydrogen Transfer Mechanism in Transfer Hydrogenations Catalyzed by [p -(Me 2 CH)C 6 H 4 Me]Ru- (NHCHPhCHPhNSO 2 C 6 H 4 - p- CH 3),* J. Org. Chem. **68**, 1998 (2003).

[17] R. Noyori, M. Yamakawa, and S. Hashiguchi, *Metal–Ligand Bifunctional Catalysis: A Nonclassical Mechanism for Asymmetric Hydrogen Transfer between Alcohols and Carbonyl Compounds,* J. Org. Chem. **66**, 7931 (2001).

[18] P. A. Dub and J. C. Gordon, *The role of the metal-bound N–H functionality in Noyori-type molecular catalysts,* Nat. Rev. Chem. **2**, 396 (2018).

[19] N. Govindarajan, H. Beks, and E. J. Meijer, *Variability of Ligand pKa during Homogeneously Catalyzed Aqueous Methanol Dehydrogenation,* ACS Catal. **10**, 14775 (2020).

[20] P. A. Dub and J. C. Gordon, *The mechanism of enantioselective ketone reduction with Noyori and Noyori–Ikariya bifunctional catalysts,* Dalt. Trans. **45**, 6756 (2016).

[21] P. A. Dub, N. J. Henson, R. L. Martin, and J. C. Gordon, *Unravelling the Mechanism of the Asymmetric Hydrogenation of Acetophenone by [RuX 2 (diphosphine)(1,2-diamine)] Catalysts,* J. Am. Chem. Soc. **136**, 3505 (2014).

[22] P. A. Dub, B. L. Scott, and J. C. Gordon, *Why Does Alkylation of the N–H Functionality within M/NH Bifunctional Noyori-Type Catalysts Lead to Turnover?* J. Am. Chem. Soc. **139**, 1245 (2017).

[23] P. A. Dub and T. Ikariya, *Quantum Chemical Calculations with the Inclusion of Nonspecific and Specific Solvation: Asymmetric Transfer Hydrogenation with Bifunctional Ruthenium Catalysts,* J. Am. Chem. Soc. **135**, 2604 (2013).

[24] L. Zheng, X. Yin, A. Mohammadlou, R. P. Sullivan, Y. Guan, R. Staples, and W. D. Wulff, *Asymmetric Catalytic Meerwein–Ponndorf–Verley Reduction of Ketones with Aluminum(III)-VANOL Catalysts,* ACS Catal. **10**, 7188 (2020).

[25] J. Song, M. Hua, X. Huang, A. Visa, T. Wu, H. Fan, M. Hou, Z. Zhang, and B. Han, *Highly efficient Meerwein–Ponndorf–Verley reductions over a robust zirconium-organoboronic acid hybrid,* Green Chem. **23**, 1259 (2021).

[26] C. G. Screttas and C. T. Cazianis, *Mechanism of meerwein-pondorf-verley type reductions,* Tetrahedron **34**, 933 (1978).

[27] G. Zassinovich, G. Mestroni, and S. Gladiali, *Asymmetric hydrogen transfer reactions promoted by homogeneous transition metal catalysts,* Chem. Rev. **92**, 1051 (1992).

[28] J.-W. Handgraaf and E. J. Meijer, *Realistic Modeling of Ruthenium-Catalyzed Transfer Hydrogenation,* J. Am. Chem. Soc. **129**, 3099 (2007).

[29] A. Pavlova and E. J. Meijer, *Understanding the Role of Water in Aqueous Ruthenium-Catalyzed Transfer Hydrogenation of Ketones.* ChemPhysChem **13**, 3492 (2012).

[30] N. Govindarajan and E. J. Meijer, *Modeling the Catalyst Activation Step in a Metal–Ligand Radical Mechanism Based Water Oxidation System,* Inorganics **7**, 62 (2019).

[31] N. Govindarajan, V. Sinha, M. Trincado, H. Grützmacher, E. J. Meijer, and B. Bruin, *An In-Depth Mechanistic Study of Ru-Catalysed Aqueous Methanol Dehydrogenation and Prospects for Future Catalyst Design,* ChemCatChem **12**, 2610 (2020).

[32] V. Sinha, N. Govindarajan, B. de Bruin, and E. J. Meijer, *How Solvent Affects C–H Activation and Hydrogen Production Pathways in Homogeneous Ru-Catalyzed Methanol Dehydrogenation Reactions,* ACS Catal. **8**, 6908 (2018).

[33] R. van Putten, G. A. Filonenko, A. Gonzalez de Castro, C. Liu, M. Weber, C. Müller, L. Lefort, and E. Pidko, *Mechanistic Complexity of Asymmetric Transfer Hydrogenation with Simple Mn–Diamine Catalysts,* Organometallics **38**, 3187 (2019).

[34] A. M. Krieger and E. A. Pidko, *The Impact of Computational Uncertainties on the Enantioselectivity Predictions: A Microkinetic Modeling of Ketone Transfer Hydrogenation with a Noyori-type Mn-diamine Catalyst,* ChemCatChem **13**, 3517 (2021).

[35] A. M. Krieger, P. Kuliaev, F. Q. Armstrong Hall, D. Sun, and E. A. Pidko, *Composition- and Condition-Dependent Kinetics of Homogeneous Ester Hydrogenation by a Mn-Based Catalyst,* J. Phys. Chem. C **124**, 26990 (2020).

[36] M. J. Frisch, G. W. Trucks, H. B. Schlegel, G. E. Scuseria, M. A. Robb, J. R. Cheeseman, G. Scalmani, V. Barone, G. A. Petersson, H. Nakatsuji, X. Li, M. Caricato, A. V. Marenich, J. Bloino, B. G. Janesko, R. Gomperts, B. Mennucci, H. P. Hratchian, J. V. Ortiz, A. F. Izmaylov, J. L. Sonnenberg, D. Williams-Young, F. Ding, F. Lipparini, F. Egidi, J. Goings, B. Peng, A. Petrone, T. Henderson, D. Ranasinghe, V. G. Zakrzewski, J. Gao, N. Rega, G. Zheng, W. Liang, M. Hada, M. Ehara, K. Toyota, R. Fukuda, J. Hasegawa, M. Ishida, T. Nakajima, Y. Honda, O. Kitao, H. Nakai, T. Vreven, K. Throssell, J. A. Montgomery Jr., J. E. Peralta, F. Ogliaro, M. J. Bearpark, J. J. Heyd, E. N. Brothers, K. N. Kudin, V. N. Staroverov, T. A. Keith, R. Kobayashi, J. Normand, K. Raghavachari, A. P. Rendell, J. C. Burant, S. S. Iyengar, J. Tomasi, M. Cossi, J. M. Millam, M. Klene, C. Adamo, R. Cammi, J. W. Ochterski, R. L. Martin, K. Morokuma, O. Farkas, J. B. Foresman, and D. J. Fox, *Gaussian16 Revision C.01,* (2016).

[37] C. Adamo and V. Barone, *Toward reliable density functional methods without adjustable parameters: The PBE0 model,* J. Chem. Phys. **110**, 6158 (1999).

[38] E. Caldeweyher, C. Bannwarth, and S. Grimme, *Extension of the D3 dispersion coefficient model,* J. Chem. Phys. **147**, 034112 (2017).

[39] A. V. Marenich, C. J. Cramer, and D. G. Truhlar, *Universal Solvation Model Based on Solute Electron Density and on a Continuum Model of the Solvent Defined by the Bulk Dielectric Constant and Atomic Surface Tensions,* J. Phys. Chem. B **113**, 6378 (2009).

[40] J. VandeVondele, M. Krack, F. Mohamed, M. Parrinello, T. Chassaing, and J. Hutter, *Quickstep: Fast and accurate density functional calculations using a mixed Gaussian and plane waves approach,* Comput. Phys. Commun. **167**, 103 (2005).

[41] A. D. Becke, *Density-functional exchange-energy approximation with correct asymptotic behavior,* Phys. Rev. A **38**, 3098 (1988).

[42] E. Carter, G. Ciccotti, J. T. Hynes, and R. Kapral, *Constrained reaction coordinate dynamics for the simulation of rare events,* Chem. Phys. Lett. **156**, 472 (1989).

[43] S. Grimme, J. Antony, S. Ehrlich, and H. Krieg, *A consistent and accurate ab initio parametrization of density functional dispersion correction (DFT-D) for the 94 elements H-Pu,* J. Chem. Phys. **132**, 154104 (2010).

[44] G. Bussi, D. Donadio, and M. Parrinello, *Canonical sampling through velocity rescaling,* J. Chem. Phys. **126**, 014101 (2007).

[45] M. Sprik and G. Ciccotti, *Free energy from constrained molecular dynamics,* J. Chem. Phys. **109**, 7737 (1998).

Summary

Catalysts are an important component of our daily life. Therefore, it is important that the catalysts we apply in industrial processes are the most efficient and sustainable they can be. The design of catalytic systems has been a field of trial-and-error, incrementally improving the system over time. Computational methods enable us to build models that predict catalytic properties. This thesis is dedicated to exploring how computational simulations and models can be applied in homogeneous catalysis. The focus lies on homogeneous catalytic systems incorporating manganese. The development and history of manganese-containing catalytic systems is elucidated in detail in Chapter 1.

In Chapter 2 we describe the computational methods that have been applied to study the catalytic systems. Quantum chemical calculations form the basis of this thesis as they were applied to estimates the energy and geometry of our catalytic systems. Density functional theory is still the golden standard in the field as it gives the most accurate description of the system at a reasonable computational cost. However, also methods like Density functional tight binding are more widely employed as they computational time required to carry out the calculations is significantly reduced. The solvent models that are applied in calculations can vary from continuum solvent models that are applied directly during the DFT calculations or solvent description that are added later by software tools like the conductor-like screening model for realistic solutions (COSMO-RS). Both methods have been applied and compared throughout this thesis. Molecular dynamics (MD) and microkinetic modelling (MKM) were also discussed in detail as approaches to study the conformations and energetics found during the DFT calculations.

Chapter 3 focusses on the description of the reaction medium and conditions to study the ester hydrogenation by a Mn-P,N catalyst. Here, a comparison between “state-of-the-art” solvent description by continuum or gas phase models and a more detailed description by COSMO-RS was made. An important feature of the study was the description of a changing solvent model. During the reduction of ester to alcohol the solvent environment becomes more polar. This ultimately affects the energetics of the intermediates and transition states of the catalytic systems. Our study has shown that the changing reaction environment does affect kinetic properties as well as thermodynamic ones. The rate-determining step of the reaction depends on the solvent description used and also changes as a function of conversion. Therefore, we have shown that a detailed description of solvent systems is required to investigate microscopic characteristics.

In Chapter 4 we implemented a high-throughput approach to estimate the energetics of more than 700 catalytic intermediates based on manganese pincer systems. In this study DFTB was applied to analyse linear scaling relationship. We explored in more detail how DFTB calculations compare with results from DFT calculations. The catalytic systems were based on four ligand scaffolds that were functionalized at different sites of the backbone. Both the first and second coordination sphere of the catalytic system have been analysed. This data-augmented approach has shown to be an effective screening method to explore opportunities in the design of catalytic systems.

Chapter 5 looks at the mechanistic description of ketone reduction by the bifunctional manganese diamine catalyst. Literature on mechanisms of catalytic systems usually links the difference in energy barriers of the enatiodeterminitive steps to the enantiomeric excess that is produced in the reaction. In this study we show how the uncertainty in computed energetics influences the predicted selectivity. The study highlights that microkinetic modelling is an important tool when formulating conclusions on the behaviour of a catalytic system. Furthermore, we have shown that also non-enatiodeterminitive steps contribute to the selectivity of the system.

In Chapter 6 the mechanism of the transfer hydrogenation catalyst has been investigated in more detail. The established Noyori-type mechanism has been established through DFT calculations conducted with either gas phase or continuum solvent models. In our investigation we examined the influence of explicit solvent molecules on mechanistic considerations. An alternative mechanism with an innocent ligand backbone has been proposed for the reduction by a Mn-diamine catalyst. The mechanism resembles that of a Meerwein-Ponndorf-Verley reaction with the metal and N-H moieties of the catalyst coordinating the substrate and solvent. Our investigation was confirmed by MD simulations.

Our work shows the possibilities of multiscale modelling in catalysis. While conventional modelling approaches are largely based on DFT calculations, additional calculations can provide valuable insights. Especially numerical methods like microkinetic modelling are cost and time efficient and enable a direct comparison between theoretical output and data from the experiment. Therefore, conclusions on rate-determing steps or enantioselectivity should be backed by MKM. While computational methods are not perfect, they are continuously improving. The pace at which computers are evolving allows us to conduct more detailed investigations and investigate models that are more realistic. We need to embrace the development and keep questioning the insights we gained in the past. This thesis has shown that the level at which a computational study is carried out can determine the conclusions that we draw. More sophisticated models provide more detailed and multi-faceted insights. Data augmented approaches also provide possibilities to analyse catalytic systems from a more generalist viewpoint. The theoretical investigation of larger numbers of catalytic intermediates provides possibilities to find activity descriptors and drive rational design of catalytic systems.

Samenvatting

Katalysatoren zijn een belangrijk onderdeel van ons dagelijks leven. Daarom is het belangrijk dat de katalysatoren die we in industriële processen toepassen zo efficiënt en duurzaam mogelijk zijn. Het ontwerp van katalytische systemen verloopt vaak door vallen en opstaan, waarbij het systeem in de loop van de tijd stapsgewijs is verbeterd. Berekeningen stellen ons in staat om modellen te bouwen die katalytische eigenschappen voorspellen. Dit proefschrift is gewijd aan het onderzoeken van hoe simulaties en modellen kunnen worden toegepast in homogene katalyse. De focus ligt op homogene katalytische systemen, waarin mangaan is verwerkt. De ontwikkeling en geschiedenis van mangaan bevattende katalytische systemen wordt in detail toegelicht in Hoofdstuk 1.

In Hoofdstuk 2 beschrijven we de rekenmethoden die zijn toegepast om de katalytische systemen te bestuderen. Kwantumchemische berekeningen vormen de basis van dit proefschrift, omdat ze werden toegepast om de energie en geometrie van onze katalytische systemen te voorspellen. Dichtheidsfunctionaaltheorie is nog steeds de gouden standaard in het veld, omdat het de meest nauwkeurige beschrijving van het systeem geeft. Echter, ook methoden zoals Dichtheidsfunctionaalsterke binding (DFTB) worden op grotere schaal gebruikt, omdat de rekentijd die nodig is om de berekeningen uit te voeren aanzienlijk wordt verminderd. De oplosmiddelmodellen die worden toegepast in berekeningen kunnen variëren van continuüm oplosmiddelmodellen die direct worden toegepast tijdens de DFT-berekeningen of oplosmiddelbeschrijvingen die later worden toegevoegd door softwaretools zoals het conducteur-achtige screeningmodel voor realistische oplossingen (COSMO-RS). Beide methoden zijn in dit proefschrift toegepast en vergeleken. Moleculaire dynamica (MD) en microkinetische modellen (MKM) worden ook in detail besproken, om de conformaties en energieën van de DFT-berekeningen verder te bestuderen.

Hoofdstuk 3 richt zich op de beschrijving van het reactiemedium en bestudeert het belang van de omstandigheden tijdens de ester-hydrogenering door een Mn-P,N-katalysator. Hier werd een vergelijking gemaakt tussen de ”gebruikelijke” oplosmiddelbeschrijving door continuüm- of gasfasemodellen en een meer gedetailleerde beschrijving door COSMO-RS. Een belangrijk kenmerk van het onderzoek was de beschrijving met een veranderend oplosmiddelmodel. Tijdens de reductie van ester tot alcohol wordt de omgeving van het oplosmiddel meer polair. Dit beïnvloedt uiteindelijk de energie van de tussenproducten en overgangstoestanden van de katalytische systemen. Onze studie heeft aangetoond dat de veranderende reactieomgeving zowel kinetische als thermodynamische eigenschappen beïnvloedt. De snelheidsbepalende stap van de reactie hangt af van de gebruikte oplosmiddelbeschrijving en verandert ook als functie van de omzetting. Daarom hebben we aangetoond dat een gedetailleerde beschrijving van oplosmiddelsystemen nodig is om microscopische eigenschappen te onderzoeken.

In Hoofdstuk 4 hebben we een hoog-productie benadering geïmplementeerd om de energie van meer dan 700 katalytische tussenproducten te schatten op basis van mangaantangsystemen. In deze studie werd DFTB toegepast om de lineaire schaalrelatie te analyseren. We hebben in detail onderzocht hoe DFTB-berekeningen zich verhouden tot resultaten van DFT-berekeningen. De katalytische systemen waren gebaseerd op vier ligandsjablonen die op verschillende plaatsen van de ruggengraat werden aangepast. Zowel de eerste als de tweede coördinatiesfeer van het katalytische systeem zijn geanalyseerd. Deze data-aangevulde benadering is een effectieve screeningmethode om mogelijkheden in het ontwerp van katalytische systemen te onderzoeken.

Hoofdstuk 5 kijkt naar de mechanistische beschrijving van ketonenreductie door de bifunctionele mangaandiamine katalysator. Literatuur over mechanismen van katalytische systemen koppelt gewoonlijk het verschil in energiebarrières van de enantiodeterminatieve stappen aan de enantiomere overmaat die in de reactie wordt geproduceerd. In deze studie laten we zien hoe de onzekerheid in berekende energie de voorspelde selectiviteit beïnvloedt. De studie benadrukt dat microkinetische modellen een belangrijk hulpmiddel zijn bij het trekken van conclusies over het gedrag van een katalytisch systeem. Verder hebben we laten zien dat ook eerder minder belangrijk geachte stappen bijdragen aan de selectiviteit van het systeem.

In Hoofdstuk 6 is het mechanisme van de transfer-hydrogenerings katalysator in meer detail onderzocht. Het gevestigde mechanisme van het Noyori-type is tot stand gekomen door middel van DFT-berekeningen die zijn uitgevoerd met ofwel gasfase- of continuüm-oplosmiddelmodellen. In ons onderzoek hebben we de invloed van expliciete oplosmiddelmoleculen op mechanistische overwegingen onderzocht. Een alternatief mechanisme met een niet-coöperatieve ligandstructuur is voorgesteld voor de reductie door een Mn-diaminekatalysator. Het mechanisme lijkt op dat van een Meerwein-Ponndorf-Verley-reactie waarbij het metaal- en N-H-groep van de katalysator het substraat en het oplosmiddel coördineren. Ons onderzoek werd bevestigd door MD-simulaties.

Ons werk laat de mogelijkheden van het modelleren op meerdere schalen in de katalyse zien. Terwijl conventionele modelleringsbenaderingen grotendeels gebaseerd zijn op DFT-berekeningen, kunnen aanvullende berekeningen waardevolle inzichten opleveren. Vooral numerieke methoden zoals microkinetische modellen zijn kosten- en tijdbesparend en maken een directe vergelijking tussen theoretische resultaten en gegevens van het experiment mogelijk. Daarom moeten conclusies over snelheidsbepalende stappen of enantioselectiviteit worden ondersteund door MKM. Hoewel computationele methoden niet perfect zijn, worden ze voortdurend verbeterd. Het tempo waarin computers evolueren, stelt ons in staat om meer gedetailleerd onderzoek te doen en modellen te onderzoeken die realistischer zijn. We moeten de ontwikkeling omarmen en de inzichten die we in het verleden hebben opgedaan kritisch evalueren. Dit proefschrift heeft aangetoond dat het niveau waarop een theoretisch onderzoek wordt uitgevoerd, bepalend kan zijn voor de conclusies die we trekken. Meer geavanceerde modellen bieden meer gedetailleerde en veelzijdige inzichten. Data-gebaseerde benaderingen bieden ook mogelijkheden om katalytische systemen vanuit een generalistisch oogpunt te analyseren. Het theoretisch onderzoek van grotere aantallen katalytische tussenproducten biedt mogelijkheden om activiteitsdescriptoren te vinden en rationeel ontwerp van katalytische systemen aan te sturen.

Acknowledgements

I want to thank my supervisor Evgeny who has provided support, guidance, encouragement and taught me everything about quantum chemistry. Thank you for sharing your knowledge and experience, telling me about Russian history, supporting me to present at as many conferences as possible, and, of course, for giving me the opportunity to come to Delft and join your group. Chong, thank you for teaching me DFT and helping me so much in my first year. I really appreciate that you cycled to university early to help me with my supercomputer struggles. I want to thank Dapeng for always troubleshooting my python scripts and having an open door whenever I had a coding question. Vivek, I want to thank you for helping me to get my first MD simulation running and giving me one of the best pieces of advice during my PhD: ”Never lose a working script.” Guanna, thank you for always being available when I had a question, for all the fun memories from our conferences and for inviting me to hotpot dinner. To Georgy, thank you for preparing me for my first presentation at a conference. I would like to thank Pavel for his collaboration and showing me the highlights of St. Petersburg. I want to thank Robbert for providing experimental evidence to my calculations and all the coffee chats. To my students, Koen, Felix, Arne-Jan, Rowin and Margareth, thank you for all your hard work. Karin, thank you for taking care of all bureaucratic matters.

I thank the people who warmly welcomed me (and convinced me to start my PhD) in Delft, Ági and Robert. Ina, thank you for motivating me to go to spinning classes on Saturday mornings. I want to thank Jaco for his great leadership as captain of the running team. Christophe, thank you for your help in translating my summary and all the coffee walks. I thank all the members of the ISE group, Divya, Jittima, Wenjun, Chuncheng, Ali, Evgeny Jr. and Adarsh, for the fun outings, inspiring group meetings and dinners. I want to thank the members of the CE group for including me and the ISE group in the Friday afternoon drinks.

Liliana, thank you for being the best ally a PhD student could wish for, inviting me for the the most beautiful views of The Hague skyline during countless dinners and giving the most insightful advice on scientifc and personal matters. I want to thank Elena for always listening to my (work) struggles, being the best roommate during conferences and accompanying me to every theater/orchestra/ballet show we could find in the Randstad. I thank my parents and brother for their encouragement, unconditional love and reassurance during my PhD. Finally, I would like to thank Jelmer for his emotional support, telling me to turn off the computer when I was submitting DFT calculations late at night and visiting me at university when his evening shifts were scheduled.

Curriculum Vitæ

Annika Meike Krieger was born on the 17th of April 1994 in Düsseldorf, Germany, where she grew up with her parents and brother. In 2012 she moved to the Netherlands to start her Bachelor degree in Chemistry. She graduated from the Radboud University Nijmegen in 2016 and continued with her Master degree with a specialization in Physical Chemistry. After receiving her diploma in 2018, she continued with her Ph.D. research in the Inorganic Systems Engineering group at the Delft University of Technology, under the supervision of prof. dr. Evgeny Pidko. The results of her research are described in this book.

List of Publications

Publications within the scope of this thesis

A.M. Krieger, V. Sinha, G. Li and E.A. Pidko, *Solvent-Assisted Ketone Reduction by a Homogeneous Mn-Catalyst*, submitted.

A.M. Krieger and E.A. Pidko, *The Impact of Computational Uncertainties on the Enantioselectivity Predictions: A Microkinetic Modeling of Ketone Transfer Hydrogenation with a Noyori-type Mn-diamine Catalyst*, ChemCatChem **13**(15), 3517–3524 (2021).

A.M. Krieger, V. Sinha, A.V. Kalikadien and E.A. Pidko, *Metal-ligand cooperative activation of HX (X=H, Br, OR)bond on Mn based pincer complexes*, Z. Anorg. Allg. Chem. **647**, 1486-1494 (2021).

A.M. Krieger, P. Kuliaev, F.Q. Armstrong Hall, D. Sun and E.A. Pidko, *Composition-and Condition-Dependent Kinetics of Homogeneous Ester Hydrogenation by a Mn-Based Catalyst*, J. Phys. Chem. C **124**, 26990-26998 (2020).

Publications outside the scope of this thesis

W. Yang, T.Y. Kalavalapalli, **A.M. Krieger**, T.A. Khvorost, I. Y. Chernyshov, M. Weber, E.A. Uslamin, E.A. Pidko and G.A. Filonenko, *Intrinsic Dynamics and Condition Dependence of Homogeneous Ester Hydrogenation Revealed by Mn-CNC Pincers*, ChemRxiv **1** (2021).

R. Van Putten, G.A. Filonenko, **A.M. Krieger**, M. Lutz and E.A. Pidko, *Manganese-Mediated C-C Bond Formation: Alkoxycarbonylation of Organoboranes*, Organometallics **40**, 674-681 (2021).

M.M.H. Smets, E. Kalkman, **A. Krieger**, P. Tinnemans, H. Meekes, E. Vlieg, H.M. Cuppen, *On the mechanism of solid-state phase transitions in molecular crystals-the role of cooperative motion in (quasi) racemic linear amino acids*, IUCrJ **7**, 331-341 (2020).

H.M. Cuppen, M.M.H. Smets, **A.M. Krieger**, J.A. van den Ende, H. Meekes, E.R.H. van Eck and C.H. Görbitz *The Rich Solid-State Phase Behavior of l-Phenylalanine: Disappearing Polymorphs and High Temperature Forms*, Cryst. Growth Des **19**, 1709-1719 (2019).

M.M.H. Smets, E. Kalkman, P. Tinnemans, **A.M. Krieger**, H. Meekes and H.M. Cuppen, *Polymorphism of the quasiracemate D-2-aminobutyric acid:L-norvaline*, CystEngComm **19**, 5604-5610 (2017).